

# Nanoscale

Accepted Manuscript

This article can be cited before page numbers have been issued, to do this please use: C. Gu, D. Li, S. Zeng, T. Jiang, X. Shen and H. Zhang, *Nanoscale*, 2021, DOI: 10.1039/D0NR07779H.



This is an Accepted Manuscript, which has been through the Royal Society of Chemistry peer review process and has been accepted for publication.

Accepted Manuscripts are published online shortly after acceptance, before technical editing, formatting and proof reading. Using this free service, authors can make their results available to the community, in citable form, before we publish the edited article. We will replace this Accepted Manuscript with the edited and formatted Advance Article as soon as it is available.

You can find more information about Accepted Manuscripts in the [Information for Authors](#).

Please note that technical editing may introduce minor changes to the text and/or graphics, which may alter content. The journal's standard [Terms & Conditions](#) and the [Ethical guidelines](#) still apply. In no event shall the Royal Society of Chemistry be held responsible for any errors or omissions in this Accepted Manuscript or any consequences arising from the use of any information it contains.

## ARTICLE

# Synthesis, Defect Engineering of Molybdenum Oxides and Their SERS Applications

Chenjie Gu, <sup>\*a#</sup> Delong Li, <sup>b#</sup> Shuwen Zeng, <sup>\*c</sup> Tao Jiang, <sup>a</sup> Xiang Shen, <sup>a</sup> and Han Zhang <sup>\*b</sup>Received 00th January 20xx,  
Accepted 00th January 20xx

DOI: 10.1039/x0xx00000x

Surface-enhanced Raman scattering (SERS) spectroscopy has been developed into a cross-disciplinary analytical technology through exploring various materials' Raman vibrational modes with ultra-high sensitivity and specificity. Although the conventional noble-metal based SERS substrates have achieved great success, the oxide-semiconductor-based SERS substrates are attracting researchers' intensive interests for their merits on facile fabrication, high uniformity and tunable SERS characteristics. Among all the SERS active oxide semiconductors, the molybdenum oxides (MoO<sub>x</sub>) possess exceptional advantages of high Raman enhancement factor, environment stability and recyclable detection etc. More interestingly, the SERS effect of the MoO<sub>x</sub> SERS substrates may involve both electromagnetic enhancement mechanism and the chemical enhancement mechanism, which is determined by the stoichiometry and morphology of the material. Therefore, the focus of this review will be on two critical points: 1) synthesis and material engineering methods of the functional MoO<sub>x</sub> material; 2) MoO<sub>x</sub> SERS mechanism and performance evaluation. First, we review recent works on the MoO<sub>x</sub> preparing and material property tuning approaches. Second, the SERS mechanism and performance of the various MoO<sub>x</sub> substrates are surveyed. Especially, the performance uniformity, enhancement factor and recyclability is evaluated. In the end, we discuss several challenges and open questions related to further promoting the MoO<sub>x</sub> as SERS substrate for monitoring extremely low trace molecules and the theory for better understanding of SERS enhancement mechanism.

## Introduction

The enhanced Raman scattering phenomenon was first reported by M. Fleischmann on a roughened silver electrode coated with pyridine in 1974.<sup>1</sup> Hereafter, research works conducted by Jeanmaire and Van Duyne, Albrecht and Creighton further lay solid foundations on this Raman enhancement phenomenon, which was named as surface-enhanced Raman scattering (SERS).<sup>2, 3</sup> Today, SERS technique has become a cross-disciplinary analytical tool endorsed by the merits of non-destructivity, ultra-high sensitivity and specificity, and the great achievements of the SERS technique are expediting its application in the fields of chemical engineer, biological sensing, food safety and environmental protection, etc.<sup>4-17</sup>

Conventionally, SERS detection relies on the surface electromagnetic field or "hot spots", which are produced by the surface plasmon polaritons that excited by the incident Raman laser on the noble metal surface (Au, Ag and Cu etc.) with the different nanostructures, and normally up to 7~8 orders of molecules' Raman scattering signal enhancement could be obtained.<sup>18-23</sup> Experimentally, for the purpose of strengthening the surface electromagnetic field induced by the surface plasmon polaritons and consequently promoting the electromagnetic enhancement mechanism (EM), researchers have paid great efforts on designing and preparing novel noble metal nanostructures or compounds, and substantial improvement on the SERS performance has been achieved.<sup>24-27</sup> However, meticulous control of the nanostructures to produce strong surface plasmon polaritons isn't an easy task. Besides, in a continuous expanding of challenging applications, noble metals usually show poor stability, biocompatibility and large-scale uniformity, which further impedes the practical application a lot.<sup>28-30</sup>

In the meanwhile, oxide semiconductors have been extensively studied for their superior light-material interaction capabilities, and numerous application cases by manipulating the light-material interaction modes or strength have been demonstrated in the early literature,<sup>31-34</sup> however, SERS phenomenon on the oxide semiconductors, as one of the important light-material interaction cases, initially receives much less attention in comparison to that on noble metals due

<sup>a</sup> Institute of Photonics, Ningbo University, 818 Feng Hua Road 315211, Ningbo, China.

<sup>b</sup> Collaborative Innovation Center for Optoelectronic Science & Technology, International Collaborative Laboratory of 2D Materials for Optoelectronics Science and Technology of Ministry of Education, Institute of Microscale Optoelectronics, Shenzhen University, Shenzhen 518060, China.

<sup>c</sup> XLIM Research Institute, UMR 7252, CNRS/University of Limoges, Avenue Albert Thomas, 87060 Limoges, France.

# C. Gu and D. Li contributed equally to this work.

Electronic Supplementary Information (ESI) available: [details of any supplementary information available should be included here]. See DOI: 10.1039/x0xx00000x

to the weak Raman signal enhancement capability.<sup>35</sup> Until recently, the out breaking of synthesizing methods for preparing the oxide semiconductors with various chemical stoichiometries and morphologies promotes the intensive research of the oxide semiconductors for SERS application.<sup>36, 37</sup> Experimental results manifest that materials like titanium oxides ( $\text{TiO}_{2-x}$ ), cuprous oxides ( $\text{Cu}_2\text{O}$ ), zinc oxides ( $\text{ZnO}_x$ ), reduced graphene oxides (rGO), tungsten oxides ( $\text{WO}_{3-x}$ ) and molybdenum oxides ( $\text{MoO}_x$ ), etc. show promising SERS characteristics. In the meanwhile, SERS mechanism investigation on these materials also reveals that either the electromagnetic enhancement/chemical enhancement or both of them exist, which brings extra advantages for the oxide semiconductors as SERS substrates.<sup>38-47</sup> Impressively, among all these oxide semiconductors,  $\text{MoO}_x$  show exceptional SERS characteristics, which is ascribed to the diverse defect engineering approaches and widely tunable free electron concentrations, therefore plentiful research works have been reported in the recent years.<sup>36, 48</sup>

Molybdenum oxides are a kind of versatile transition metal oxides with various applications in the fields of chemical catalyst, bio-sensing, energy storage, fluorescence detection, electrochromic glass and hole transport layer, etc. For example, Cheng et al. reported the use of  $\text{Pd}/\text{MoO}_{3-x}$  hybrids as chemical catalyst for ammonia borane hydrolysis. Xiao et al. implemented the  $\text{MoO}_x$  quantum dots to probe the 2, 4, 6-Trinitrotoluene, while Balendhran et al. fabricated a field effect transistor by using the  $\text{MoO}_3$  as the channel material for bovine serum albumin (BSA) detection. And Achadu et al. used the antibody modified magnetic-derivatized plasmonic molybdenum trioxide quantum dots as plasmonic/magnetic agent, and the antibody modified fluorescent graphitic carbon nitride quantum dots as the monitoring prober for virus detection.<sup>49-55</sup> Experimentally,  $\text{MoO}_x$  have several different crystal structures, and the relatively stable one is the orthorhombic structure ( $\alpha\text{-MoO}_3$ ), whereas the monoclinic structure ( $\beta\text{-MoO}_3$ ),  $\text{MoO}_3\text{-II}$  ( $\varepsilon\text{-MoO}_3$ ) and hexagonal structure ( $\text{h-MoO}_3$ ) are metastable phases. Moreover,  $\text{MoO}_x$  also show rich variants on morphologies and chemical stoichiometries. Therefore, in order to achieve  $\text{MoO}_x$  with diverse functions, tremendous efforts have been made to explore advanced material preparing and engineering strategies. Generally, methods of chemical liquid synthesis and vapour deposition are extensively reported, e.g., sputtering, evaporation, chemical vapour deposition or physical vapour deposition etc.

To date, a great number of studies on  $\text{MoO}_x$  for the SERS applications have been reported since the first use of  $\text{MoO}_x$  ribbons as SERS substrates in 2010.<sup>56</sup> Especially in the recent three years, various functional  $\text{MoO}_x$  materials have been prepared and remarkable SERS performance improvement has been achieved (Figure 1), however a thorough review on  $\text{MoO}_x$  material preparing, defect engineering methods as well as SERS mechanism discussions and performance evaluations are still lacking. Herein, in this minireview, we will emphasize on the SERS application of the  $\text{MoO}_x$ . First, we briefly introduce the fundamental material properties, e.g., crystalline structures and band structure of  $\text{MoO}_x$ . Then, we mainly focus

on the diverse preparing methods and material engineering strategies on the physical and chemical properties of  $\text{MoO}_x$ . Next, we discuss the SERS mechanism as well as the SERS performance of  $\text{MoO}_x$  and  $\text{MoO}_x$  hybrids. Finally, we summarize the paper, several challenges and open questions of  $\text{MoO}_x$  as the promising SERS substrates for monitoring extremely low trace molecules as well as the theory for better understanding the SERS enhancement mechanism are presented.

## Fundamental Material Properties and Synthesis Methods

### Crystal Structures

Molybdenum oxides have several crystal structures, namely  $\alpha\text{-MoO}_3$ ,  $\beta\text{-MoO}_3$ ,  $\varepsilon\text{-MoO}_3$  and  $\text{h-MoO}_3$ . Experimental evidences indicate that  $\alpha\text{-MoO}_3$  is thermally stable, whereas  $\beta\text{-MoO}_3$ ,  $\varepsilon\text{-MoO}_3$  and  $\text{h-MoO}_3$  are metastable phases, and phase transformation from the metastable phase of  $\beta\text{-MoO}_3$  and  $\text{h-MoO}_3$  to  $\alpha\text{-MoO}_3$  is ready to happen under the high temperature condition.

The  $\alpha\text{-MoO}_3$  has an orthorhombic structure with the cell parameter of  $a=3.962 \text{ \AA}$ ,  $b=13.85 \text{ \AA}$  and  $c=3.697 \text{ \AA}$  (Figure 1a), respectively.<sup>57, 58</sup>  $\alpha\text{-MoO}_3$  possesses the typical layered crystal structure, which is constructed by the linked and distorted  $\text{MoO}_6$  octahedra sharing four corners to form double layers. More specifically, the  $\text{MoO}_6$  octahedra forms edge-sharing along the [001] crystal direction and corner sharing rows along the [100] crystal direction in the double-layer sheet, and the double-layer sheet stacks are maintained by the weak van der Waals (vdW) forces along the [010] crystal direction. The thickness of the double layers constructed by the distorted  $\text{MoO}_6$  octahedra is about  $14 \text{ \AA}$ , whereas the vdW gaps between the neighbouring layer is  $6.9 \text{ \AA}$ .<sup>59</sup> The above layered crystal structure provides the possibility of creating two dimensional (2D)  $\alpha\text{-MoO}_3$  sheets.<sup>60</sup> Moreover, it can be observed in the octahedron that the oxygen atoms can be categorized into three types based on its coordination number (inset of Figure 2a), which is terminal oxygen ( $\text{O}_t$ ), asymmetric oxygen ( $\text{O}_a$ ), and symmetrically bridging oxygen ( $\text{O}_s$ ). The  $\text{O}_t$  bonds to single Mo and the bond length is  $1.67 \text{ \AA}$ . While the  $\text{O}_a$  laterally bonds to two Mo atoms and the bond lengths are  $1.74 \text{ \AA}$  and  $2.25 \text{ \AA}$ , respectively. The  $\text{O}_s$  bonds to three Mo atoms, the length of two horizontal bonds is  $1.95 \text{ \AA}$ , and the vertical one is  $2.33 \text{ \AA}$ . Charge distribution analysis of the Mo-O bonds in the  $\text{MoO}_6$  octahedron reveals strong covalent characteristic on the shortest Mo-O bond, whereas ionic bond dominates the longest Mo-O bond.<sup>61, 62</sup>

The  $\beta\text{-MoO}_3$  has a monoclinic structure, the cell parameter of the  $\beta\text{-MoO}_3$  crystal phase is  $a=5.6109 \text{ \AA}$ ,  $b=4.8562 \text{ \AA}$  and  $c=5.6285 \text{ \AA}$ , while the monoclinic angle is  $120.95^\circ$  (Figure 2b). The structure of  $\beta\text{-MoO}_3$  is a kind of monoclinically distorted variants of  $\text{ReO}_3$ , in which the  $\text{MoO}_6$  octahedra shares the corner and forms the distorted strings in the [001] crystal direction.<sup>63</sup> In the meanwhile, the Mo atom corners within the strings are pairwise drawn nearer to each other to form

doublets, resulting in the distortion of the  $\text{MoO}_6$  octahedra and elimination of the crystal plane. Moreover, in the string of the  $\text{MoO}_6$  octahedra, the distorted angle is  $13.18^\circ$ , and the Mo atom lies within the octahedra, bonding to six inequivalent O atoms with the bond length of 1.694, 2.054, 1.766, 2.288, 1.800 and 2.056 Å, respectively. Finally, as a metastable phase, it is reported that  $\beta\text{-MoO}_3$  will transform into the  $\alpha$ -phase by heating above 673 K.<sup>64</sup>

The  $\epsilon\text{-MoO}_3$  and  $h\text{-MoO}_3$  crystal structures are less studied than the above two. The  $\epsilon\text{-MoO}_3$  is a high-pressure modification crystal structure, and it is with a specific monoclinic phase (Figure 2c).<sup>65</sup> While the  $h\text{-MoO}_3$  has a hexagonal structure with the cell parameters are determined to be  $a=b=10.57$  Å,  $c=3.725$  Å (Figure 2d).<sup>66</sup> The structure of  $h\text{-MoO}_3$  is constructed with the  $\text{MoO}_6$  octahedra by chaining them in zigzag. Moreover, the unique feature of the  $h\text{-MoO}_3$  is that the octahedra chains build a hexagonal crystalline structure, and create large one-dimensional tunnels along the [001] crystal direction with a diameter of  $\sim 3.0$  Å.<sup>67</sup>

### Controllable Synthesizing of $\text{MoO}_x$

Material synthesis establishes the foundation of  $\text{MoO}_x$  as an attractive material for SERS application. Up to now, a variety of synthetic approaches have been reported, which can be categorized into two primary strategies, e.g., the vapor-phase deposition and liquid-phase synthesis. Therefore, in this part, synthetic methods of  $\text{MoO}_x$  with different approaches are comprehensively discussed.

**Vapor-phase Deposition** Since 1950s, the vapour-phase deposition has been extensively investigated for the synthesis of bulk crystals.<sup>68, 69</sup> In general, the vapour-phase deposition methods are based on the deposition of vaporized target material onto specific substrates, which mainly includes physical vapour deposition (PVD), chemical vapour deposition (CVD), chemical vapour transport (CVT) and so on. Generally, through the vapour-phase deposition method, it is able to prepare  $\text{MoO}_x$  materials with controlled quality and structure, as well as large-scale production.<sup>70, 71</sup>

For PVD method, metallic Mo or its oxide are commonly chosen as the starting material and transited from solid phase into vapour phase by evaporation or sputtering.<sup>71</sup> A range of techniques have been reported to synthesize  $\text{MoO}_x$ , such as sputtering, thermal and electron-beam evaporation, pulsed laser deposition, etc. These PVD techniques are suitable for the control growth of thin  $\text{MoO}_x$  films as revealed by the TEM, AFM, SEM, XRD, XPS and Raman spectroscopy detections. However, it also shows that each technique has its own characteristics and processing parameters, depending on the selection of PVD techniques.

Sputtering is a widely adopted PVD technique with controllable growth rate and thickness for thin film deposition. In a typical sputtering process, the incident inert gas is firstly ionized to generate energetic plasma by applying a high voltage, the ions then bombard target source to generate sputtered flux, which will finally deposit onto the substrate to

form the film product.<sup>69</sup> In order to prepare the  $\text{MoO}_x$  by sputtering method, Mo target was usually used to deposit Mo thin film at first. Then, the  $\text{MoO}_x$  was synthesised by dry oxidation of the sputtered Mo thin film. The influence of Mo thickness variation, oxidation temperature and time on the crystallographic structure, surface morphology and roughness of  $\text{MoO}_x$  thin films can be studied by using TEM, AFM, XRD, SEM and Raman spectroscopy. For example, Dwivedi et al. reported a radio-frequency (RF) sputtering method to deposit 150 and 240 nm thick Mo films at 100 W RF power in pure argon atmosphere, the deposited Mo films were then subjected to oxidize at 400 °C and 500 °C in the  $\text{O}_2$  ambient to obtain crystal  $\text{MoO}_3$  films.<sup>72</sup> Chang et al. studied the phases and textures of resultant  $\text{MoO}_3$  under different conditions. A 3 inch diameter metallic Mo target was employed as precursor during the sputtering process. It was found that the final structure of  $\text{MoO}_3$  was directly related to the sputtering gas composition as well as the annealing temperature. As shown in Figure 3a, the phase variety and texture can be analysed by XRD measurement. When sputtered in mixed  $\text{Ar}/\text{O}_2$  atmosphere, the obtained  $\text{MoO}_3$  film form  $\alpha$  and/or  $\beta$  phase, varying with the annealing temperature. The films annealed below 350 °C show the pure  $\beta$  phase, films at 350-400 °C are composed of both  $\alpha$  and  $\beta$  phases, and the pure  $\alpha$  phase are obtained when the temperature beyond 450 °C.<sup>73</sup>

Evaporation method (thermal and electron beam) is also a commonly used PVD technique for molybdenum oxides synthesis. The target source, usually  $\text{MoO}_3$  powder, is melt and evaporated by heating or bombardment of high-energy electron beams, then the vaporized source material deposits onto the substrate to form  $\text{MoO}_3$  with controlled microstructure.<sup>74, 75</sup> This technique can provide a relatively high deposition rate as well as the controllability of deposition parameters, which enables the direct growth of thin molybdenum oxides films on various technical substrates, like  $\text{Si}/\text{SiO}_2$ , FTO, ITO and glass substrates.<sup>76, 77</sup> Generally, the morphologies and crystal phases of molybdenum oxides films are closely related to the sublimation and deposition temperatures. For example, Wang et al. reported the mica supported atomically thin  $\alpha\text{-MoO}_3$  crystal film by vaporized  $\text{MoO}_3$  powder in  $\text{N}_2$  gas, and revealed the relationship between the growth temperature and structure of as-grown  $\text{MoO}_3$  nanosheets.<sup>78</sup> As shown in Figure 3b and c, the thickness of the  $\text{MoO}_3$  sheet is reduced and lateral size is enlarged as the growth temperature rises. The high saturation vapor pressure and small nucleation rate of the  $\alpha\text{-MoO}_3$  at high temperature would result in large and ultrathin  $\alpha\text{-MoO}_3$  sheets growth. In a typical physical vapour deposition process, the morphology of the as prepared  $\text{MoO}_3$  is strongly depend on the substrate and source temperature, as shown in Figure 3d. According to the optical images, the thickness of the  $\text{MoO}_3$  nanosheets is reduced and lateral size of the  $\text{MoO}_3$  is enlarged when the substrate temperature increases.

Pulsed laser deposition is another efficient PVD technique, especially for electrically insulating compound targets. Different from the aforementioned sputtering or evaporation

method, the vaporization energy comes from the pulsed laser, which is well suited for the semiconducting  $\text{MoO}_x$  source.<sup>79</sup> Camacho-López et al. deposited  $\text{MoO}_x$  thin films ( $x$  is between 1.8 and 2.1) and observed the structural transformation from amorphous  $\text{MoO}_x$  to a mixed  $\alpha$  and  $\beta$  phases of  $\text{MoO}_3$ .<sup>80</sup> Except for the technical parameters (including deposition temperature, substrate and oxygen gas flow rate), the laser wavelength, power density and pulse duration also have great effects on the growth process.<sup>81</sup> In the typical experiment, the ultraviolet lasers are most commonly used for the deposition of  $\text{MoO}_3$  films, such as argon fluoride (193 nm), krypton fluoride (248 nm), xenon fluoride (351 nm) excimer lasers.<sup>80, 82-84</sup>

CVD method is an advantage vapour-phase based direct growth process for  $\text{MoO}_x$  synthesis, which is analogous to the above mentioned PVD method. The difference is that the carbonyl materials, such as molybdenum hexacarbonyl ( $\text{Mo}(\text{CO})_6$ ), is used as precursor during the CVD process.<sup>85, 86</sup> Benefiting from the volatile property of precursor, CVD requires much lower growth temperature and less energy consumption for  $\text{MoO}_3$  deposition when compared to PVD.<sup>87, 88</sup>  $\text{MoO}_2$  and sub-stoichiometric molybdenum oxides ( $\text{MoO}_{3-x}$ ) can be grown via controlled CVD process by utilizing  $\text{MoO}_3$  powder as precursor.<sup>89-91</sup> In the literature, Wu et al. synthesized ultrathin  $\text{MoO}_2$  nanosheets on an inverted  $\text{SiO}_2/\text{Si}$  substrate by reducing  $\text{MoO}_3$  powder. As shown in Figure 4a-c, the as-grown  $\text{MoO}_2$  nanosheets shows the micron-scale lateral size and thickness of  $\sim 9$  nm, as well as the high crystallinity. Wang et al. synthesized the molybdenum oxides nanomaterials by a plasma-enhanced hot filament CVD with  $\text{N}_2$  and  $\text{MoO}_3$  precursors.<sup>86</sup> In this process, the carrier gas  $\text{N}_2$  were discharged to generate plasma, which could lead to the effective reduction of  $\text{MoO}_3$ . And the experimental results in Figure 4d-e show that the structure of  $\text{MoO}_{3-x}$  product with different can be either nanoparticles or nanosheets, depending on the  $\text{N}_2$  flow rate and growth time.

CVT is a traditional vapour-solid growth method for single crystal deposition. The CVT growth is usually conducted in a two-zone furnace under the continuous flow of carrier gas, which involves the evaporation of volatile precursors (e.g.:  $\text{MoO}_3(\text{OH})_2$ ,  $\text{MoO}_3$ ) in high-temperature zone and the deposition of products in low-temperature zone.<sup>92</sup> Lee et al. modified the CVT process and achieved the deposition of  $\text{MoO}_2$  thin films.<sup>93</sup> In their experiment, the  $\text{SiO}_2$  substrate was placed under the  $\text{MoO}_3$  precursor, and the dual temperature zone was not required for the film deposition. By inducing  $\text{H}_2$  as the transport agent,  $\text{MoO}_3$  was reduced and thus form the volatile species,  $\text{MoO}_3(\text{OH})_2$ , which can be transported in vapour phase and deposited onto the substrate to form a homogeneous thin  $\text{MoO}_2$  film. However, the reduction of  $\text{MoO}_3$  involved a series of complex reactions and intermediates, for example,  $\text{Mo}_4\text{O}_{11}$  is a frequently observed intermediate for the reduction of  $\text{MoO}_3$ .<sup>94, 95</sup> On the other hand, De Melo et al. reported a chemically driven isothermal closed space CVT process for pure  $\text{MoO}_2$  synthesis.<sup>96</sup> Different from other methods, this CVT process can produce pure  $\text{MoO}_2$

films without any other stoichiometric  $\text{MoO}_x$  like  $\text{MoO}_3/\text{Mo}_4\text{O}_{11}$ .

DOI: 10.1039/D0NR07779H

**Liquid-phase Synthesis** For liquid-phase synthesis of nanostructured  $\text{MoO}_x$  materials, the synthetic methods mainly include hydrothermal/solvothermal approach, chemical precipitation, sol-gel method, and electrochemical method. In these methods, the precursor source materials are commonly the ionic salt, acid or polymer containing Mo. These liquid-phase syntheses methods show outstanding advantages in the construction of diverse morphologies and structures for  $\text{MoO}_x$  nanomaterials, as well as the lower cost and higher yield than vapor-phase deposition.

The hydrothermal/solvothermal method is one of the most extensively employed approaches for nanomaterials synthesis. Hydrothermal or solvothermal synthesis of  $\text{MoO}_x$  materials relies on the controlled crystallization of molybdenum oxide seeds from the precursor in the solution environment with high temperature and pressure.<sup>97</sup> This synthetic method enables the good control and chemical homogeneity of the crystal structure, morphology and size by manipulating the reaction parameters. The reactant source, reaction time and temperature, concentration and species of solvent and additive/surfactant, are all key parameters for the nucleation and growth of molybdenum oxides. By properly controlling the synthetic procedures, multidimensional architectures of  $\text{MoO}_x$  nanomaterials can be designed and synthesized. A variety of micro-/nanostructures including 0D quantum dots, 1D nanorods, nanowires, nanotubes, 2D nanosheets, and 3D porous structures have been synthesized by precise controlling the synthesis process.<sup>98-104</sup> Figure 4f-h show the typical TEM and SEM morphologies of molybdenum oxides nanomaterials synthesised by using hydrothermal or solvothermal method.<sup>105, 106</sup> Moreover, the hydrothermal synthesis allows the phase transition between metastable and stable crystal structures of molybdenum oxides. The nucleation process of different phases is found to be dependent on the concentration of acid/saline ions and temperature during the hydrothermal treatment.<sup>107</sup> The  $\beta$ - $\text{MoO}_3$  tends to form under the acidic aqueous environment with a high concentration of  $\text{H}^+$ ,  $\text{Na}^+$  or  $\text{K}^+$  ions, while  $\alpha$ - $\text{MoO}_3$  is more likely to be formed under a high hydrothermal temperature.<sup>108</sup> The hydrothermal synthesis is also an effective method to introduce oxygen vacancies or Mo ion valance tuning in the as prepared  $\text{MoO}_x$  samples, which will be discussed in the next section.

Chemical precipitation is a facile liquid-phase synthetic method without high temperature or high pressure. Sakaushi et al. utilized sodium molybdenum oxide dihydrate ( $\text{Na}_2\text{MoO}_4 \cdot 2\text{H}_2\text{O}$ ) as the precursor to synthesize nanostructured  $\alpha$ - $\text{MoO}_3$ , which can assemble to form a large-area freestanding film.<sup>109</sup> The whole process was conducted in a low-temperature (75 °C) aqueous solution with the pH of 0.5. The presence of organic acid also exhibits strong influence on the nanostructures of  $\alpha$ - $\text{MoO}_3$ . In addition, Kumar et al. synthesized  $\alpha$ - $\text{MoO}_3$  with the aid of three organic acids, citric acid (CA), tartaric acid (TA) and ethylene diamine tetra-acetic

acid (EDTA).<sup>110</sup> The structural difference of organic ligands led to distinct morphologies of the resultant  $\alpha$ -MoO<sub>3</sub> products, in which hexagonal plates were prepared in CA or TA solution, while nanorods and nanoplates were prepared in EDTA solution. While in Jittiarporn et al. experiment, they carried on an intensive study about the impact of precipitation temperature on the nanostructure and physiochemical properties of MoO<sub>3</sub>.<sup>111</sup> It shows that as the temperature varied from 55 to 85 °C, the crystallite size enlarged, band gap became narrower, and defects in the crystal lattice increased. At 85 °C, the h-MoO<sub>3</sub> crystals aggregated together and formed a flower-like cluster, which possessed the reduced band gap, increased oxygen vacancies, and best photochromic property.

Sol-gel process is a versatile wet chemical approach for molybdenum oxides synthesis, which enables the good control of textural and morphological characteristics of materials.<sup>112</sup> The sol-gel method mainly undergoes several consecutive steps including: the initial hydrolysis of molecular precursors, the following condensation and gelation, and the final drying process to obtain molybdenum oxides crystals. Tang et al. utilized the hydrogen peroxide treated Mo powder as precursor to synthesize the  $\alpha$ -MoO<sub>3</sub> nanomaterials.<sup>113</sup> The obtained MoO<sub>3</sub> was composed of 2D nanoplates with the average size of about 1  $\mu$ m and thickness of 100 nm. Morphologies of the  $\alpha$ -MoO<sub>3</sub> products can be well controlled by adjusting the molar ratios of precursors, drying conditions or the additive/surfactant. Additionally, Cong et al. studied the influence of the relative molar ratios of molybdate and citric acid in the precursor on the growth process of  $\alpha$ -MoO<sub>3</sub> samples.<sup>114</sup> The citric acid molar ratio to molybdate in the precursors was demonstrated to have a significant impact on the competing crystal growth process of  $\alpha$ -MoO<sub>3</sub> nanorods. Additive or surfactant can also be induced as templates into the sol-gel process to assist the shaping of morphology and structure. For example, Brezesinski et al. used poly(ethylene-co-butylene)-b-poly(ethylene oxide) block copolymer as soft-template to synthesized a mesostructured  $\alpha$ -MoO<sub>3</sub> thin film.<sup>115</sup> As a result, a homogeneous and porous cubic architecture MoO<sub>3</sub> film without obvious structural defects was successfully synthesized by this simple method. More recently, Yin et al. successfully synthesized well crystallized, high surface area plasmonic MoO<sub>3-x</sub> by combing the evaporation induced self-assembly process and a subsequent hydrogen reduction with the assist of F127 (PEO<sub>106</sub>PPO<sub>70</sub>PEO<sub>106</sub>) as organic template.<sup>116</sup> During the synthesis procedure, commercial Mo metal powder was chosen as Mo precursor. Detailed characterization of XRD, TEM, XPS and Nitrogen adsorption-desorption analysis measurement proved that the MoO<sub>3-x</sub> possessed a high surface area and strong localized surface plasmon resonance under incident light.

Electrochemical methods including the electrodeposition and electrochemical anodization, are kinds of economic and facile techniques for molybdenum oxides synthesis. Moreover, it is easy to proceed the structural modulation and functional modification during the electrochemical process.<sup>117, 118</sup>

Electrodeposition is a well-suitable method for producing thin, large and uniform molybdenum oxides films. Generally, the molybdate solution, such as sodium molybdate (Na<sub>2</sub>MoO<sub>4</sub>), is selected as the electrolyte.<sup>119</sup> A further investigation demonstrated that hydrogen peroxide dissolved Mo powder can also be used for the electrodeposition of MoO<sub>3</sub> films.<sup>120</sup> More importantly, the crystallinity, phase and Mo oxidation state of the as-deposited molybdenum oxides film are reported to be very sensitive to the electrodeposition parameters. In addition, Yao et al. reported that the phase structure of the formation of  $\alpha$ -MoO<sub>3</sub> or  $\beta$ -MoO<sub>3</sub> strongly relied on the cyclic voltammetry experiments parameters. The  $\beta$ -MoO<sub>3</sub> was formed over the potential range from -1.2 to -0.40 V (vs Ag/AgCl), while  $\alpha$ -MoO<sub>3</sub> was formed by applying the bias of -1.2 to 0.40 V.<sup>57</sup> Moreover, the bath pH is also a significant factor, which determined the oxidation state of resultant MoO<sub>x</sub>.<sup>121-123</sup>

Electrochemical anodization is another electrosynthesis method to prepare molybdenum oxides materials. By electrochemical etching and oxidation of Mo metal simultaneously, MoO<sub>x</sub> with controlled microstructure can be obtained. Lou et al. synthesized  $\alpha$ -MoO<sub>3</sub> thin films by anodization of Mo foils in the ethylene glycol/water solution with sodium fluoride as electrolyte.<sup>124</sup> The anodization of metallic Mo involved two competing processes, the anodic oxidation and the chemical dissolution. The fluoride etching of  $\alpha$ -MoO<sub>3</sub> was favoured along [001] crystal direction and crystal growth was altered and forced along [010], leading to the promoted growth along (hk0) planes to form the platelet morphology. Szkoda et al. further studied the impact of fluoride ions on the morphology and porosity of synthesized films.<sup>125</sup> The presence of fluoride ions significantly affected the morphology of MoO<sub>3</sub>, resulting in a maze-like architecture and the anisotropic growth along [110] crystal direction.

## Material Engineering and Characterization

Stoichiometric MoO<sub>3</sub> in  $\alpha$ -crystal phase is an indirect and wide band gap semiconductor with the experimentally detected band gap of  $\sim$ 3.1 eV, the rest crystal phases of stoichiometric MoO<sub>3</sub> feature similar band gaps.<sup>60</sup> Recent years, density functional theory (DFT) calculation has been extensively used to investigate the MoO<sub>x</sub> material properties. By implementing the improved calculation schemes, e.g., modified Becke-Johnson potential (mBJ-GGA) method and the hybrid functional (HSE06) method, the band gap of the MoO<sub>3</sub> can be theoretically reproduced.<sup>59, 60</sup> For instance, as shown in Figure 5a, calculation of the  $\alpha$ -MoO<sub>3</sub> band diagram with the mBJ-GGA method along the high symmetric points of  $\Gamma$ -X-S-R-T-Z- $\Gamma$  in the Brillouin zone indicates that the valence band maximum (VBM) is at the R point, while the conduction band minimum (CBM) is located at the  $\Gamma$  point, which confirms that  $\alpha$ -crystal MoO<sub>3</sub> is an indirect band gap with the band gap of about 3 eV. Similar band diagram is also obtained by using the HSE06 method. In addition, density of states (DOS) analysis in Figure 5b-e shows that the energy band below VBM is mainly

contributed by the Mo-d and O1, 2, 3-p electrons hybridization, while the contribution from Mo-s/p and O1, 2, 3-s electron states is negligible (here O1 equal to O<sub>t</sub>, O2 equal to O<sub>a</sub> and O3 equal to O<sub>s</sub>). On the other hand, the energy band above the CBM is mainly contributed by the Mo-d and O1, 2, 3-p electrons hybridization, and the contribution from Mo-s/p and O1, 2, 3-s electrons is insignificant.<sup>126</sup> At this stage, it is worth noting that experimentally prepared MoO<sub>x</sub> usually are n-type semiconductor, which is due to the unintentional formation of intrinsic defect in the oxides (e.g., oxygen vacancy), however, in order to obtain the full optical and electrical functions of MoO<sub>x</sub>, material engineering strategies to tune the band structure, free electron concentration and morphologies etc. are essentially demanded. Presently, published literature indicates that oxygen vacancies or dopants affect the MoO<sub>x</sub> properties a lot.<sup>127</sup> Other than that, structural and compound modifications such as film thickness, chemical compositions, crystal phases and surface states control, also have great influence on MoO<sub>x</sub> properties.<sup>128</sup> Herein, in this section, the following strategies of tuning material properties are first reviewed: i) oxygen vacancies creation; ii) doping or intercalation with different types of elements; iii) crystal phases and morphologies manipulating; iv) MoO<sub>x</sub> hybrids formation.

### Oxygen Vacancy Creation

As aforementioned, the orthorhombic structure of α-MoO<sub>3</sub> is comprised by a bilayer network of MoO<sub>6</sub> octahedra that stacks along the [010] crystal direction, and the neighbouring bilayers bond with each other by vdW forces. Atomic structure in Figure 2a already shows that, O<sub>t</sub> bonds to Mo, pointing perpendicular to the vdW gap in the [010] crystal direction, and O<sub>a</sub> asymmetrically bonds to two nearby Mo ions in the [100] crystal direction, whereas O<sub>s</sub> bonds to two Mo ions with the short bond in the [001] crystal direction and another Mo ion with the longer bond in the [010] crystal direction (Figure 6a).<sup>61</sup> DFT calculation demonstrates that the formation energy of the oxygen vacancy on three different oxygen sites varies, and the lowest one is 1.32 eV, which corresponds to the oxygen vacancy formation at the O<sub>t</sub> site (Figure 6b). On the other hand, the formation energies of oxygen vacancies at O<sub>a</sub> and O<sub>s</sub> site is 2.49 eV and 3.41 eV, which are higher than that at O<sub>t</sub>, implying the oxygen vacancy formation at these two respective sites is less energy favourable.<sup>129</sup> In the practical situation, physical characterization confirms that oxygen vacancies tend to be created at O<sub>t</sub> site with higher probability, and they also can be created at O<sub>a</sub> and O<sub>s</sub> but with lower probability, which is determined by the defect engineering strategy.<sup>62</sup> Besides, accounting on the number of bonded O atoms are removed, a number of non-stoichiometric molybdenum-oxides with the average valence between +6 and +4 are prepared, e.g., MoO<sub>2</sub>, Mo<sub>4</sub>O<sub>11</sub>, Mo<sub>9</sub>O<sub>26</sub>, Mo<sub>18</sub>O<sub>52</sub> and Mo<sub>4</sub>O<sub>11</sub> etc. (Figure 6c).<sup>126</sup>

The introduce of oxygen vacancies in the MoO<sub>3</sub> crystal inevitably create rich defect levels in the band gap. More insightfully, the freely vibrating electrons (two per oxygen

vacancy) move close to the Mo atoms, and a portion of the wave function superimposes on the Mo-Mo (with d-d character) band, generating new energy levels lying within the band gap, while the rest is relocated to the initially empty energy levels at the edge of the conduction band (Figure 7a).<sup>130</sup> Meanwhile, DOS calculation reveals more information about the defect-level positions generated by removing the O<sub>t</sub>, O<sub>s</sub> and O<sub>a</sub>. It shows that the defect levels induced by the oxygen vacancies at O<sub>a</sub> sites locate at the lower part of the band gap, and those induced by oxygen vacancies at O<sub>t</sub> sites locate at the upper part of the band gap, whereas defect levels induced by oxygen vacancies at O<sub>a</sub> sites are much close to the conduction band edge (Figure 7b-d).<sup>53</sup> Besides, experimental evidence also shows that, for low degree of vacancy density, the free electrons from the oxygen vacancies only occupy the bonding d-d band, and the Fermi level of the material is hardly changed. However, at higher degree of vacancy density, more free electrons are generated, and they tend to occupy the empty d-d band in the conduction band, which consequently raises the electron filling level and shifts the Fermi level towards the conduction band.<sup>131</sup>

To achieve sub-molybdenum-oxides with different oxygen vacancy concentrations, effective strategies of introducing oxygen vacancies are principally important. Currently, methods of chemical reduction, semiconductor process technology and light irradiation, etc. are widely used. For example, sodium borohydride (NaBH<sub>4</sub>), a strong inorganic reductant, can be used to react with MoO<sub>3</sub> nanoparticles in a mixed solution to introduce the oxygen vacancies. In the experiment, stoichiometric MoO<sub>3</sub> nanoflakes were first prepared by oxidizing the MoS<sub>2</sub> in the H<sub>2</sub>O<sub>2</sub> solution, then NaBH<sub>4</sub> was added to create the oxygen vacancies through tuning the mole ratio between the NaBH<sub>4</sub> and Mo (NaBH<sub>4</sub>:Mo). It is shown in the Figure 8a that the colour of the MoO<sub>3</sub> suspension changes from light green, then blue to brown with the continuous increase of reductive NaBH<sub>4</sub>. The UV-vis absorption spectra in Figure 8b also reflect obvious peak shift, which can be ascribed to the change of free electron concentration provided by the oxygen vacancies. Furthermore, XPS detection confirms that partial of the Mo<sup>6+</sup> ions in MoO<sub>3</sub> are reduced at low mole ratio condition, however, when the mole ratio reaches 6:1, all the Mo<sup>6+</sup> ions are reduced to +4 valance state, and pure MoO<sub>2</sub> can be obtained (Figure 8c). At this time, it also should be mentioned that, due to the layered structure of the MoO<sub>3</sub>, EDX mapping on the reduced MoO<sub>x</sub> indicates that Na<sup>+</sup> ions from NaBH<sub>4</sub> intercalate into the material, which introduce extra defect levels in to the band gap.<sup>132</sup> Other than that, Wang et al. reported that, by using dopamine as the reductant, sub-molybdenum-oxides with various chemical ratio can be prepared (Figure 9a).<sup>133</sup> Firstly, according to the electrochemical measurement, it reveals that the oxidation potential of dopamine decreases with the increase of the pH values. Therefore, in the experiment of MoO<sub>3</sub> reduction, the pH value of the MoO<sub>3</sub> and dopamine mixture solution was controlled, and then MoO<sub>3-x</sub> nanosheets with tunable localized surface plasmon resonance (LSPR) from ultraviolet to the near-infrared region (361-809 nm) could be

achieved, which also reflected on the colour change of the nanosheets that from deep blue, faint bluish, orange, yellow to black (Figure 9b-c). Moreover, in Figure 9d, it also reveals that dopamine can act as a protective surfactant, and forms polydopamine (PDA) coated  $\text{MoO}_x$ , which prevents the  $\text{MoO}_x$  from being oxidized even in the strong oxidants. Additionally, reductants such as ascorbic acid (AA), polyethylene glycol (PEG), glucose, ethanol etc. also have been extensively used to tune the oxygen vacancy density, and remarkable successes on tuning the oxygen vacancies have been obtained, however, using of these organic reductants always introduce undesirable radicals on the material surface, which may degrade the SERS performance.<sup>134, 135</sup>

Moreover, electro-deposition method owns plenty of advantages on preparing thin film, e.g., precise control of film's stoichiometry and layer thickness, low reaction temperatures, large-scale uniformity and cost effectiveness, therefore, it also has been widely implemented for  $\text{MoO}_x$  preparation. Experimentally, through tuning the deposition parameters, e.g., pulse voltage, current density, electrolyte and electrodes, the oxygen vacancy density of the deposited film can be conveniently manipulated. For instance, in the steps of electrodeposition of the oxygen deficient  $\text{MoO}_x$ , a three-electrode electrodeposition system configured with Pt wire (counter electrode), ITO glass (working electrode), and Ag/AgCl (reference electrode) were used (Figure 10a). Using the  $\text{MoO}_3$  colloid as the electrolyte, voltage pulse of 3 seconds and current density of  $0.03 \text{ mA cm}^{-2}$  was set as the deposition parameter. After 1200 deposition cycles, XPS detection on the deposited molybdenum oxides reveals that  $\text{MoO}_{2+x}$  film with 61% of  $\text{Mo}^{6+}$  ion and 39% of  $\text{Mo}^{5+}$  is achieved (Figure 10b and c).<sup>136</sup>

Semiconductor process technologies, such as chemical vapor deposition (CVD), magnetic sputtering, pulse laser deposition and thermal evaporation, are commonly used to tune the oxygen vacancy defects. Relying on the advantage of CVD, Wu et al. reported a kind of ultra-thin layer  $\text{MoO}_2$  nanosheets prepared on the  $\text{SiO}_2$  via CVD process.<sup>89</sup> In the experiment,  $\text{MoO}_3$  powder was first deposited on the  $\text{SiO}_2$  at  $750 \text{ }^\circ\text{C}$  for 30 minutes in the furnace by using the  $\text{N}_2$  as the carrying gas, then sulfur (S) source was heated to  $90 \text{ }^\circ\text{C}$ , and the evaporated S reacted with O element in  $\text{MoO}_3$  to create the oxygen vacancy (Figure 11a). Raman spectra of the prepared thin film are collected. As shown in the Figure 11b, the Raman peaks at  $124, 208, 230, 347, 363$  and  $498 \text{ cm}^{-1}$  can be assigned to the vibration modes of  $\text{MoO}_2$ , indicating the successful deposition of  $\text{MoO}_2$  thin film. In the meanwhile, XPS detection in the Figure 11c also reveals the strong peak intensity of  $\text{Mo}^{4+}$  ion, which further confirms the formation of  $\text{MoO}_2$ .

Other than that, the pulse laser deposition method is also used to shape the oxygen vacancy defect distribution in the  $\text{MoO}_3$  through controlling the deposition temperature and oxygen partial pressure. In Khojier et al. research work,  $\text{MoO}_3$  was used as the target, different chamber temperatures and pressures were set during the process for the purpose of depositing  $\text{MoO}_x$  film with different oxygen vacancy density.<sup>137</sup> XRD is performed to investigate the  $\text{MoO}_x$  film obtained under

different process conditions. It shows in Figure 12a that the condition of 500/4.5 (500  $^\circ\text{C}$ , 4.5 Pa) allows the formation of orthorhombic  $\text{MoO}_3$ , however, it also shows some reflections of the  $\text{Mo}_4\text{O}_{11}$  phase, representing the formation of mixed-phase  $\text{MoO}_x$  film. Moreover, for lower deposition pressure, the film prepared under 500/2.4 (500  $^\circ\text{C}$ , 2.4 Pa) condition has reflections of  $\text{Mo}_4\text{O}_{11}$  and  $\text{MoO}_2$ , and in the process condition of 570/2.4 (570  $^\circ\text{C}$ , 2.4 Pa) film, it shows strong  $\text{MoO}_2$  reflections and faint reflections of  $\text{Mo}_4\text{O}_{11}$  (Figure 12b). The above characterization results prove the importance of the temperature as well as the  $\text{O}_2$  partial pressure on forming the oxides with different stoichiometry. In addition, XPS detection reveals more information of the material component. It illustrates in Figure 12c that, for the  $\text{MoO}_x$  deposited at 500/4.5 condition, about 13.8% of the Mo ions are  $\text{Mo}^{5+}$ , and 86.2% of the ions are  $\text{Mo}^{6+}$ . Whereas, for the  $\text{MoO}_x$  deposited at 500/2.4,  $\text{Mo}^{4+}$  ions occupy about 0.5% of the Mo ions,  $\text{Mo}^{5+}$  ions occupy another 39.4%, and the rest are  $\text{Mo}^{6+}$  ions. In the end, for the  $\text{MoO}_x$  deposited at 570/2.4, about 39.5% are  $\text{Mo}^{4+}$  ions, 31.6% of them are  $\text{Mo}^{5+}$  ions and the rest are  $\text{Mo}^{6+}$  ions. Besides, oxygen vacancies also can be created by introducing N element in the  $\text{MoO}_x$ . In the literature, the  $\text{MoO}_3$  film is annealed in ammonia or  $\text{N}_2$  atmosphere. It is demonstrated that substitution of N in the crystal introduces abundant vacancy defects into  $\text{MoO}_3$ , resulting in the enhancement of the electrical conductivity.<sup>138, 139</sup>

Recently, light irradiation is considered as an effective strategy for creating oxygen vacancies in the oxide. Previous experiment indicates that active radicals like  $\text{H}^\cdot$  and  $\text{OH}^\cdot$  can be created from  $\text{H}_2\text{O}$  in the catalytic reaction with the presence of  $\text{MoO}_3$  under the light illumination, thereafter, substantial number of the  $\text{H}^\cdot$  ions diffuse into the layered  $\text{MoO}_3$ , forming the  $\text{OH}_2$  species, and then excessive  $\text{OH}_2$  species dissociate away from the crystal, which ultimately results in the formation of oxygen vacancies (Figure 13a and b).<sup>95, 140-142</sup> Raman spectra are used in the experiment to monitor the evolution of 2D  $\text{MoO}_x$  suspensions under different solar light irradiation time, it shows in Figure 13c that, for the initial sample that associated to  $\alpha\text{-MoO}_3$ , Raman peaks at  $280, 667, 816$  and  $991 \text{ cm}^{-1}$  are observed, which is in good agreement with the vibration modes of  $\alpha\text{-MoO}_3$ . And after 5 hours of solar light exposure, the formation of oxygen vacancies is confirmed that Raman peaks at  $489$  and  $740 \text{ cm}^{-1}$  appear, which are assigned to the stretching mode of  $\text{Mo}=\text{O}$  and  $\text{Mo}-\text{O}-\text{Mo}$ , evidencing the creation of  $\text{MoO}_{3-x}$  in the solution.

### Ion Doping and Intercalation

Doping with extrinsic defects in the  $\text{MoO}_3$  introduces extra energy levels in the band gap of  $\text{MoO}_3$  material as well. Lambert et al. performed DFT calculation to investigate the solubility and effect on the band structure of different metal ions doping in the  $\text{MoO}_3$ . It reveals in Figure 14a and b that Sc, Ti and Y have limited solubility within a wide range of  $\text{O}_2$  partial pressure at the temperature of 500 K, and thus they are restricted for efficient defect tuning. Meanwhile, Zn, Cu and Se show some solubility, especially Cu and Se appear to introduce defect levels near the valence band. On the



other hand, Mn and V are found to be highly soluble in the MoO<sub>3</sub>, and substitutional or interstitial type of defects can be formed in a wide range of doping concentrations. In the meanwhile, band structure calculation result in Figure 14c further evidences that the Mn and V atoms (Mn<sub>i</sub> or V<sub>i</sub>) in the interstitial position tend to introduce mid-gap states in the MoO<sub>3</sub> crystal, whereas a substitutional Mn (Mn<sub>Mo</sub>) induces extra defect levels near the conduction band. To the contrary, defect levels originate from the substitutional V are closer to the valance band.<sup>143</sup>

Additionally, Sn<sup>2+</sup> ions are implemented as dopant to tune the MoO<sub>3</sub> material properties, and either interstitial or substitutional defects are created, introducing wide-distributed defect levels in the band gap. Experimentally, the layered  $\alpha$ -MoO<sub>3</sub> nanosheets were prepared by PVD method. And in order to achieve the Sn<sup>2+</sup> intercalation, the  $\alpha$ -MoO<sub>3</sub> were dipped into the beaker with deionized water solution containing 10 mM SnCl<sub>2</sub> and 100 mM tartaric acid, then the mixed solution was heated at 60 °C for more than 15 minutes, thereafter the MoO<sub>3</sub>-Sn samples were rinsed with acetone and deionized water to get rid of other impurities absorbed on surface of sample (Figure 15a and b). UV-vis spectra shown in the Figure 15c first reveal that the absorption intensity is enhanced significantly in a broad wavelength range from 300 to 15000 nm, which is ascribed to charge transfer from Sn<sup>2+</sup> ions to the Mo<sup>6+</sup> ions. Thereafter, XPS measurement is further implemented to investigate the atomic details of the material properties. It shows that, after the introducing of Sn<sup>2+</sup> ions in the MoO<sub>3</sub>, both Mo 3d 5/2 and 3d 3/2 peaks are split into doublets, arising from the presence of Mo +5 and +6 oxidation states. And in the meanwhile, it also indicates that Sn<sup>2+</sup> ions are oxidized into Sn<sup>4+</sup> ions, confirming the electrons are transferred from the Sn<sup>2+</sup> ions to the Mo<sup>6+</sup> ions (Figure 15d).<sup>144</sup>

Other than that, Nb or Ti doping via spray pyrolysis in the MoO<sub>x</sub> also shows profound influence on the optical and electronic properties of MoO<sub>3</sub>.<sup>145, 146</sup> It manifests that the dopants induce extra defect levels near the conduction band of the MoO<sub>3</sub>, promoting electron intervalence transfer between Mo and dopants. Besides, the above doping process also works for the other metal doping in the MoO<sub>3</sub>. For example, it has been confirmed that elements like Li, Na, K, Nb, W, Fe, Cd, Ce and Eu ions generate additional energy levels in the band gap, reducing the intrinsically wide band gap of MoO<sub>3</sub>.<sup>147-153</sup> However, In-doped MoO<sub>3</sub> is found to be transformed into a p-type semiconductor with an increased band gap of ~3.8 eV.<sup>154</sup> This phenomenon also is found in the Ru-doped MoO<sub>3</sub>, which is considered to be caused by induced structural defects during the doping process.<sup>155</sup>

Furthermore, H<sup>+</sup> ions are also extensively used as a dopant to engineer the MoO<sub>3</sub> material property. For the reason of its tiny atom size and single valence electron, introducing H<sup>+</sup> ions in the crystal structure only induces insignificant structural expansion in the MoO<sub>3</sub> with relatively low migration barrier, and plenty of researches have been performed to study the intercalation of hydrogen in the MoO<sub>3</sub> as the dopant.<sup>156-158</sup> Usually, method of preparing hydrogen molybdenum bronze (H<sub>x</sub>MoO<sub>3</sub>) is via the chemical reaction in acid aqueous solution.<sup>136, 140, 159</sup> It shows that the H<sup>+</sup> ions prefer to attach to the O and form the hydroxyl-like radicals, introducing intrinsic defects and contributing excessive electrons to the material. More specifically,

based on the intercalated H<sup>+</sup> ion concentration (the concentration is still low if compared to that in the oxygen-vacancy formation), three thermodynamically stable phases of H<sub>x</sub>MoO<sub>3</sub> can be determined, which are shown in Figure 16a, including type 1 (0.23 < x < 0.40), type 2 (0.85 < x < 1.04) and type 3 (1.55 < x < 1.72). In type 1 H<sub>x</sub>MoO<sub>3</sub>, the intercalated H<sup>+</sup> ions are relatively low, and therefore the H<sub>x</sub>MoO<sub>3</sub> remains the orthorhombic crystal phase, showing blue colour. However, with the increase of the intercalated H<sup>+</sup> ion amounts, it forms type 2 or type 3 H<sub>x</sub>MoO<sub>3</sub>, and the crystal phase may evolve from orthorhombic into monoclinic phase, while the colour converts to green (Figure 16b). In the meanwhile, XPS valence spectrum analysis shown in Figure 16c indicates that the valence band edge is determined to be ~3eV away from the Fermi level for MoO<sub>3</sub>, however, weak humps are also detected for the H<sub>0.3</sub>MoO<sub>3</sub>, H<sub>0.91</sub>MoO<sub>3</sub> and H<sub>1.55</sub>MoO<sub>3</sub> between the valence band edge and the Fermi level. Physically, these peaks are ascribed to the overlap of the electron wave function induced by free electrons from the intercalated H<sup>+</sup> ions, further revealing the strong interaction of the H<sup>+</sup> ions with the crystal and ultimately shifting up the Fermi level.

In addition to that, the advantage of strong light-material interaction between the incident light and MoO<sub>3</sub> is exploited to introduce H<sup>+</sup> ions into the MoO<sub>3</sub> as well. MoO<sub>x</sub> nano flakes were first prepared by a liquid exfoliation method, and three kinds of MoO<sub>x</sub> nanoflaks aqueous suspensions (MoO<sub>x</sub>-I, MoO<sub>x</sub>-II and MoO<sub>x</sub>-III) were obtained from the precursors with different MoO<sub>3</sub> and Mo weight ratio (MoO<sub>3</sub>, 4MoO<sub>3</sub>:1MoO<sub>2</sub> and 1MoO<sub>3</sub>:4MoO<sub>2</sub>). Then, a solar simulator source was used to irradiate the precursors in the experiment. Experiment results show that the MoO<sub>x</sub> aqueous suspension under the light irradiation can create rich hydroxyl groups in the MoO<sub>3</sub> through H<sup>+</sup> intercalation process, inducing the electron transfer from the O to Mo. Subsequently, the terminal oxygen atoms transferred charges to the bonding Mo atoms, resulting in partial reduction of molybdenum ions and shortening of Mo-O bonds, which simultaneously leads to the introducing of the defect levels in the MoO<sub>3</sub> band gap (Figure 17).<sup>141, 160</sup> Besides, spill-over method, electron-proton co-doping strategy or annealing in the H<sub>2</sub>, are also widely implemented, and they show excellent hydrogen introducing efficiency in the MoO<sub>3</sub>, consequently promoting the free carrier concentration significantly.<sup>49, 95, 161</sup>

### Crystal Phase Control

Molybdenum oxides possess various crystal phases, showing diverse optical and electronic properties, therefore, it could be an attractive approach to manipulate the crystal phase for specific optical applications.<sup>126</sup> In a reported experiment, a novel solvothermal method was implemented to synthesize MoO<sub>x</sub> nanomaterials. Specifically, MoS<sub>2</sub> dispersed in ethanol was used as precursor, and H<sub>2</sub>O<sub>2</sub> was used as the oxidant. Through reaction time control, monoclinic MoO<sub>2</sub> (JCPDS No. 32-0671) was achieved in the first-time phase, then with the extending of the reaction time, non-stoichiometric structure of MoO<sub>3-x</sub> (Mo<sub>4</sub>O<sub>11</sub>) nanoparticles and the stoichiometric structure of MoO<sub>3</sub> nanoparticles were obtained (Figure 18a).<sup>162</sup> Physical characterizations of XRD and XPS detections indicate

that the material properties closely rely on the synthetic condition. It reveals that monoclinic MoO<sub>2</sub> nanoparticles with sufficient oxygen-rich groups have been prepared in the first stage, whereas MoO<sub>3-x</sub> nanoparticles that contain less vacancy defect are obtained in the second stage, and stoichiometric MoO<sub>3</sub> nanoparticles are synthesized in the end. In addition, UV-vis absorption investigation in Figure 18b illustrates that MoO<sub>2</sub> nanoparticles appear intense absorption from visible to NIR with the peak located at 795 nm, which is produced by the strong LSPR effect induced by the d-orbital free electrons from oxygen vacancies. On the other hand, MoO<sub>3-x</sub> nanoparticles with less defect density show a weaker and narrower absorption profile within the mild visible range, whereas MoO<sub>3</sub> nanoparticles appear no absorption from the visible to NIR region, indicating the low free electron density in these two materials. Besides, an alkaline solution (NH<sub>4</sub><sup>+</sup> solution) is also implemented to tune the alkaline of the electrolysis. By optimizing the doping level of NH<sub>4</sub><sup>+</sup> in the MoO<sub>3</sub> crystal solution, it shows that highly crystalline orthorhombic 2D molybdenum oxide transits to hexagonal phase (Figure 18c).<sup>163</sup>

Other than that, early study reveals that amorphous ZnO NCs-molecules system is able to promote the interfacial charge-transfer process (ICTP), consequently improving the semiconductor-based SERS performance significantly. Therefore, Li et al. presented a quantum size H<sub>x</sub>MoO<sub>3</sub> for the similar ICTP property. In a typical experiment, MoS<sub>2</sub> powder was first oxidized in the H<sub>2</sub>O<sub>2</sub> solution, and then the mixed solution was quickly transferred into a stainless-steel autoclave with the supercritical CO<sub>2</sub>.<sup>164</sup> Through heating it at 40 °C for 3 hours, the CO<sub>2</sub> was released, and supernatant of MoO<sub>3</sub> quantum dots were collected for the further experiment. Thereafter, illumination process was conducted with sunlight for 5 hours, the H<sup>+</sup> ions in the solution intercalated into MoO<sub>3</sub> and formed H<sub>x</sub>MoO<sub>3</sub> quantum dots (Figure 19a). It shows in Figure 19b that the prepared H<sub>x</sub>MoO<sub>3</sub> quantum dots are with the average physical size of 4 nm, and no lattice diffraction fringe is observed. Moreover, the UV-vis spectra in Figure 19c reveal that the quantum dots show dual optical absorption peaks, which is attributed to the increase of the surface carrier density produced by the quantum size constrain.

### MoO<sub>x</sub> Hybrids Formation

Molybdenum oxide can be prepared by various chemical synthesis and physical deposition methods, therefore, it enables the researchers to integrate proper preparation processes to obtain MoO<sub>x</sub> hybrids, pursuing enhanced optical functions. In the most recent research work, Li et al. prepared molybdenum tungsten oxide hybrids (MWO) with strong plasmonic resonance property.<sup>165</sup> Tungsten oxides (WO<sub>x</sub>) are transitional oxide material, and widely used for electrochromic glass, photocatalysis and sensing application. It shows in literature that rich substoichiometric compositions of WO<sub>x</sub> with tunable LSPR properties can be obtained by various types of defect engineering approaches. Thus, in order to reinforce the plasmonic vibration of both WO<sub>x</sub> and MoO<sub>x</sub>, MWO hybrids are synthesized by using the one-pot solvothermal solution method. The prepared hybrids are in black-blue colour due to the high density of oxygen vacancies,

which are reduced by the 2-propanol during the reaction. In the meanwhile, the Mo and W ions also tend to enter into each other's octahedral structures, creating extra defects in the MWO (Figure 20a). UV-vis absorption spectra are collected, and it shows broad and strong LSPR effect >400 nm (Figure 20b), deriving from the high concentration of free electrons. In addition to that, Mo/MoO<sub>2</sub> and MoS<sub>2</sub>/MoO<sub>x</sub> hybrids are prepared, and experiment characterizations manifest that hybridizing two materials significantly promote the free electron density, consequently enhance the SPR intensity.<sup>166, 167</sup> In the meanwhile, MoO<sub>2</sub>/graphene oxide hybrids (MoO<sub>2</sub>/GO) are also reported in the publication. The hydrothermal reaction is implemented to synthesize the hybrids by Chen et al., and it shows in Figure 20c that MoO<sub>2</sub> nanoparticles are completely covered by the ultra-thin GO.<sup>168</sup> UV-vis absorption spectra are recorded and show broad absorption peaks centred at 650 nm, revealing the strong LSPR resonance produced by the MoO<sub>2</sub> nano particles. Moreover, rich absorption peaks from FTIR spectra further suggest the presence of the abundance of carboxyl and hydroxyl groups on the surface of GO. Therefore, the constructing of above MoO<sub>2</sub>/GO hybrids not only retains the LSPR property of MoO<sub>2</sub> nanoparticles, and also raises the absorption density of target prober molecules by the GO covering. Besides, Achadu et al. also prepared Fe<sub>3</sub>O<sub>4</sub> functionalized MoO<sub>3</sub> nanocubes as the nanotags and graphene as substrate. By exploiting the plasmonic property of the MoO<sub>3</sub> nanocubes, a reliable hybrids biosensing system based on the immunoassay protocol is constructed for virus detection.<sup>169</sup>

Furthermore, MoO<sub>x</sub> and noble metal hybrids (MoO<sub>x</sub>/Au, MoO<sub>x</sub>/Ag) are reported by researchers for the purpose of utilizing the merits of noble metal and oxide in SERS detection.<sup>170-172</sup> In Guo et al. research work, they took the advantage of low valence state of the Mo ions, chloroauric acid (HAuCl<sub>4</sub>) was directly added into the MoO<sub>x</sub> solution, and MoO<sub>x</sub>-Au hybrids were synthesized by heating the mixture at 100 °C for 2 minutes. SEM investigation in Figure 20d confirms the formation of the MoO<sub>x</sub>/Au hybrids. In the meanwhile, the UV-vis absorption spectra also appear dual absorption peaks that are derived from LSPR resonance of the Au nanoparticle and MoO<sub>x</sub> nanoparticles, which strengthens the SPR intensity as well as expands the LSPR frequency band. In the meanwhile, similar MoO<sub>x</sub> and noble metal hybrids also can be prepared by UV light irradiation or adding weak reductant in the solution and same improvement on the SPR intensity is achieved, too.

### SERS Mechanism and Performance of the Defective MoO<sub>x</sub>

The SERS effect on the surface of the metal oxides was first observed in the 1980s. In the early years, due to the limitations of semiconductor synthesis and characterization technologies, this phenomenon was detected only on several semiconductor surfaces, such as NiO, GaP, and TiO<sub>2</sub>, and the Raman enhancement on these semiconductors is found relatively weak. Nevertheless, with the progress of the material preparation and tuning technologies, SERS study on oxide-semiconductor surface has undergone a remarkable growth, especially it is found that the SERS performance on transition metal oxides can be comparable with that of noble

metal. However, there are still extensive debates on the SERS mechanisms and SERS performance evaluation, therefore, in the subsequent part of the article, the SERS mechanism and SERS performance of the MoO<sub>x</sub> will be reviewed.

### SERS Mechanism of the Defective MoO<sub>x</sub>

It is known from the theory that Raman signal intensity is closely related to the incident field intensity and polarizability derivative, therefore, two mechanisms for SERS are always discussed, namely electromagnetic enhancement mechanism (EM) and chemical enhancement mechanism (CM).<sup>173</sup> The EM of the SERS involves the electromagnetic field intensity enhancement, which is produced from the surface plasmon resonance excitation. On the other hand, the CM of SERS originates from the molecule polarizability enhancement, which is attributed to the charge transfer between the SERS substrate and molecules.

The plasmon resonance of the material is strongly correlated to the free electron density, and according to the Drude-Lorentz model, it can be estimated as follows:

$$\omega_p = \sqrt{\frac{ne^2}{\epsilon_0 m_e}}$$

Where  $\omega_p$  is the bulk plasmon resonance frequency.<sup>140</sup> Previously, the surface plasmon resonance excited by the visible light is only found on noble metals. However, the progress on preparing and tuning oxide semiconductor enormously expands the plasmonic material selection. Today, it is shown that a series of substoichiometry oxide-semiconductors also show surface plasmonic resonance that excited by the visible light range, which is ascribed to the promoted free electron density obtained via defect engineering. Especially for the MoO<sub>x</sub>, widely tunable localized surface plasmon resonance (LSPR) can be achieved by defect engineering. And plenty of SERS studies have observed the strong EM that originates from the surficial electromagnetic field generated by the defective MoO<sub>x</sub>, which enhances the molecular Raman signal intensity to several orders higher than that on normal substrate.

On the other hand, theoretical and experimental evidence also reveals that the defective MoO<sub>x</sub> possesses rich defect levels in the band gap. Thus, it provides multi-step defect levels to facilitate the charge transfer between the oxide-semiconductor SERS substrate and molecules, and ultimately promotes the molecular polarizability, which is considered as the CM. In a typical experiment, electrons in the ground states gain enough energy by absorbing the incident photon under the specific laser wavelength, and then these excited electrons are transferred to the molecules through the coupled energy level and enhance the polarizability of the molecule, which results in the chemical enhancement of the molecular Raman signal intensity.

Both EM and CM are important for the performance of MoO<sub>x</sub> SERS substrate, however, previous studies indicate that the SERS contributed by EM is always effective when the

distance between the substrate and molecules is within the evanescent distance of the surface electromagnetic field, whereas CM only happens when a junction is formed between the substrate and the molecules.

### SERS Performance of the Defective MoO<sub>x</sub>

In the early days, the SERS phenomenon exclusively relies on the EM observed on the noble metals, until recently, heavily doped semiconductor materials are successfully prepared, and they also show prominent EM enhancement. In a reported research work, an 8-nm thick MoO<sub>2</sub> film with metallic character is prepared by CVD technique and implemented as the SERS substrate. It shows in Figure 21a that a lowest detection concentration of  $4 \times 10^{-8}$  M and enhancement factor of  $2.1 \times 10^5$  can be obtained, which exceeds that of other 2D materials and is comparable to that of noble metal films. Moreover, the Raman signal mapping results also reveal excellent uniformity. It shows Figure 21b that the RSD of Raman peaks in a  $5 \times 5 \mu\text{m}^2$  area can reach 4.89% (914 cm<sup>-1</sup>), 5.706% (1182 cm<sup>-1</sup>), and 5.513% (1622 cm<sup>-1</sup>), respectively (Figure 21b). Furthermore, as it can be observed in Figure 21c, the planar MoO<sub>2</sub> substrate is more environmental stability compared to that of the noble metals, experimental evidence indicates that even 15-day in the air, the ultra-thin MoO<sub>2</sub> nanosheets still retain the nearly the same. In the meanwhile, the CVD prepared ultrathin film also shows extraordinary temperature stability. It reveals in Figure 21d that the shape and SERS performance of MoO<sub>2</sub> nanosheet remains when the nanosheets undergo the heating treatment at 200 °C for 1 hour. Moreover, Raman measurement demonstrates that the analysts on the surface can be removed by annealing and then the substrate can be reused for more than 10 cycles, showing the excellent reusability. In the end, first principle calculation is performed to understand the SERS mechanism of this ultrathin MoO<sub>2</sub>. It reveals that MoO<sub>2</sub> presents a metallic character and significant absorption band at 510 nm, both of which can be attributed to the SPR effect (EM) induced by the free electrons, and consequently promotes the SERS performance.<sup>89</sup>

Additionally, the plasmonic properties of the MoO<sub>x</sub> are also impacted by their surface states and microstructure. In the experiment, a one-pot and facile solvothermal method by adjusting the synthesis time to prepare different phases of MoO<sub>x</sub> nanomaterials is implemented. Practically, MoO<sub>2</sub> (5 hours), MoO<sub>3-x</sub> (7 hours) and MoO<sub>3</sub> (11 hours) phases of nanoparticles are synthesized by oxidizing the bulk MoS<sub>2</sub> powder through reaction time control. Meanwhile, UV-vis absorption spectra obtained from the three different phases nanoparticles illustrate that MoO<sub>2</sub> nanoparticles display strong SPR absorption in the visible and NIR region, however, MoO<sub>3-x</sub> nanoparticles show much weaker LSPR effect, and no LSPR effect is observed for the MoO<sub>3</sub> nanoparticles. The SERS activity is evaluated on the above three different phase nanoparticles. Figure 22a shows that MoO<sub>2</sub> nanoparticles exhibit superior SERS effect than that of the MoO<sub>3-x</sub> and MoO<sub>3</sub> nanoparticles, which is ascribed to the strong LSPR induced by the high oxide vacancy density in the material with shorter reaction time and consequently promotes the EM.

Furthermore, SERS performance of the plasmonic MoO<sub>2</sub> nanoparticles substrate is evaluated by probing the molecules of R6G with different concentrations. It can be observed in Figure 22b and c that the minimum detection concentration of 5×10<sup>-8</sup> M and the maximum EF up to 1.10×10<sup>7</sup> can be achieved, which even reaches that of noble metals.<sup>162</sup>

Other than the EM mechanism, CM is widely exploited to achieve attractive SERS performance. Research work performed by Ma et al. used light to engineer the defect density of the MoO<sub>3-x</sub>. In the first place, MoO<sub>3-x</sub> nanosheets are prepared at the room-temperature by oxidizing the molybdenum powder with H<sub>2</sub>O<sub>2</sub>, and subsequently the prepared molybdenum oxides are irradiated by the light in methanol to induce the reduction. Physical and optical detections are performed. It confirms that MoO<sub>3-x</sub> nanosheets are in amorphous state. In the meanwhile, UV-vis absorption spectra in Figure 23a further reveal that amorphous MoO<sub>3-x</sub> nanosheets display a strong and wide absorption band from 700 to 1200 nm, which is ascribed to the high-level electrons doping from the oxygen vacancies generated during the Xe irradiation phase. SERS performance is evaluated by using a variety of molecules, e.g., MB, RhB and PNTP. As shown in Figure 23b, it demonstrates that the substrate prepared by amorphous MoO<sub>3-x</sub> sheets show more efficient charge transfer capability compared to that of crystal MoO<sub>3-x</sub>, and using the R6G as the Raman reporter (Figure 23c), it can be observed that attractive SERS performance induced by the CM can be obtained for the amorphous MoO<sub>3-x</sub> nanosheets under the 532 nm laser irradiation, which also exhibits higher sensitivity than the crystalline MoO<sub>3-x</sub>. Moreover, in Figure 23d, the recycling detection of the amorphous MoO<sub>3-x</sub> nanosheets is investigated by repeated oxygen insertion in the H<sub>2</sub>O<sub>2</sub> solution and extraction through light-irradiation reduction in methanol. Comparing to the crystalline MoO<sub>3-x</sub>, SERS activity of the a-MoO<sub>3-x</sub> sheets keep stable upon 5 cycles. This unique SERS property allows the recycling use of the substrate through H<sub>2</sub>O<sub>2</sub>-based Fenton-like reaction.<sup>174</sup>

The plasmonic characteristics of the MoO<sub>x</sub> determine the SERS performance, and preparation of tunable and stable plasmonic MoO<sub>x</sub> attracts a lot of interests. Therefore, using a polydopamine (PDA) as the surface coating, MoO<sub>x</sub> nanosheets with the LSPR from the ultraviolet to the near-infrared region (361-809 nm) are prepared through changing the pH value of the reaction solution (Figure 9b).<sup>131</sup> SERS performance is compared between the blue (lower free electron density) and yellow MoO<sub>3-x</sub> nanosheets (higher free electron density, Figure 24a). Using the 532 nm laser as the excitation source, it illustrates in the Figure 24b that the blue MoO<sub>3-x</sub> nanosheets achieve the limit of detection of 0.3 fM when rhodamine 6G (R6G) is used as dye, and the corresponding Raman enhancement factor is calculated to be 1×10<sup>10</sup>. On the other hand, the yellow MoO<sub>3-x</sub> nanosheets show much insignificant Raman signal enhancement (Figure 24c). In view of the experiment evidence, the SERS mechanism of the above MoO<sub>3-x</sub> nanosheets are discussed. Firstly, it manifests that the Raman signal enhancement of the MoO<sub>3-x</sub> nanosheets contributed by the LSPR is insignificant, which can be ascribed to the weak

surface electromagnetic field induced by the LSPR at both two resonance frequency. However, at this stage, it is observed on the SERS spectra of R6G that the vibrational modes at 612 cm<sup>-1</sup> and 773 cm<sup>-1</sup> are highly promoted, which suggests the critical role of CM. Therefore, in the next investigation, the energy band is calculated, it reveals that the valence band (VB) and conduction band (CB) are well-aligned with the HOMO and LUMO of the R6G, and consequently triggers charge transfer resonances between the nanosheets and R6G, inducing the remarkable Raman signal improvement (Figure 24d). Moreover, PDA-coated MoO<sub>3-x</sub> further shows strong resistant to high concentration of oxidant, such as H<sub>2</sub>O<sub>2</sub> and NaClO, it demonstrates that the optical dispersion of the material can be remained, showing excellent stability for harsh environment detection application.<sup>133</sup>

Other than that, MoS<sub>2-x</sub>-MoO<sub>x</sub> complex materials also exhibit encouraging SERS capability. Zheng et al. reported a kind of MoS<sub>2-x</sub>-MoO<sub>x</sub> mixed phase material prepared through oxygen incorporation into MoS<sub>2</sub> (Figure 25a and b), and SERS measurement reveals that the substrate prepared by the MoS<sub>2-x</sub>-MoO<sub>x</sub> mixed phase material can have 10,000 times of SERS intensity improvement compared to that of the pristine MoS<sub>2</sub> (Figure 25c). Additionally, annealing treatment of the MoS<sub>2-x</sub>-MoO<sub>x</sub> mixed phase at 300 °C for 40 min brings extra oxygen in the material, and gives 100,000 times higher SERS intensity when referring to the pristine MoS<sub>2</sub> (Figure 25c). Mechanism investigation is then conducted, as it is shown in Figure 25d, oxygen incorporation in the MoS<sub>2</sub> creates additional energy levels, which promotes the charge transfer between semiconductor and analyte molecule. Besides, it also points out that the improvement of exciton resonances on the semiconductor and molecule produces stronger intensity, which further boosts the charge-transfer resonance in the semiconductor-molecule system.<sup>166</sup>

Furthermore, for a typical MoO<sub>x</sub> based SERS substrate, it is observed that both the EM and CM contribute to the SERS enhancement significantly. For instance, a kind of monoclinic-phase MoO<sub>2</sub> nano-dumbbell was prepared by a hydrothermal method (Figure 26a). First principle calculation reveals the metallic characteristics of the MoO<sub>2</sub>. In the meanwhile, UV-vis absorption spectra in Figure 26a also show strong and well-defined SPR peaks, which are attributed to the high concentration of free electrons in the MoO<sub>2</sub>. The SERS performance is then evaluated by using the R6G as the Raman reporter (Figure 26b), it shows in Figure 26c that the MoO<sub>2</sub> substrate owns the EF of 3.75×10<sup>6</sup> and high detection sensitivity of 10<sup>-7</sup> M. Besides, the MoO<sub>2</sub> nano-dumbbell also shows extremely stability under the harsh environment. It illustrates in Figure 26d that the absorption curve of the MoO<sub>2</sub> substrate can sustain even after 300 °C annealing in the air. In the end, the SERS enhancement mechanism is discussed. Other than the EM effect, it reveals from the absorption spectra of the R6G-modified MoO<sub>2</sub> substrates that new absorption bands at 349, 485, 536, 580 and 732 nm appear, indicating the coexistence of the charge transfer (CM) between the substrate and molecules.<sup>175</sup>

In addition, amorphous  $H_xMoO_3$  quantum dots possess rich surface defects, and the plasmonic property investigation manifests that they appear dual and strong SPR peaks at 720 and 1050 nm, which can be attributed to the high free electron density from the defects that are confined in a quantum sized dot. The SERS performance of the amorphous  $H_xMoO_3$  quantum dots is evaluated by using the MB as Raman reporter. It shows that the ultrahigh EF of  $9.5 \times 10^5$  and limit of detection to  $10^{-9}$  M can be obtained on amorphous  $H_xMoO_3$  quantum dots when MB is used as the Raman reporter (Figure 27a and b). Such a remarkable SERS performance is also shown when R6G and RhB are used as Raman reporter, which suggests that the amorphous  $H_xMoO_3$  quantum dots not only generate intensive surface electromagnetic field, but also promote the charge transfer, and thus shows extremely low trace molecule detection capability. In the meanwhile, the mechanism of the exceptional SERS property of the  $H_xMoO_3$  quantum dots is discussed, it indicates that the small size of  $H_xMoO_3$  quantum dots can benefit the absorption process of azo dyes, and consequently enhance the interaction between them (Figure 27c).<sup>164</sup>

Additionally,  $MoO_x$  can be prepared by various chemical and physical deposition methods, thus, researchers have integrated proper preparation methods to obtain  $MoO_x$  hybrids, pursuing prominent SERS performance by taking the advantage of individual components. In Li et al. research work, they prepared molybdenum tungsten oxide hybrids (MWO) for the purpose of integrating the excellent SERS performance of tungsten oxide and molybdenum oxide. Firstly, as it illustrates in Figure 20b that the measured UV-vis absorption spectra show high and broad absorption peak centred at 552 nm that is ascribed to high concentration of free electrons produced by the oxygen vacancy defects in the MWO hybrids, and then the SERS performance is measured by using the R6G as the probe molecules. Clearly, it can be observed in Figure 28a that the SERS signal obtained on R6G@MWO is greatly improved, and the EF of the MWO can reach  $10^7$  with the detection limit of  $10^{-8}$  M (Figure 28b). Moreover, the enhancement mechanism of the MWO is discussed, since both tungsten oxides and molybdenum oxides possess the EM and CM characteristics, therefore, a thin PVP layer is coated on the MWO to block the charge transfer between substrate and molecule, and the SERS spectra are measured again. It shows obviously in Figure 28c that the signal is severely reduced when only the EM contributes to the enhancement. And through the calculation, it reveals in Figure 28d that, due to the high oxygen vacancy defect density, the CM generates more than 50% of the SERS signal enhancement, while the EM from the MWO hybrids contributes the rest enhancement.<sup>165</sup>

To further optimize the CM of the  $MoO_{3-x}$ , in the research work presented by Tan et al., shell-isolated  $MoO_{3-x}@MoO_3$  hybrids were prepared by a solvothermal procedure and then annealing treatment at 200 °C in the air to form the  $MoO_3$  shell. The plasmonic properties of different  $MoO_{3-x}$  nanosheets were evaluated in Figure 29a, it demonstrates that  $MoO_{3-x}$  nanosheets prepared under different annealing conditions show respective SPR frequencies and intensities. Higher temperature at 180 °C generates broader and stronger

absorption peak, indicating much higher free electron concentration in the material. Besides, in the SERS detection of MB with 785 nm laser, it is observed that the SERS intensity of plasmonic  $MoO_{3-x}$  is lower than that observed on the commercial  $MoO_3$ , which is ascribed to photocatalytic activity towards the Raman reporter. Nevertheless, the SERS performance investigation of  $MoO_{3-x}@MoO_3$  shown in Figure 29b reveals a high EF of  $1.42 \times 10^5$  and excellent low detection of limit of  $10^{-7}$  M. Mechanism analysis indicates that the significant SERS performance improvement of the  $MoO_{3-x}@MoO_3$  is produced by the high free carrier density ( $5.3 \times 10^{21} \text{ cm}^{-3}$ ) in the defective bulk  $MoO_x$  and preventing of the photocatalytic degradation of analyte by the non-plasmonic  $MoO_3$  shell (Figure 29c).<sup>176</sup> In addition,  $Fe_3O_4$  functionalized  $MoO_3$  nanocubes were loaded on the graphene substrate through immunoassay reaction, a signal amplification of up to  $\sim 10^9$ -fold was achieved on the above biosensing system, which is ascribed to the combined electromagnetic and chemical mechanisms of the dual SERS nanotag/substrate hybrids system.<sup>169</sup>

On the other hand, ascribed to the reductivity of the low valence Mo ions in  $MoO_x$ , the  $MoO_x$  also can act as an effective reductant with the help of external stimulation (heating or UV irradiation). Research work presented by Guo et al. reported an in-situ reducing of the  $Au^{3+}$  or  $Ag^+$  on the defective  $MoO_x$  NSs to prepare molybdenum oxides/noble metal nanoparticles. In the experiment, the defective  $MoO_x$  NSs showed excellent reducing ability, and by preparing the mixture with different  $HAuCl_4$  volumes, Au nanoparticles ( $Au$ NPs) with different sizes scattered on the nanosheets ( $MoO_x$ - $Au$ NSs) are prepared (Figure 30a) under the light irradiation. Raman evaluation on the  $MoO_x$ - $Au$ NSs reveals that the as-prepared material shows synergistic SERS enhancement produced by both the LSPR enhancement from  $Au$ NPs and enrichment of molecules on  $MoO_x$ - $Au$ NSs ascribed to electrostatic/hydrophobic interaction. In addition, as shown in Figure 30b and c, the IR-780 iodine is used as the Raman reporter, the LOD of  $5 \times 10^{-9}$  M and EF of  $1.7 \times 10^5$  are achieved in aqueous solution. The uniformity of the  $MoO_x$ - $Au$ NSs is also investigated, and it shows that the relative standard deviations (RSD) of 11.76% ( $941 \text{ cm}^{-1}$ ), 7.37% ( $1208 \text{ cm}^{-1}$ ), 6.36% ( $1370 \text{ cm}^{-1}$ ) and 4.37% ( $1468 \text{ cm}^{-1}$ ) can be achieved. Besides, the merits of the  $MoO_x$ /metal hybrids are also reproduced by synthesizing the  $MoO_x/Ag$  NPs and  $MoO_x/Mo$  hybrids, and relying on the synergetic effect of EM and CM, excellent SERS enhancement as well as uniformity is obtained, too.<sup>170-172</sup>

## Challenges and Future Prospects

We have summarized the recent progress on preparing  $MoO_x$  and two main categories of process techniques, vapor-phase deposition and liquid-phase synthesis, are thoroughly presented. Then, in the second part, the emphasis is put on the review for various material engineering strategies to functionalize the  $MoO_x$ . As the compositional and the morphological changes of  $MoO_x$  material critically affect the physical and chemical properties, strategies like vacancy and dopant introducing, phase control and hybrids formation are

presented. Through the review, it shows that significant progress has achieved in the controllable preparation and engineering of MoO<sub>x</sub> with specific properties and structures, which lay a valuable foundation for MoO<sub>x</sub> implemented as SERS substrate. In the fourth part, the SERS mechanism and various SERS applications based on MoO<sub>x</sub> material are reviewed. Relying on the respective MoO<sub>x</sub> material, it shows that the MoO<sub>x</sub> with different morphologies, crystal phases and defect densities own either EM/CM or both of two enhancement mechanisms, and exhibit attractive SERS performance in terms of Raman signal enhancement, large scale uniformity, environment stability and recyclable use.

At this point, it is fair to say that great achievement has been made for the MoO<sub>x</sub> used in the SERS application over the past few years, however, further comprehensive investigation on MoO<sub>x</sub> is still required. One critical issue can be the catalytic degradation phenomenon. As stated in the review, the SERS on the semiconductor oxides depends on the PICT procedure, and higher defect density usually facilitate the charge transfer between the substrate and molecules, however, it is also observed in the experiment that the Raman dyes tend to be photo catalytically degraded, and high density of defects in the oxides generate more active radicals, which further promotes the photo-catalytic process and degrades the SERS sensitivity. Presently, this photo-catalytic issue has attracted researcher's attentions, and some practical solutions have been proposed, however, it is expected that more efforts are still needed to find a better solution. The second obstacle for the MoO<sub>x</sub> used as a flexible SERS sensor lie on the facile tuning method of MoO<sub>x</sub> material properties. Although plethora of methods has been developed, it can be found that most of these methods are implemented before the MoO<sub>x</sub> are fabricated into SERS sensor. Nevertheless, for an advanced and flexible applicable sensor, it is necessary to have the merit that the SERS performance can be in-situ tuned, depending on the detection requirement. Currently, some prototypes of light or electric field tuning have been reported, but more studies are still needed to further build the knowledge on sensor structure design and tuning parameter optimization. The last key issue lies on the enhancement mechanism investigation. Previously, physical theory has comprehensively depicted the surface electromagnetic field property produced by the surface plasmon polaritons on the noble metal, which lays the solid foundation for the EM of the noble metal SERS effect. However, for heavily doped oxide semiconductor, although the carrier concentration can be tuned to 10<sup>21</sup> cm<sup>-3</sup> or even higher, the localized characteristics of these electrons from defects are not considered, thus a further study on the physical model of the surface plasmon polaritons related to the carrier concentration in the oxide semiconductor is needed. In addition, for the noble-metal-based substrates, constructing the "hot spots" is an important approach for further improve the SERS performance, however, this approach is hardly investigated yet. On the other hand, for the CM, it is widely accepted that the charge transfer between the substrate and molecules induces the molecular polarization change, producing enhanced Raman signal. And the defect levels

within the oxides at this procedure significantly facilitate the charge transfer process, however, according to the condensed mater physics, the charge life on different defect level varies, as a consequence, the charge transfer rate will be affected when the oxide is engineered with diverse defect types that have different defect level properties. Finally, although various defect engineering strategies have been reviewed in the manuscript, alternative material engineering methods like ion implantation, laser irradiation, Ar bombardment and building heterojunction are also encouraged to be further investigated in the future.

In summary, this review has covered the recent achievement on the MoO<sub>x</sub> preparing and material property tuning approaches. Then, the SERS mechanism and performance of the various defective MoO<sub>x</sub> substrates are thoroughly surveyed, the SERS enhancement mechanism, performance uniformity, enhancement factor and recyclability of the MoO<sub>x</sub> based SERS substrate are evaluated. In all, MoO<sub>x</sub> is emerging as a promising candidate for SERS application, however more encouraging researches are still desirable to build both better knowledge of MoO<sub>x</sub> materials and understanding on the chemical enhancement model.

### Conflicts of interest

There are no conflicts to declare.

### Acknowledgements

This research was funded by National Natural Science Funding of China (Grant No. 61704095, 61905161), Natural Science Foundation of Zhejiang Province (Grant No. LY19F050002), the Natural Science Funding of Ningbo (Grant No. 2019A610058) and the K.C. Wong Magna Fund in Ningbo University. This project has also received funding from the European Union's Horizon 2020 research and innovation program under the Marie Skłodowska-Curie grant agreement No. 798916.

### Notes and references

1. M. Fleischmann, P. J. Hendra and A. J. McQuillan, *Chem. Phys. Lett.*, 1974, 26, 163-166.
2. M. G. Albrecht and J. A. Creighton, *J. Am. Chem. Soc.*, 1977, 99, 5215-5217.
3. D. L. Jeanmaire and R. P. Van Duyne, *J. Electroanal. Chem. Interf. Electrochem.*, 1977, 84, 1-20.
4. R. Rani, A. Yoshimura, S. Das, M. R. Sahoo, A. Kundu, K. K. Sahu, V. Meunier, S. K. Nayak, N. Koratkar and K. S. Hazra, *ACS Nano*, 2020, 14, 6258-6268.
5. J. Langer, D. Jimenez de Aberasturi, J. Aizpurua, R. A. Alvarez-Puebla, B. Auguie, J. J. Baumberg, G. C. Bazan, S. E. J. Bell, A. Boisen, A. G. Brolo, J. Choo, D. Cialla-May, V. Deckert, L. Fabris, K. Faulds, F. J. Garcia de Abajo, R. Goodacre, D. Graham, A. J. Haes, C. L. Haynes, C. Huck, T.

23. Itoh, M. Käll, J. Kneipp, N. A. Kotov, H. Kuang, E. C. Le Ru, H. K. Lee, J.-F. Li, X. Y. Ling, S. A. Maier, T. Mayerhöfer, M. Moskovits, K. Murakoshi, J.-M. Nam, S. Nie, Y. Ozaki, I. Pastoriza-Santos, J. Perez-Juste, J. Popp, A. Pucci, S. Reich, B. Ren, G. C. Schatz, T. Shegai, S. Schlücker, L.-L. Tay, K. G. Thomas, Z.-Q. Tian, R. P. Van Duyne, T. Vo-Dinh, Y. Wang, K. A. Willets, C. Xu, H. Xu, Y. Xu, Y. S. Yamamoto, B. Zhao and L. M. Liz-Marzán, *ACS Nano*, 2020, 14, 28-117.
24. H. K. Lee, Y. H. Lee, C. S. L. Koh, G. C. Phan-Quang, X. Han, C. L. Lay, H. Y. F. Sim, Y.-C. Kao, Q. An and X. Y. Ling, *Chem. Soc. Rev.*, 2019, 48, 731-756.
25. J. Dong, X. Zhao, E. Cao, Q. Han, L. Liu, W. Zhang, W. Gao, J. Shi, Z. Zheng, D. Han and M. Sun, *Mater. Today Nano*, 2020, 9, 100067.
26. T. Jiang, G. Chen, X. Tian, S. Tang, J. Zhou, Y. Feng and H. Chen, *J. Am. Chem. Soc.*, 2018, 140, 15560-15563.
27. G. Maiorano, L. Rizzello, M. A. Malvindi, S. S. Shankar, L. Martiradonna, A. Falqui, R. Cingolani and P. P. Pompa, *Nanoscale*, 2011, 3, 2227-2232.
28. S. Zhou, J. Li, K. D. Gilroy, J. Tao, C. Zhu, X. Yang, X. Sun and Y. Xia, *ACS Nano*, 2016, 10, 9861-9870.
29. X. Zhang, S. Si, X. Zhang, W. Wu, X. Xiao and C. Jiang, *ACS Appl. Mater. Interfaces*, 2017, 9, 40726-40733.
30. M. Potara, S. Boca, E. Licarete, A. Damert, M.-C. Alupeii, M. T. Chiriac, O. Popescu, U. Schmidt and S. Astilean, *Nanoscale*, 2013, 5, 6013-6022.
31. C. Niu, B. Zou, Y. Wang, L. Cheng, H. Zheng and S. Zhou, *Langmuir*, 2016, 32, 858-863.
32. J. Choi, Y. Luo, R. B. Wehrspohn, R. Hillebrand, J. Schilling and U. Gösele, *J. Appl. Phys.*, 2003, 94, 4757-4762.
33. B. Guha, J. Cardenas and M. Lipson, *Opt. Express*, 2013, 21, 26557-26563.
34. M. Abb, Y. Wang, N. Papasimakis, C. H. de Groot and O. L. Muskens, *Nano Lett.*, 2014, 14, 346-352.
35. F. Zhou, Z. Zhou, J. Chen, T. H. Choy, J. Wang, N. Zhang, Z. Lin, S. Yu, J. Kang, H. S. P. Wong and Y. Chai, *Nat. Nanotechnol.*, 2019, 14, 776-782.
36. A. Otto, *J. Raman Spectrosc.*, 2005, 36, 497-509.
37. H. Ren, S. Sun, J. Cui and X. Li, *Cryst. Growth Des.*, 2018, 18, 6326-6369.
38. X. Wang and L. Guo, *Angew. Chem., Int. Ed.*, 2020, 59, 4231-4239.
39. S. Cong, Y. Yuan, Z. Chen, J. Hou, M. Yang, Y. Su, Y. Zhang, L. Li, Q. Li, F. Geng and Z. Zhao, *Nat. Comm.*, 2015, 6, 7800.
40. X. Jiang, K. Song, X. Li, M. Yang, X. Han, L. Yang and B. Zhao, *ChemistrySelect.*, 2017, 2, 3099-3105.
41. J. Lin, Y. Shang, X. Li, J. Yu, X. Wang and L. Guo, *Adv. Mater.*, 2017, 29, 1604797.
42. T. Yan, L. Zhang, T. Jiang, Z. Bai, X. Yu, P. Dai and M. Wu, *Appl. Surf. Sci.*, 2017, 419, 373-381.
6. W. Lv, C. Gu, S. Zeng, J. Han, T. Jiang and J. Zhou, *Biosens. Bioelectron*, 2018, 8, 2-10.
7. C.-S. Ho, N. Jean, C. A. Hogan, L. Blackmon, S. S. Jeffrey, M. Holodniy, N. Banaei, A. A. E. Saleh, S. Ermon and J. Dionne, *Nat. Comm.*, 2019, 10, 4927.
8. E. Mitsai, A. Kuchmizhak, E. Pustovalov, A. Sergeev, A. Mironenko, S. Bratskaya, D. P. Linklater, A. Balčytis, E. Ivanova and S. Juodkazis, *Nanoscale*, 2018, 10, 9780-9787.
9. J. Yu, Y. Wei, H. Wang, C. Zhang, Y. Wei, M. Wang, B. Man and F. Lei, *Opt. Express*, 2019, 27, 9879-9894.
10. Z. Huang, A. Zhang, Q. Zhang and D. Cui, *J. Mater. Chem. B*, 2019, 7, 3755-3774.
11. D. Zhang, L. Huang, B. Liu, H. Ni, L. Sun, E. Su, H. Chen, Z. Gu and X. Zhao, *Biosens. Bioelectron*, 2018, 106, 204-211.
12. Y. Chen, H. Liu, Y. Tian, Y. Du, Y. Ma, S. Zeng, C. Gu, T. Jiang and J. Zhou, *ACS Appl. Mater. Interfaces*, 2020, 12, 14386-14399.
13. Y. Ma, Y. Du, Y. Chen, C. Gu, T. Jiang, G. Wei and J. Zhou, *Chem. Eng. J.*, 2020, 381, 122710.
14. P. Wang, W. Liu, W. Lin and M. Sun, *J. Raman Spectrosc.*, 2017, 48, 1144-1147.
15. Y. Du, H. Liu, Y. Chen, Y. Tian, X. Zhang, C. Gu, T. Jiang and J. Zhou, *Appl. Surf. Sci.*, 2020, 528, 146953.
16. T. Jiang, X. Wang, J. Zhou, D. Chen and Z. Zhao, *Nanoscale*, 2016, 8, 4908-4914.
17. A. Kundu, R. Rani and K. S. Hazra, *Nanoscale*, 2019, 11, 16245-16252.
18. Q. Chen, Y. Jia, S. Xie and Z. Xie, *Chem. Soc. Rev.*, 2016, 45, 3207-3220.
19. J. Reguera, J. Langer, D. Jiménez de Aberasturi and L. M. Liz-Marzán, *Chem. Soc. Rev.*, 2017, 46, 3866-3885.
20. S. Zhou, M. Zhao, T.-H. Yang and Y. Xia, *Mater. Today*, 2019, 22, 108-131.
21. J.-F. Li, Y.-J. Zhang, S.-Y. Ding, R. Panneerselvam and Z.-Q. Tian, *Chem. Rev.*, 2017, 117, 5002-5069.
22. M. I. Halawa, J. Lai and G. Xu, *Mater. Today Nano*, 2018, 3, 9-27.

## Journal Name

## ARTICLE

43. R. Haldavnekar, K. Venkatakrishnan and B. Tan, *Nat. Comm.*, 2018, 9, 3065.
44. C. Zhou, L. Sun, F. Zhang, C. Gu, S. Zeng, T. Jiang, X. Shen, D. S. Ang and J. Zhou, *ACS Appl. Mater. Interfaces*, 2019, 11, 34091-34099.
45. Y. Yin, P. Miao, Y. Zhang, J. Han, X. Zhang, Y. Gong, L. Gu, C. Xu, T. Yao, P. Xu, Y. Wang, B. Song and S. Jin, *Adv. Funct. Mater.*, 2017, 27, 1606694.
46. L. Zhou, J. Zhou, W. Lai, X. Yang, J. Meng, L. Su, C. Gu, T. Jiang, E. Y. B. Pun, L. Shao, L. Petti, X. W. Sun, Z. Jia, Q. Li, J. Han and P. Mormile, *Nat. Comm.*, 2020, 11, 1785.
47. G. Barbillon, *Nanomaterials*, 2020, 10.
48. I. A. de Castro, R. S. Datta, J. Z. Ou, A. Castellanos-Gomez, S. Sriram, T. Daeneke and K. Kalantar-zadeh, *Adv. Mater.*, 2017, 29, 1701619.
49. H. Cheng, X. Qian, Y. Kuwahara, K. Mori and H. Yamashita, *Adv. Mater.*, 2015, 27, 4616-4621.
50. H. Li, L. McRae, C. J. Firby, M. Al-Hussein and A. Y. Elezzabi, *Nano Energy*, 2018, 47, 130-139.
51. Z. Xu, Q. Zhang and W. Zhai, *RSC Adv.*, 2015, 5, 93554-93562.
52. S. J. Xiao, X. J. Zhao, P. P. Hu, Z. J. Chu, C. Z. Huang and L. Zhang, *ACS Appl. Mater. Interfaces*, 2016, 8, 8184-8191.
53. M. Hossain, S. Rashkeev, V. Madhavan, T. Zhang, C.-Y. Lee, B. Hoex, N. Tabet and A. Abdallah, *Proc. of UPVSEC2018*, 2018, 2018-1A0.1.6, 15-19.
54. S. Balendhran, S. Walia, M. Alsaif, E. P. Nguyen, J. Z. Ou, S. Zhuiykov, S. Sriram, M. Bhaskaran and K. Kalantar-zadeh, *ACS Nano*, 2013, 7, 9753-9760.
55. O. J. Achadu, K. Takemura, I. M. Khoris and E. Y. Park, *Sens Actuators B: Chem*, 2020, 321, 128494.
56. B. Dong, Y. Huang, N. Yu, Y. Fang, B. Cao, Y. Li, H. Xu and M. Sun, *Chem. Asian J.*, 2010, 5, 1824-1829.
57. Y. Chen, C. Lu, L. Xu, Y. Ma, W. Hou and J.-J. Zhu, *CrystEngComm*, 2010, 12, 3740-3747.
58. D. D. Yao, J. Z. Ou, K. Latham, S. Zhuiykov, A. P. O'Mullane and K. Kalantar-zadeh, *Cryst. Growth Des.*, 2012, 12, 1865-1870.
59. Q. Qu, W.-B. Zhang, K. Huang and H.-M. Chen, *Comput. Mater. Sci.*, 2017, 130, 242-248.
60. A. H. Reshak, *RSC Adv.*, 2015, 5, 22044-22052.
61. M. P. Mitoraj and A. Michalak, *J. Struct. Chem.*, 2012, 23, 1369-1375.
62. X. Xiao, C. Zhang, S. Lin, L. Huang, Z. Hu, Y. Cheng, T. Li, W. Qiao, D. Long, Y. Huang, L. Mai, Y. Gogotsi and J. Zhou, *Energy Storage Mater.*, 2015, 1, 1-8.
63. T. Mizushima, Y. Moriya, N. H. H. Phuc, H. Ohkita and N. Kakuta, *Catal. Commun.*, 2011, 13, 10-13.
64. N. A. Chernova, M. Roppolo, A. C. Dillon and M. S. Whittingham, *J. Mater. Chem.*, 2009, 19, 2526-2552.
65. E. M. McCarron and J. C. Calabrese, *J. Solid State Chem.*, 1991, 91, 121-125.
66. C. V. Ramana, I. B. Troitskaia, V. V. Atuchin, M. Ramos and D. Ferrer, *J. Vac. Sci. Technol.*, 2010, 28, 726-729.
67. H. Hu, C. Deng, J. Xu, K. Zhang and M. Sun, *J. Exp. Nanosci.*, 2015, 10, 1336-1346.
68. F. Reale, K. Sharda and C. Mattevi, *Appl. Mater. Today*, 2016, 3, 11-22.
69. C. Muratore, A. A. Voevodin and N. R. Glavin, *Thin Solid Films*, 2019, 688, 137500.
70. Z. Wei and S. Zhuiykov, *Nanoscale*, 2019, 11, 15709-15738.
71. S. Balendhran, S. Walia, H. Nili, J. Z. Ou, S. Zhuiykov, R. B. Kaner, S. Sriram, M. Bhaskaran and K. Kalantar-zadeh, *Adv. Funct. Mater.*, 2013, 23, 3952-3970.
72. P. Dwivedi, S. Dhaneekar and S. Das, *Semicond. Sci. Technol*, 2016, 31, 115010.
73. W.-C. Chang, X. Qi, J.-C. Kuo, S.-c. Lee, S.-K. Ng and D. Chen, *CrystEngComm*, 2011, 13, 5125-5132.
74. N. X. Dongmei Ban, Shaozhi Deng, Jun Chen, Juncong She, *J. Mater. Res. Technol.*, 2010, 26, 584-588.
75. R. Senthilkumar, G. Anandhababu, T. Mahalingam and G. Ravi, *J. Energy Chem.*, 2016, 25, 798-804.
76. K. Kalantar-zadeh, J. Tang, M. Wang, K. L. Wang, A. Shailos, K. Galatsis, R. Kojima, V. Strong, A. Lech, W. Wlodarski and R. B. Kaner, *Nanoscale*, 2010, 2, 429-433.
77. Y. Wang, X. Du, J. Wang, M. Su, X. Wan, H. Meng, W. Xie, J. Xu and P. Liu, *ACS Appl. Mater. Interfaces*, 2017, 9, 5543-5549.
78. D. Wang, J.-N. Li, Y. Zhou, D.-H. Xu, X. Xiong, R.-W. Peng and M. Wang, *Appl. Phys. Lett.*, 2016, 108, 053107
79. M. F. Al-Kuhaili, S. M. A. Durrani and I. A. Bakhtiari, *Appl. Phys. A-Mater*, 2009, 98, 609-615.
80. M. A. Camacho-López, L. Escobar-Alarcón and E. Haro-Poniatowski, *Appl. Phys. A-Mater*, 2004, 78, 59-65.
81. S. Santhosh, M. Mathankumar, S. Selva Chandrasekaran, A. K. Nanda Kumar, P. Murugan and B. Subramanian, *Langmuir*, 2017, 33, 19-33.



- | ARTICLE   | Journal Name  |
|---|---|
| 82. T. Aoki, T. Matsushita, K. Mishiro, A. Suzuki and M. Okuda, <i>Thin Solid Films</i> , 2008, 517, 1482-1486.   | 102. S. Hu and X. Wang, <i>J. Am. Chem. Soc.</i> , 2008, 130, 8126-8127. <small>VIEW ARTICLE ONLINE<br/>DOI: 10.1039/D0NR07779H</small>   |
| 83. O. M. Hussain, K. Srinivasa Rao, K. V. Madhuri, C. V. Ramana, B. S. Naidu, S. Pai, J. John and R. Pinto, <i>Appl. Phys. A-Mater</i> , 2002, 75, 417-422.  | 103. H. Cheng, T. Kamegawa, K. Mori and H. Yamashita, <i>Angew. Chem., Int. Ed.</i> , 2014, 53, 2910-2914.                                |
| 84. C. V. Ramana and C. M. Julien, <i>Chem. Phys. Lett.</i> , 2006, 428, 114-118.   | 104. Y. Xu, M. Zhou, X. Wang, C. Wang, L. Liang, F. Grote, M. Wu, Y. Mi and Y. Lei, <i>Angew. Chem., Int. Ed.</i> , 2015, 54, 8768-8771.  |
| 85. T. Ivanova, K. Gesheva and A. Szekeres, <i>J. Solid State Electrochem.</i> , 2002, 7, 21-24.  | 105. X. Yu, G. Zhang, Z. Lu, J. Liu, X. Lei and X. Sun, <i>CrystEngComm</i> , 2014, 16, 3935-3939.  |
| 86. J. Wang, I. Matsubara, N. Murayama, S. Woosuck and N. Izu, <i>Thin Solid Films</i> , 2006, 514, 329-333.  | 106. Y. Jin and P. K. Shen, <i>J. Mater. Chem. A</i> , 2015, 3, 20080-20085.  |
| 87. K. Gesheva, A. Cziraki, T. Ivanova and A. Szekeres, <i>Thin Solid Films</i> , 2005, 492, 322-326.   | 107. Y. Song, J. Zhao, Y. Zhao, Z. Huang, Y. Li and G. Wu, <i>CrystEngComm</i> , 2016, 18, 6502-6512.                                     |
| 88. T. Ivanova, K. A. Gesheva, G. Popkirov, M. Ganchev and E. Tzvetkova, <i>Mater. Sci. Eng. B</i> , 2005, 119, 232-239.  | 108. Z. Li, J. Ma, B. Zhang, C. Song and D. Wang, <i>CrystEngComm</i> , 2017, 19, 1479-1485.  |
| 89. H. Wu, X. Zhou, J. Li, X. Li, B. Li, W. Fei, J. Zhou, J. Yin and W. Guo, <i>Small</i> , 2018, 14, 1802276.  | 109. K. Sakaushi, J. Thomas, S. Kaskel and J. Eckert, <i>Chem. Mater.</i> , 2013, 25, 2557-2563.  |
| 90. B. B. Wang, X. L. Qu, M. K. Zhu, Y. A. Chen, K. Zheng, X. X. Zhong, U. Cvelbar and K. Ostrikov, <i>J. Alloys Compd</i> , 2018, 765, 1167-1173.  | 110. V. V. Kumar, K. Gayathri and S. P. Anthony, <i>Mater. Res. Bull.</i> , 2016, 76, 147-154.  |
| 91. Y. Chen and B. Wang, <i>Opt. Mater.</i> , 2019, 92, 150-155.  | 111. P. Jittiarporn, L. Sikong, K. Kooptarnond and W. Taweepreda, <i>Ceram. Int.</i> , 2014, 40, 13487-13495.                             |
| 92. M. Koyano, S. Ōhara, H. Negishi, M. Sasaki, M. Inoue, M. Nomura and H. Fujiwara, <i>Phys. Status Solidi B</i> , 1988, 147, 559-565.   | 112. M. Parashar, V. K. Shukla and R. Singh, <i>J. Mater. Sci.: Mater. Electron.</i> , 2020, 31, 3729-3749.                               |
| 93. Y. J. Lee, Y. I. Seo, S.-H. Kim, D.-G. Kim and Y. D. Kim, <i>Appl. Phys. A-Mater</i> , 2009, 97, 237-241.   | 113. J. X. Tang, C. S. Lee and S. T. Lee, <i>J. Appl. Phys.</i> , 2007, 101, 064504.  |
| 94. W. V. Schulmeyer and H. M. Ortner, <i>Int. J. Refract. Met. H.</i> , 2002, 20, 261-269.   | 114. S. Cong, T. Sugahara, T. Wei, J. Jiu, Y. Hirose, S. Nagao and K. Sugauma, <i>Cryst. Growth Des.</i> , 2015, 15, 4536-4542.           |
| 95. A. Borgschulte, O. Sambalova, R. Delmelle, S. Jenatsch, R. Hany and F. Nüesch, <i>Sci. Rep.</i> , 2017, 7, 40761.   | 115. T. Brezesinski, J. Wang, S. H. Tolbert and B. Dunn, <i>Nat. Mater.</i> , 2010, 9, 146-151.   |
| 96. O. de Melo, L. García-Pelayo, Y. González, O. Concepción, M. Manso-Silván, R. López-Nebreda, J. L. Pau, J. C. González, A. Climent-Font and V. Torres-Costa, <i>J. Mater. Chem. C</i> , 2018, 6, 6799-6807. | 116. H. Yin, Y. Kuwahara, K. Mori, H. Cheng, M. Wen and H. Yamashita, <i>J. Mater. Chem. A</i> , 2017, 5, 8946-8953.                      |
| 97. A. Chithambararaj, N. Rajeswari Yogamalar and A. C. Bose, <i>Cryst. Growth Des.</i> , 2016, 16, 1984-1995.  | 117. S. Koçak, F. N. Ertaş and Z. Dursun, <i>Appl. Surf. Sci.</i> , 2013, 265, 205-213.   |
| 98. D. Ding, W. Guo, C. Guo, J. Sun, N. Zheng, F. Wang, M. Yan and S. Liu, <i>Nanoscale</i> , 2017, 9, 2020-2029.   | 118. A. Quintana, A. Varea, M. Guerrero, S. Suriñach, M. D. Baró, J. Sort and E. Pellicer, <i>Electrochim. Acta</i> , 2015, 173, 705-714. |
| 99. J. S. Chen, Y. L. Cheah, S. Madhavi and X. W. Lou, <i>J. Phys. Chem. C</i> , 2010, 114, 8675-8678.  | 119. D. Di Yao, M. R. Field, A. P. O'Mullane, K. Kalantar-Zadeh and J. Z. Ou, <i>Nanoscale</i> , 2013, 5, 10353-10359.                    |
| 100. L. Fang, Y. Shu, A. Wang and T. Zhang, <i>J. Phys. Chem. C</i> , 2007, 111, 2401-2408.   | 120. G. Zhao, L. Zhang and K. Sun, <i>J. Electroanal. Chem.</i> , 2013, 694, 61-67.   |
| 101. R. Liang, H. Cao and D. Qian, <i>Chem. Commun.</i> , 2011, 47, 10305-10307.  | 121. E. Gómez, E. Pellicer and E. Vallés, <i>J. Electroanal. Chem.</i> , 2005, 580, 238-244.  |
|   | 122. D. Sinkeviciute, J. Baltrusaitis and N. Dukstiene, <i>J. Solid State Electrochem.</i> , 2010, 15, 711-723.                           |

- | Journal Name  | ARTICLE   |
|---|---|
| 123. R. S. Patil, M. D. Uplane and P. S. Patil, <i>Appl. Surf. Sci.</i> , 2006, 252, 8050-8056.   | H. Nili, E. P. Nguyen, K. Latham, J. van Embden, M. S. Strano, J. Z. Ou and K. Kalantar-zadeh, <i>Adv. Funct. Mater.</i> , 2016, 26, 91-100.  |
| 124. S. N. Lou, N. Yap, J. Scott, R. Amal and Y. H. Ng, <i>Sci. Rep.</i> , 2014, 4, 7428.   | 143. D. S. Lambert, A. Lennon and P. A. Burr, <i>J. Mater. Chem. C</i> , 2018, 122, 27241-27249.  |
| 125. M. Szkoda, K. Trzciński, K. Siuzdak and A. Lisowska-Oleksiak, <i>Electrochim. Acta</i> , 2017, 228, 139-145.   | 144. R. He, Z. Chen, H. Lai, T. Zhang, J. Wen, H. Chen, F. Xie, S. Yue, P. Liu, J. Chen, W. Xie, X. Wang and J. Xu, <i>ACS Appl. Mater. Interfaces</i> , 2019, 11, 15741-15747.         |
| 126. K. Inzani, M. Nematollahi, F. Vullum-Bruer, T. Grande, T. W. Reenaas and S. M. Selbach, <i>Phys. Chem. Chem. Phys.</i> , 2017, 19, 9232-9245.  | 145. S. S. Mahajan, S. H. Mujawar, P. S. Shinde, A. I. Inamdar and P. S. Patil, <i>Sol. Energy Mater. Sol. Cells</i> , 2009, 93, 183-187.   |
| 127. H. Peelaers, M. L. Chabinyk and C. G. Van de Walle, <i>Chem. Mater.</i> , 2017, 29, 2563-2567.   | 146. N. Usha, R. Sivakumar and C. Sanjeeviraja, <i>Mater. Lett.</i> , 2018, 229, 189-192.   |
| 128. F. Li and Z. Chen, <i>Nanoscale</i> , 2013, 5, 5321-5333.  | 147. H. Li, J. Chen, M. Cui, G. Cai, A. L.-S. Eh, P. S. Lee, H. Wang, Q. Zhang and Y. Li, <i>J. Mater. Chem. C</i> , 2016, 4, 33-38.  |
| 129. H.-S. Kim, J. B. Cook, H. Lin, Jesse S. Ko, Sarah H. Tolbert, V. Ozolins and B. Dunn, <i>Nat. Mater.</i> , 2017, 16, 454-460.  | 148. C. M. Cholang, T. M. Westphal, R. D. C. Balboni, E. A. Moura, A. Gündel, W. H. Flores, A. Pawlicka and C. O. Avellaneda, <i>J. Solid State Electrochem.</i> , 2017, 21, 1509-1515. |
| 130. M. Vasilopoulou, A. M. Douvas, D. G. Georgiadou, L. C. Palilis, S. Kennou, L. Sygellou, A. Soultati, I. Kostis, G. Papadimitropoulos, D. Davazoglou and P. Argitis, <i>J. Am. Chem. Soc.</i> , 2012, 134, 16178-16187. | 149. C. C. Chang, P. W. Chi, P. Chandan and C. K. Lin, <i>Materials (Basel)</i> , 2019, 12, 2475.   |
| 131. M. T. Greiner, L. Chai, M. G. Helander, W.-M. Tang and Z.-H. Lu, <i>Adv. Funct. Mater.</i> , 2012, 22, 4557-4568.  | 150. Q.-Y. Ouyang, L. Li, Q.-S. Wang, Y. Zhang, T.-S. Wang, F.-N. Meng, Y.-J. Chen and P. Gao, <i>Sens Actuators B: Chem</i> , 2012, 169, 17-25.  |
| 132. G. Song, J. Shen, F. Jiang, R. Hu, W. Li, L. An, R. Zou, Z. Chen, Z. Qin and J. Hu, <i>ACS Appl. Mater. Interfaces</i> , 2014, 6, 3915-3922.   | 151. S. Bai, C. Chen, D. Zhang, R. Luo, D. Li, A. Chen and C.-C. Liu, <i>Sens Actuators B: Chem</i> , 2014, 204, 754-762.   |
| 133. J. Wang, Y. Yang, H. Li, J. Gao, P. He, L. Bian, F. Dong and Y. He, <i>Chem. Sci.</i> , 2019, 10, 6330-6335.   | 152. Z. Liu, Y. Jin, F. Teng, X. Hua and M. Chen, <i>Catal. Commun.</i> , 2015, 66, 42-45.  |
| 134. Y. Li, J. Cheng, Y. Liu, P. Liu, W. Cao, T. He, R. Chen and Z. Tang, <i>J. Mater. Chem. C</i> , 2017, 121, 5208-5214.  | 153. A. Phuruangrat, U. Cheed-Im, T. Thongtem and S. Thongtem, <i>Mater. Lett.</i> , 2016, 172, 166-170.  |
| 135. R. Li, H. An, W. Huang and Y. He, <i>Sens Actuators B: Chem</i> , 2018, 259, 59-63.  | 154. H.-Y. Chen, H.-C. Su, C.-H. Chen, K.-L. Liu, C.-M. Tsai, S.-J. Yen and T.-R. Yew, <i>J. Mater. Chem.</i> , 2011, 21, 5745-5752.  |
| 136. W. Zhang, H. Li, C. J. Firby, M. Al-Hussein and A. Y. Elezzabi, <i>ACS Appl. Mater. Interfaces</i> , 2019, 11, 20378-20385.  | 155. M. Balaji, J. Chandrasekaran, M. Raja and S. Rajesh, <i>J. Mater. Sci.: Mater. Electron.</i> , 2016, 27, 11646-11658.  |
| 137. K. Khojier, H. Savaloni and S. Zolghadr, <i>Appl. Surf. Sci.</i> , 2014, 320, 315-321.   | 156. X. Sha, L. Chen, A. C. Cooper, G. P. Pez and H. Cheng, <i>J. Mater. Chem. C</i> , 2009, 113, 11399-11407.  |
| 138. S. Kasani, P. Zheng, J. Bright and N. Wu, <i>ACS Appl. Mater. Interfaces</i> , 2019, 1, 2389-2395.   | 157. H. Cheng, M. Wen, X. Ma, Y. Kuwahara, K. Mori, Y. Dai, B. Huang and H. Yamashita, <i>J. Am. Chem. Soc.</i> , 2016, 138, 9316-9324.   |
| 139. L. Li, T. Zhang, J. Yan, X. Cai and S. F. Liu, <i>Small</i> , 2017, 13, 1700441.   | 158. I. Kostis, N. Vourdas, G. Papadimitropoulos, A. Douvas, M. Vasilopoulou, N. Boukos and D. Davazoglou, <i>J. Phys. Chem. C</i> , 2013, 117, 18013-18020.                            |
| 140. B. Y. Zhang, A. Zavabeti, A. F. Chrimes, F. Haque, L. A. O'Dell, H. Khan, N. Syed, R. Datta, Y. Wang, A. S. R. Chesman, T. Daeneke, K. Kalantar-zadeh and J. Z. Ou, <i>Adv. Funct. Mater.</i> , 2018, 28, 1706006.     | 159. F. Xie, W. C. H. Choy, C. Wang, X. Li, S. Zhang and J. Hou, <i>Adv. Mater.</i> , 2013, 25, 2051-2055.  |
| 141. A. S. Etman, L. Wang, K. Edström, L. Nyholm and J. Sun, <i>Adv. Funct. Mater.</i> , 2019, 29, 1806699.   | 160. M. M. Y. A. Alsaif, K. Latham, M. R. Field, D. D. Yao, N. V.   |
| 142. M. M. Y. A. Alsaif, A. F. Chrimes, T. Daeneke, S. Balendhran, D. O. Bellisario, Y. Son, M. R. Field, W. Zhang,   |   |

## ARTICLE

## Journal Name

- Medehkar, G. A. Beane, R. B. Kaner, S. P. Russo, J. Z. Ou and K. Kalantar-zadeh, *Adv. Mater.*, 2014, 26, 3931-3937.
161. Q. Zhu, S. Jiang, K. Ye, W. Hu, J. Zhang, X. Niu, Y. Lin, S. Chen, L. Song, Q. Zhang, J. Jiang and Y. Luo, *Adv. Mater.*, 2020, 32, 2004059.
162. Y. Zhan, Y. Liu, H. Zu, Y. Guo, S. Wu, H. Yang, Z. Liu, B. Lei, J. Zhuang, X. Zhang, D. Huang and C. Hu, *Nanoscale*, 2018, 10, 5997-6004.
163. F. Haque, A. Zavabeti, B. Y. Zhang, R. S. Datta, Y. Yin, Z. Yi, Y. Wang, N. Mahmood, N. Pillai, N. Syed, H. Khan, A. Jannat, N. Wang, N. Medhekar, K. Kalantar-zadeh and J. Z. Ou, *J. Mater. Chem. A*, 2019, 7, 257-268.
164. H. Li, Q. Xu, X. Wang and W. Liu, *Small*, 2018, 14, 1801523.
165. P. Li, L. Zhu, C. Ma, L. Zhang, L. Guo, Y. Liu, H. Ma and B. Zhao, *ACS Appl. Mater. Interfaces*, 2020, 12, 19153-19160.
166. Z. Zheng, S. Cong, W. Gong, J. Xuan, G. Li, W. Lu, F. Geng and Z. Zhao, *Nat. Comm.*, 2017, 8, 1-10.
167. X. Zhou, X. Zhao, F. Xie, Z. Jin, X. Song, W. Xie, X. Wang and Z. Tang, *ACS Appl. Mater. Interfaces*, 2020, 3, 5656-5664.
168. J. Chen, K. Sun, Y. Zhang, D. Wu, Z. Jin, F. Xie, X. Zhao and X. Wang, *Anal. Bioanal. Chem.*, 2019, 411, 2781-2791.
169. O. J. Achadu, F. Abe, T. Suzuki and E. Y. Park, *ACS Appl. Mater. Interfaces*, 2020, 12, 43522-43534.
170. Y. Guo, Z. Zhuang, Z. Liu, W. Fan, H. Zhong, W. Zhang, Y. Ni and Z. Guo, *Appl. Surf. Sci.*, 2019, 480, 1162-1170.
171. Y. Xu, K. Lai, C. Gu, T. Jiang, X. Shen, S. Zeng, A. H.-P. Ho, D. S. Ang and J. Zhou, *physica status solidi-Rapid Res Lett*, 2020, n/a, 2000499.
172. L. Su, Y. Xiong, Z. Chen, Z. Duan, Y. Luo, D. Zhu and X. Ma, *Sens Actuators B: Chem*, 2019, 279, 320-326.
173. G. C. Schatz, M. A. Young and R. P. Duyne, in *Surface-Enhanced Raman Scattering-Physics and Applications*, eds. K. Kneipp, M. Moskovits and J. Kneipp, Springer, Berlin, 2006, vol. 103.
174. J. Ma, X. Tan, Y. Ma, X. Yao, J. Zhang and L. Wang, *Chem. Eur. J*, 2020, 26, 2653-2657.
175. Q. Zhang, X. Li, Q. Ma, Q. Zhang, H. Bai, W. Yi, J. Liu, J. Han and G. Xi, *Nat. Comm.*, 2017, 8, 14903.
176. X. Tan, L. Wang, C. Cheng, X. Yan, B. Shen and J. Zhang, *Chem. Commun.*, 2016, 52, 2893-2896.

View Article Online  
DOI: 10.1039/D0NR07779H

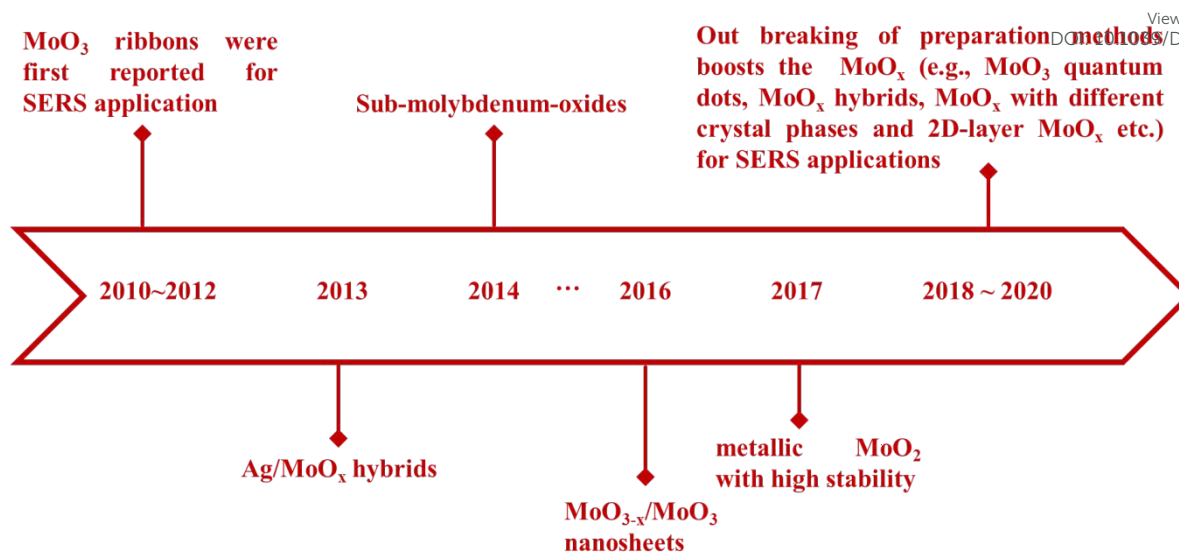


**Fig. 1.** A concise timeline depicts the emergence of MoO<sub>x</sub> nanostructures for SERS application.

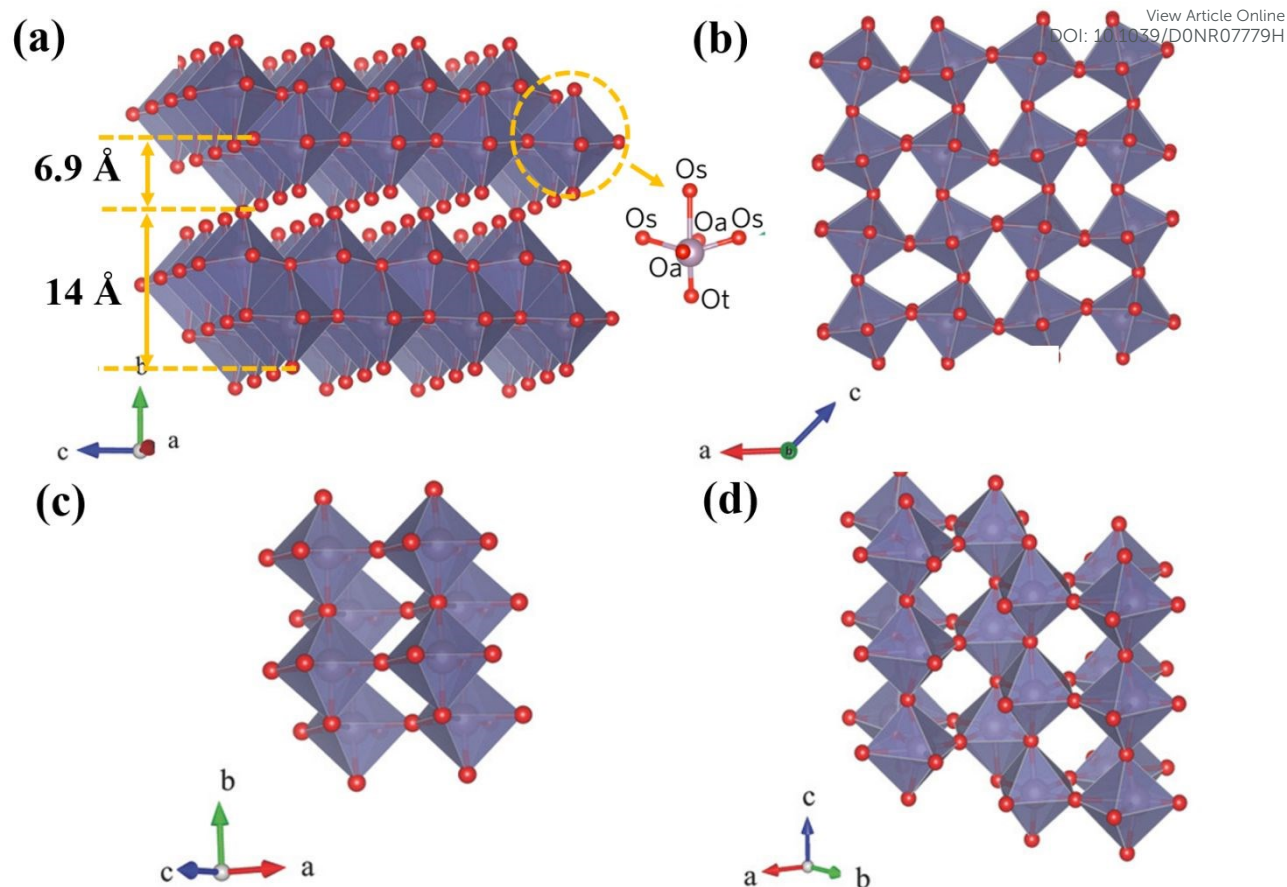


**Fig. 2.** (a) The  $\alpha$ - $\text{MoO}_3$  with an orthorhombic crystal structure. (b) The  $\beta$ - $\text{MoO}_3$  with a monoclinic crystal structure. (c) The  $\epsilon$ - $\text{MoO}_3$  with a monoclinic crystal structure. (d) The  $h$ - $\text{MoO}_3$  with a hexagonal crystal structure.<sup>[48]</sup> Reproduced with permission. Copyright 2017, Wiley-VCH. The inset in (a) shows the respective position of  $\text{O}_a$ ,  $\text{O}_s$  and  $\text{O}_t$  in the  $\text{MoO}_6$  octahedra.

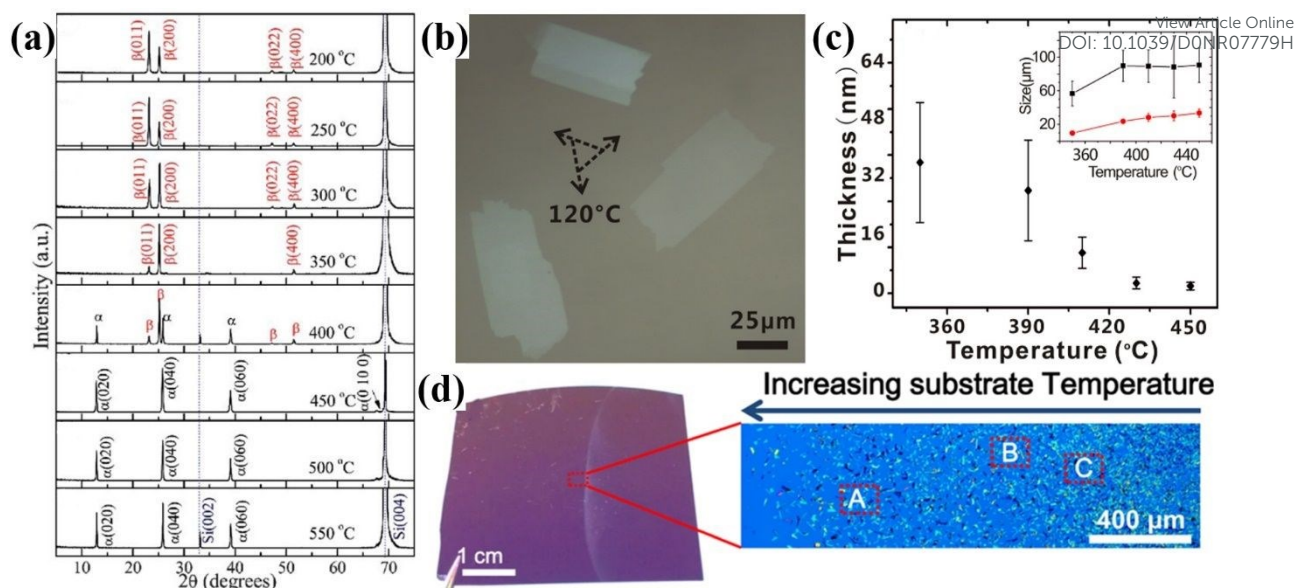


**Fig. 3.** (a) XRD patterns of the  $\text{MoO}_3$  films sputtered at room temperature in 3 mTorr mixed gas and then annealed at different temperature in air for 1 h.<sup>[73]</sup> Reproduced with permission. Copyright 2011, Royal Society of Chemistry. (b) Optical micrograph of grown  $\alpha$ - $\text{MoO}_3$  sheets on mica substrate. (c) Thickness and lateral size of  $\alpha$ - $\text{MoO}_3$  sheets as a function of the growth temperature.<sup>[78]</sup> Reproduced with permission. Copyright 2016, American Institute of Physics. (d) Optical image of the sample and the distribution of as-grown  $\text{MoO}_3$ .<sup>[77]</sup> Reproduced with permission. Copyright 2017, The American Chemical Society.

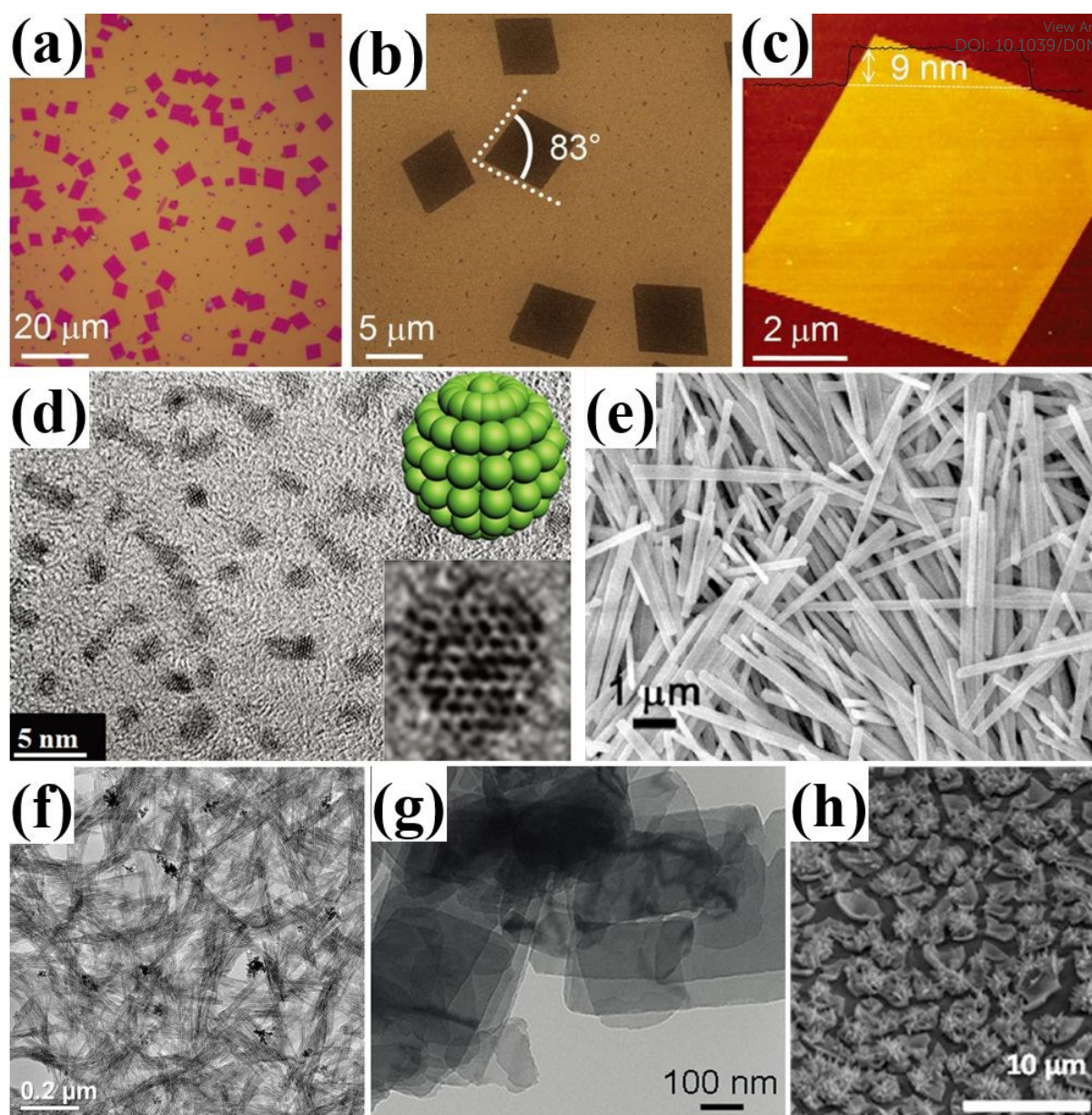


**Fig. 4.** (a) Optical image. (b) SEM image and (c) AFM image of MoO<sub>2</sub> nanosheets prepared by CVD.<sup>[89]</sup> Reproduced with permission. Copyright 2018, Wiley-VCH. (d) TEM image of MoO<sub>3-x</sub> quantum dots.<sup>[98]</sup> Reproduced with permission. Copyright 2017, Royal Society of Chemistry. (e) SEM image of α-MoO<sub>3</sub> nanorod.<sup>[99]</sup> Reproduced with permission. Copyright 2010, The American Chemical Society. (f) TEM image of single walled MoO<sub>3</sub> nanotubes.<sup>[102]</sup> Reproduced with permission. Copyright 2008, The American Chemical Society. (g) TEM image of the MoO<sub>3-x</sub> nanosheets.<sup>[103]</sup> Reproduced with permission. Copyright 2014, Wiley-VCH. (h) SEM image of nanoflower like MoO<sub>2</sub>.<sup>[106]</sup> Reproduced with permission. Copyright 2015, Royal Society of Chemistry.

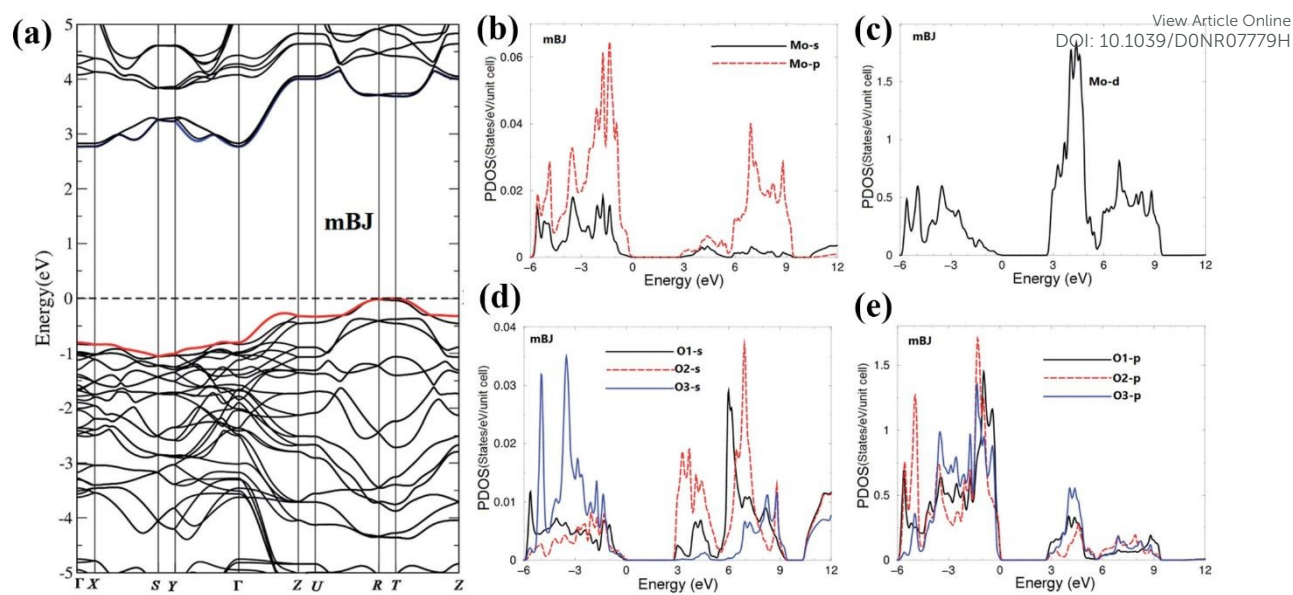


**Fig. 5.** (a) Band diagram calculated with the mBJ-GGA method.<sup>[60]</sup> Copyright 2015, Royal Society of Chemistry. (b) The projected DOS for the  $-s$ ,  $-p$  electron of Mo. (c) the projected DOS for the  $-d$  electron of Mo. (d) The projected DOS for the  $-s$  electron of O. (e) The projected DOS for the  $-p$  electron of O. Here, O1 equal to O<sub>x</sub>, O2 equal to O<sub>y</sub> and O3 equal to O<sub>z</sub>.<sup>[126]</sup> Reproduced with permission. Copyright 2017, Royal Society of Chemistry.



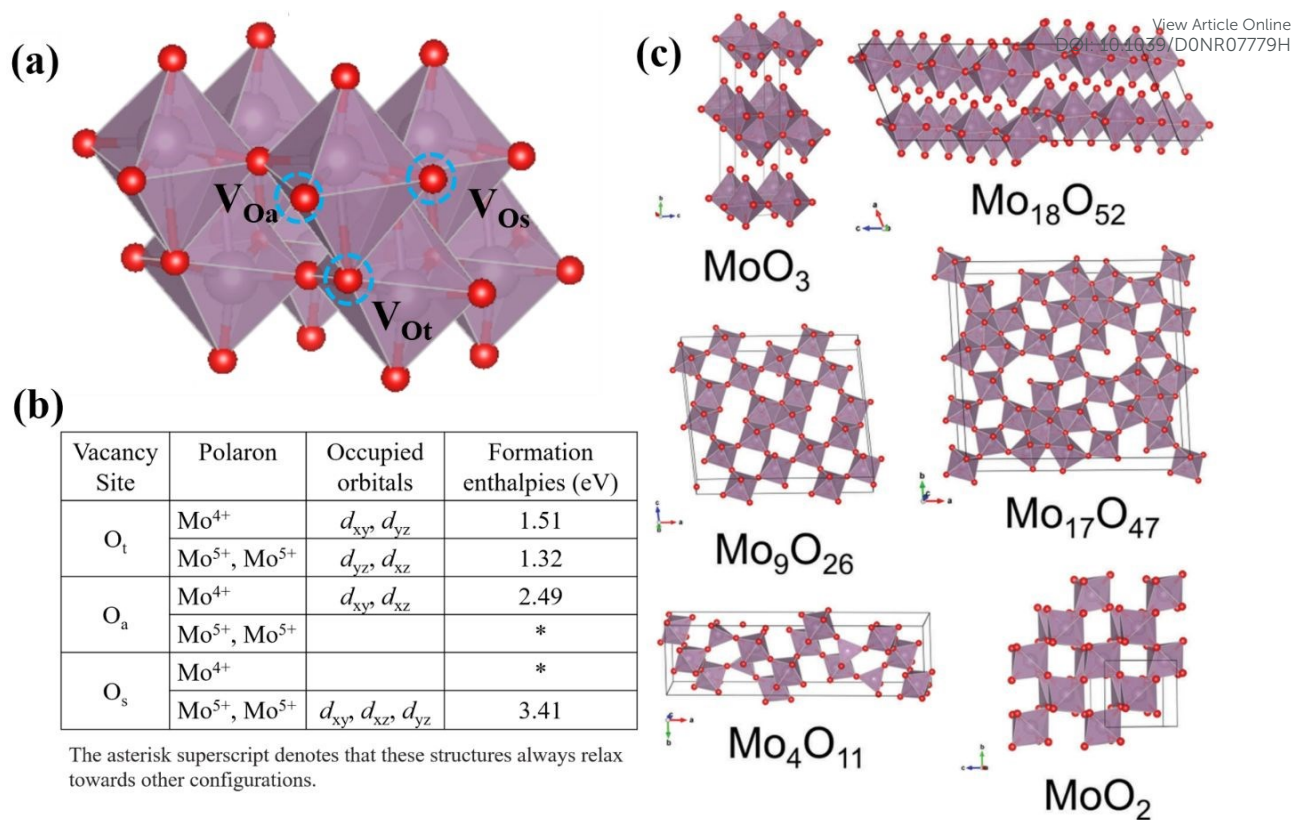


**Fig. 6.** (a) The possible position of forming different oxygen vacancy types in the  $\alpha$ -MoO<sub>3</sub>. (b) The listed formation enthalpies for the different oxygen vacancy types and polaron states in the bulk  $\alpha$ -MoO<sub>3</sub>. Adapted from Ref. [129]. Copyright 2017, The Springer Nature Publishing Group (c)  $\alpha$ -MoO<sub>3</sub> crystal structure and various defective structures with different vacancy concentrations.<sup>[126]</sup> Reproduced with permission. Copyright 2017, Royal Society of Chemistry.

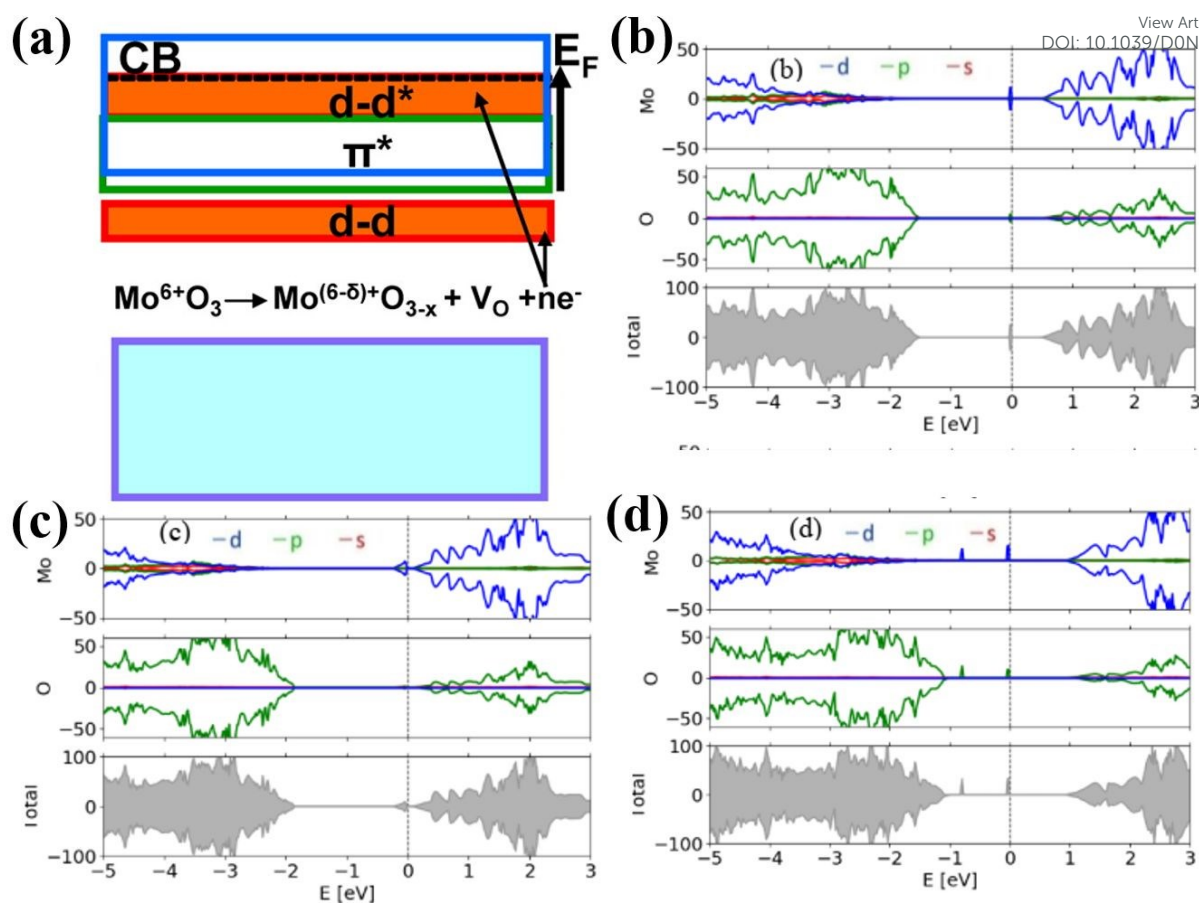


**Fig. 7.** (a) A schematic illustration of the electron transferring and defect level formation with the introducing of oxygen vacancy in the MoO<sub>3</sub>.<sup>[130]</sup> Reproduced with permission. Copyright 2012, The American Chemical Society. (b) Projected DOS of the atomic supercell with V<sub>Os</sub> vacancy. (c) Projected DOS of the atomic supercell with V<sub>Oa</sub> vacancy. (d) Projected DOS of the atomic supercell with V<sub>Ot</sub> vacancy. The blue, green and red lines represent the *d*, *p* and *s* orbital contributions of the corresponding atoms.<sup>[53]</sup> Reproduced with permission. Copyright 2018, EU PVSEC.

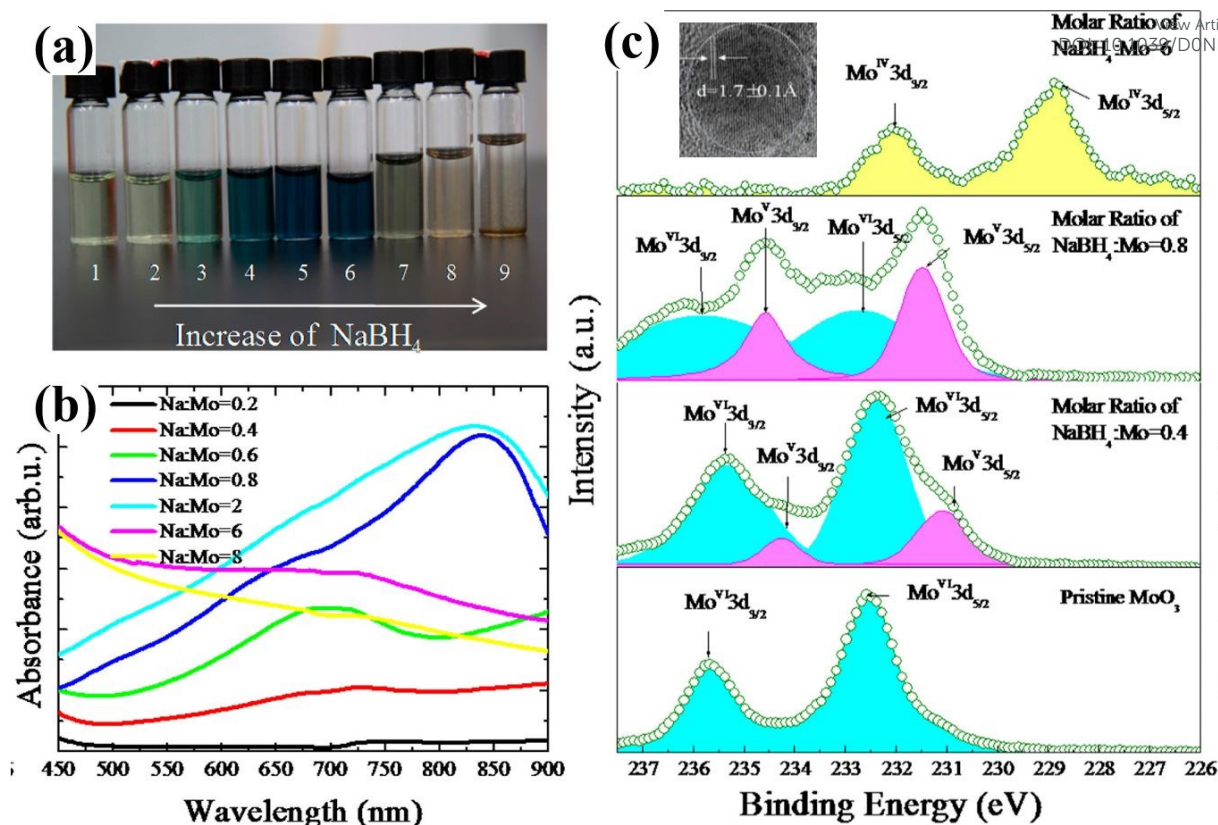


**Fig. 8.** (a) The color evolution of the MoO<sub>3-x</sub> nanodot aqueous solution with the increase of NaBH<sub>4</sub>: Mo mole ratio. (b) UV-vis absorption spectra of MoO<sub>3-x</sub> nanodots prepared with different NaBH<sub>4</sub> concentrations. (c) XPS spectra of Mo 3d obtained on MoO<sub>3</sub> and various MoO<sub>3-x</sub> nanodots prepared with different concentrations.<sup>[134]</sup> Reproduced with permission. Copyright 2017, The American Chemical Society.

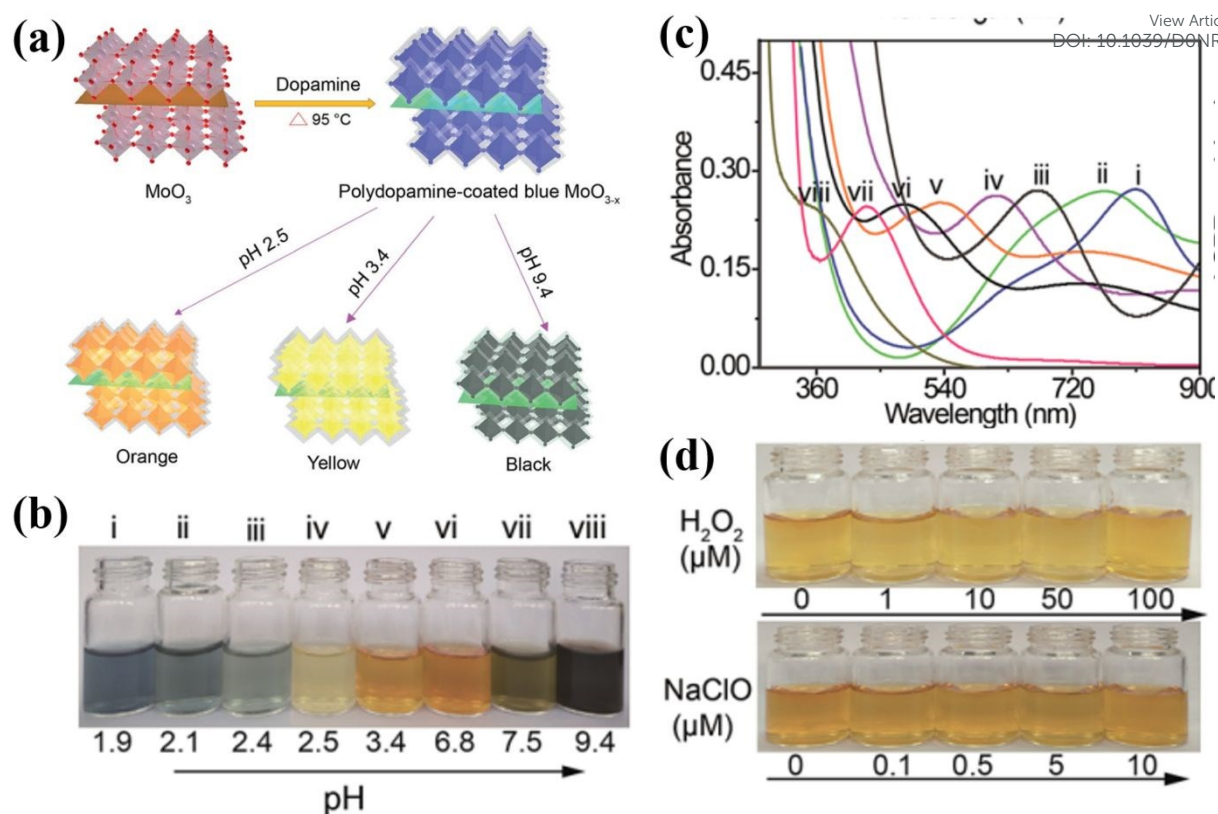


**Fig. 9.** (a) Schematic illustration of the preparation of PDA-coated  $\text{MoO}_{3-x}$  nanosheets with tunable plasmon resonance. (b) Photography of the PDA-coated  $\text{MoO}_{3-x}$  nanosheets obtained under different pH values. (c) UV-Vis-NIR spectra of the  $\text{MoO}_{3-x}$  nanosheets prepared under various pH reaction solution. (d) photography of a yellow  $\text{MoO}_{3-x}$  nanosheets dispersed in the  $\text{H}_2\text{O}_2$  and  $\text{NaClO}$  with different concentrations.<sup>[133]</sup> Reproduced with permission. Copyright 2019, Royal Society of Chemistry.

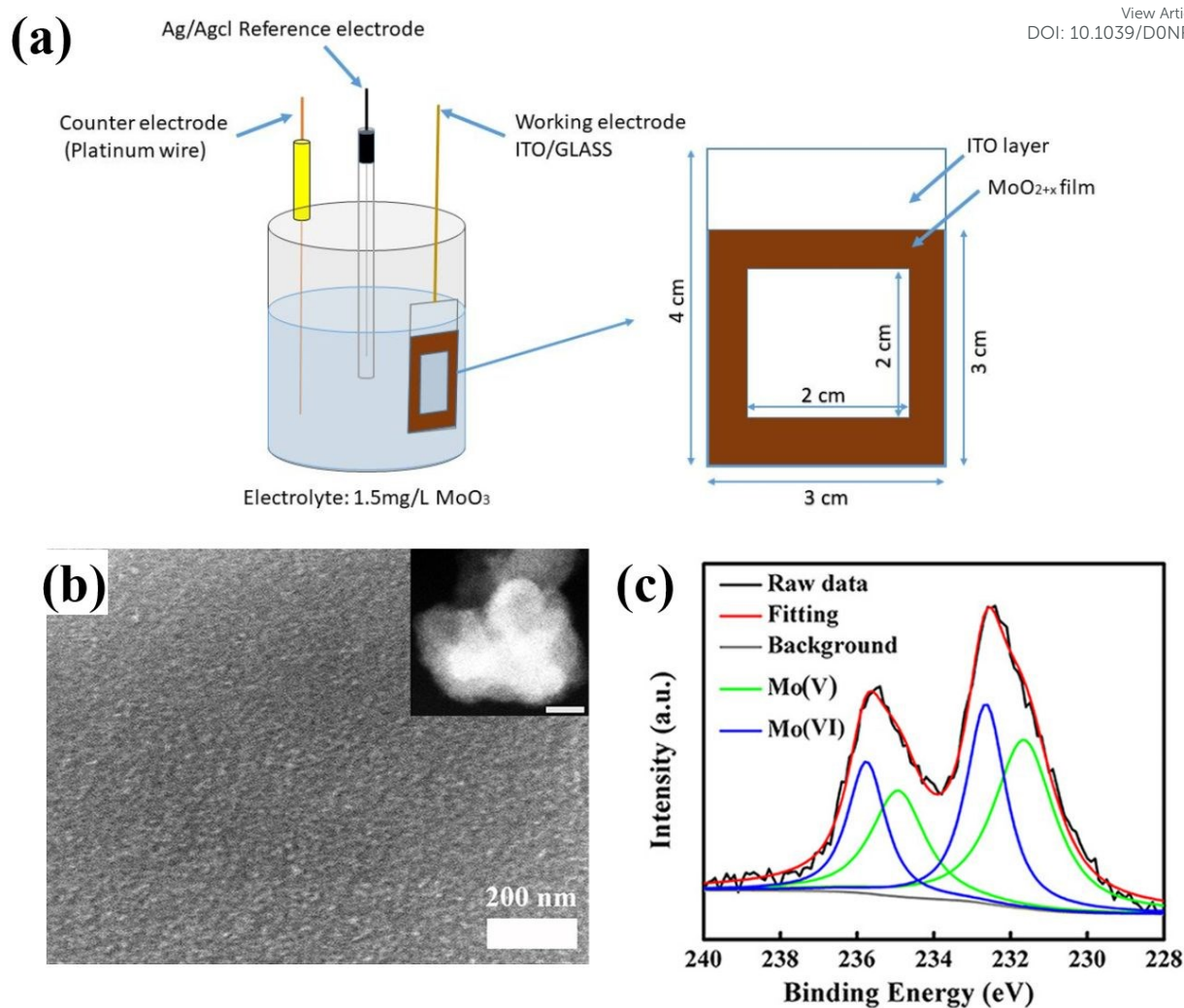


**Fig. 10.** (a) Schematic of  $\text{MoO}_{2+x}$  films electrodeposited on ITO glass. (b) FSEM images of prepared  $\text{MoO}_{2+x}$  nanofilm. (c) XPS spectra of Mo 3d obtained on  $\text{MoO}_{2+x}$ .<sup>[136]</sup> Reproduced with permission. Copyright 2019, The American Chemical Society.

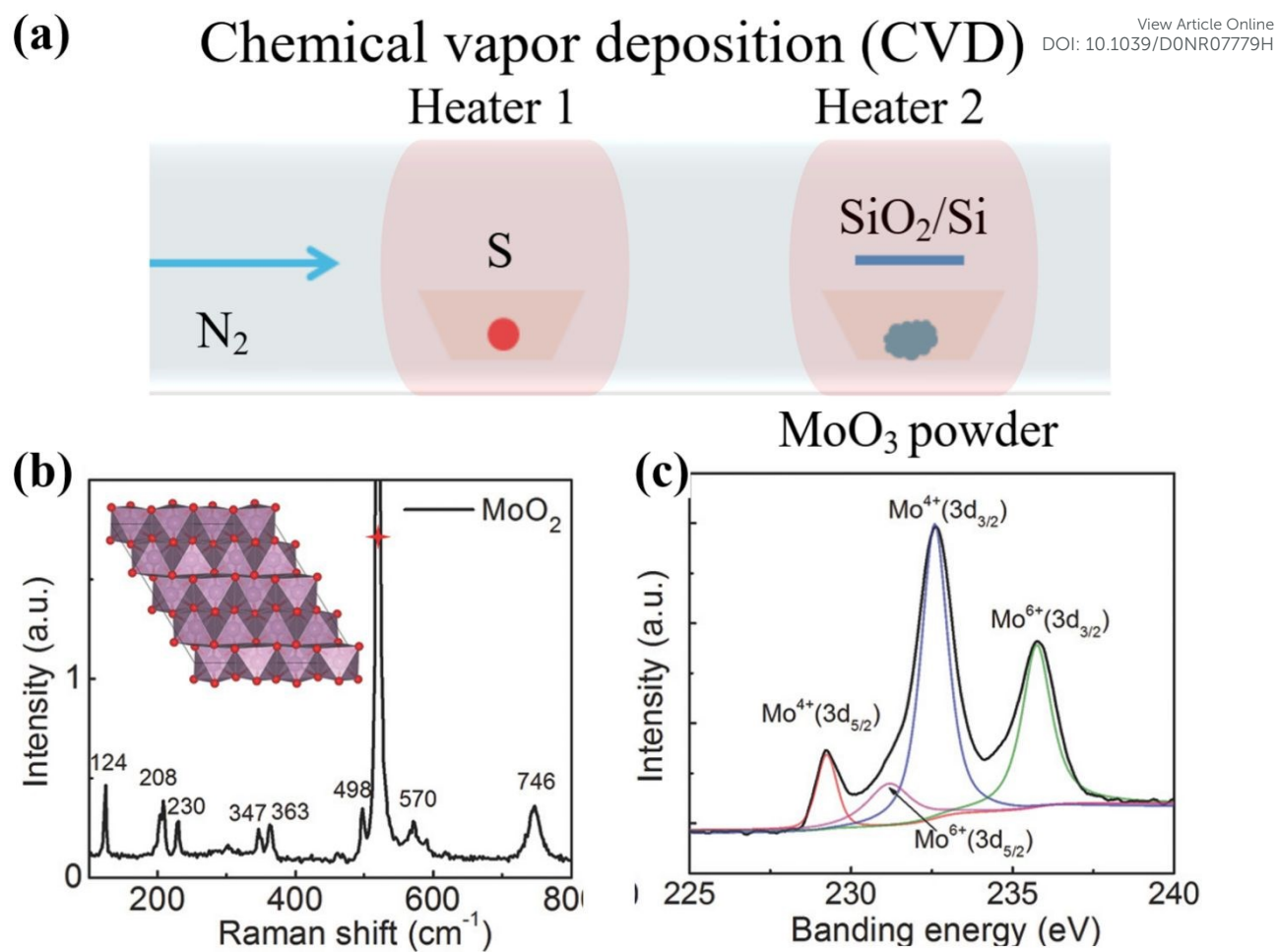


**Fig. 11.** (a) Schematic diagram of CVD system. (b) Raman spectrum of MoO<sub>2</sub> nanosheets. (c) XPS spectrum of the Mo 3d spectrum obtained on the sample, indicating that the Mo ion in the material is mainly +4.<sup>[89]</sup> Reproduced with permission.

Copyright 2018, Wiley-VCH.

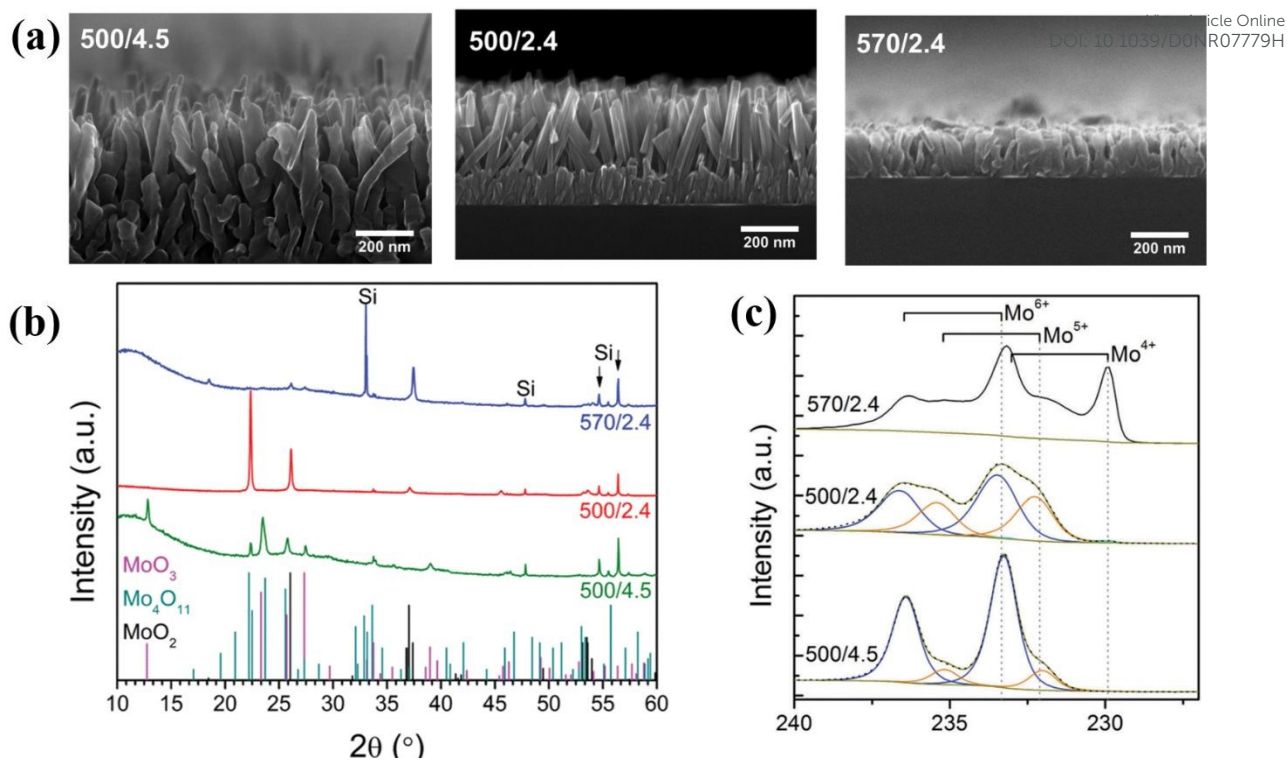


**Fig. 12.** (a) Molybdenum oxide deposited under different chamber condition. (b) XRD spectra of the deposited film. (c) XPS spectra of the sample prepared under three different conditions.<sup>[126]</sup> Reproduced with permission. Copyright 2017, Royal Society of Chemistry.

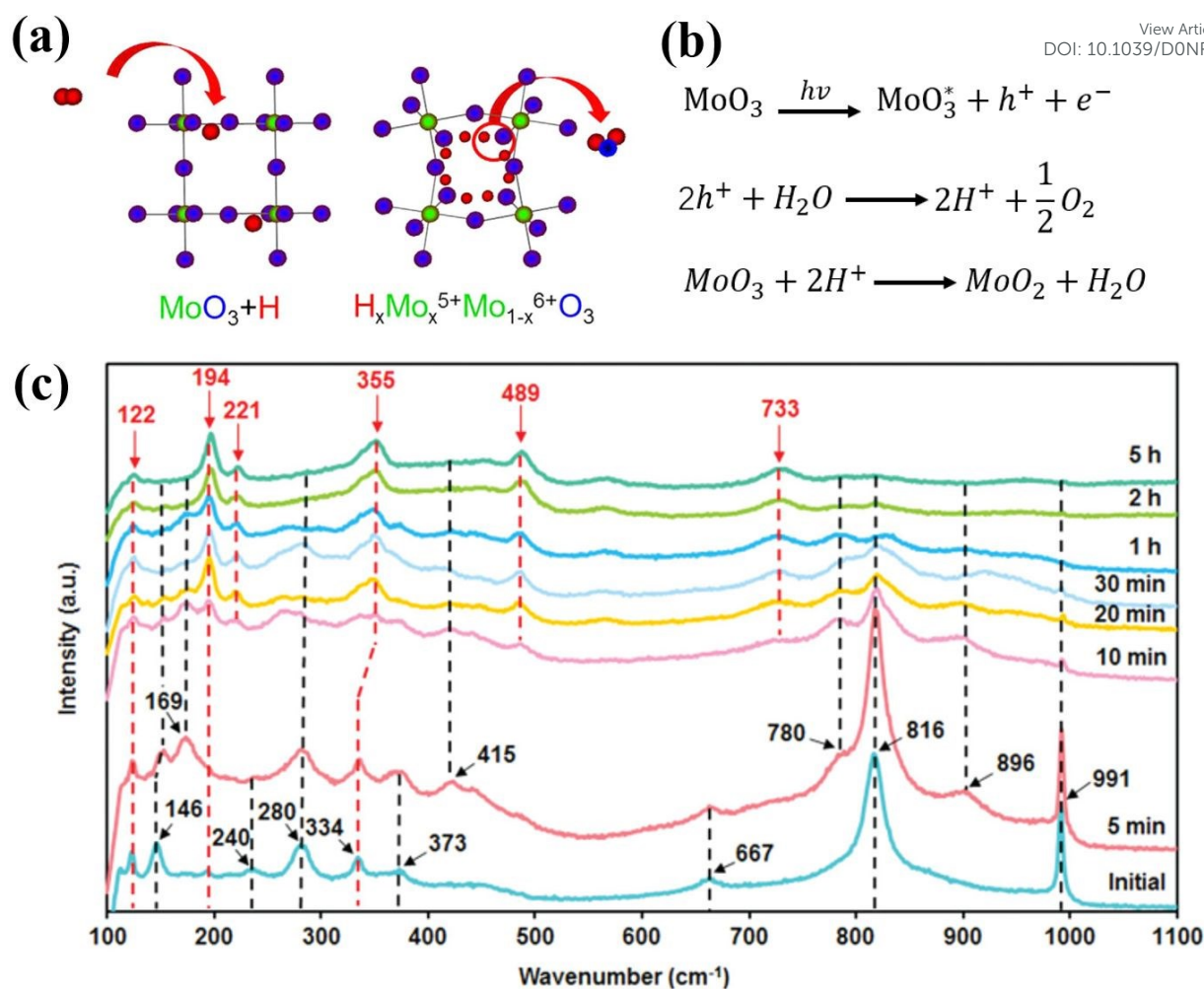


**Fig. 13.** (a) Schematic illustration of the H intercalation in the  $\text{MoO}_3$ , and then the  $\text{H}_2\text{O}$  molecule dissociating from the crystal in the  $\text{MoO}_3$ .<sup>[95]</sup> Reproduced with permission. Copyright 2017, The Springer Nature Publishing Group. (b) The photocatalytic process of the  $\text{MoO}_3$  solution under the light irradiation. Adapted from Ref. [160]. (c) The evolution of the 2D  $\text{MoO}_{3-x}$  nano flake when exposed to the simulated solar light for different time.<sup>[160]</sup> Reproduced with permission. Copyright 2014, Wiley-VCH.



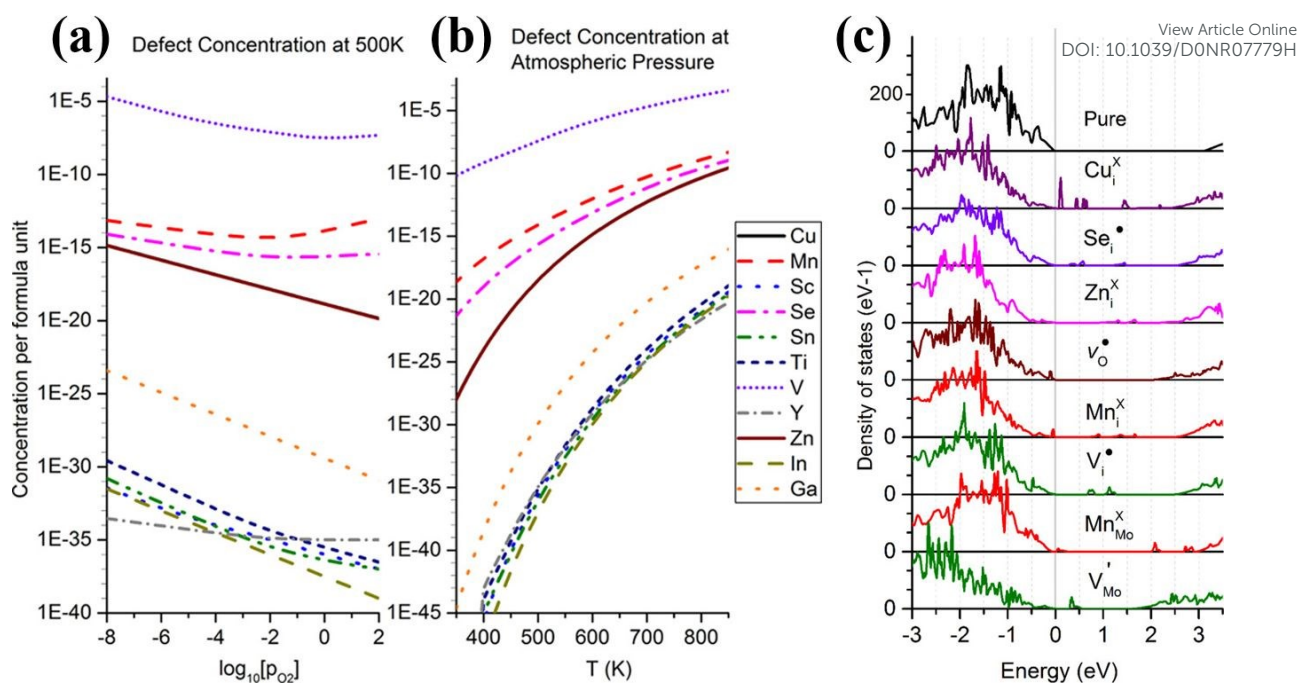


**Fig. 14.** (a) The equilibrium solubility curve for the elements at the temperature of 500 K with varied  $O_2$  partial pressure. (b) Atmospheric pressure with varied temperature. (c) The electronic density of states introduced by varied dopants.<sup>[143]</sup>

Reproduced with permission. Copyright 2018, The American Chemical Society.

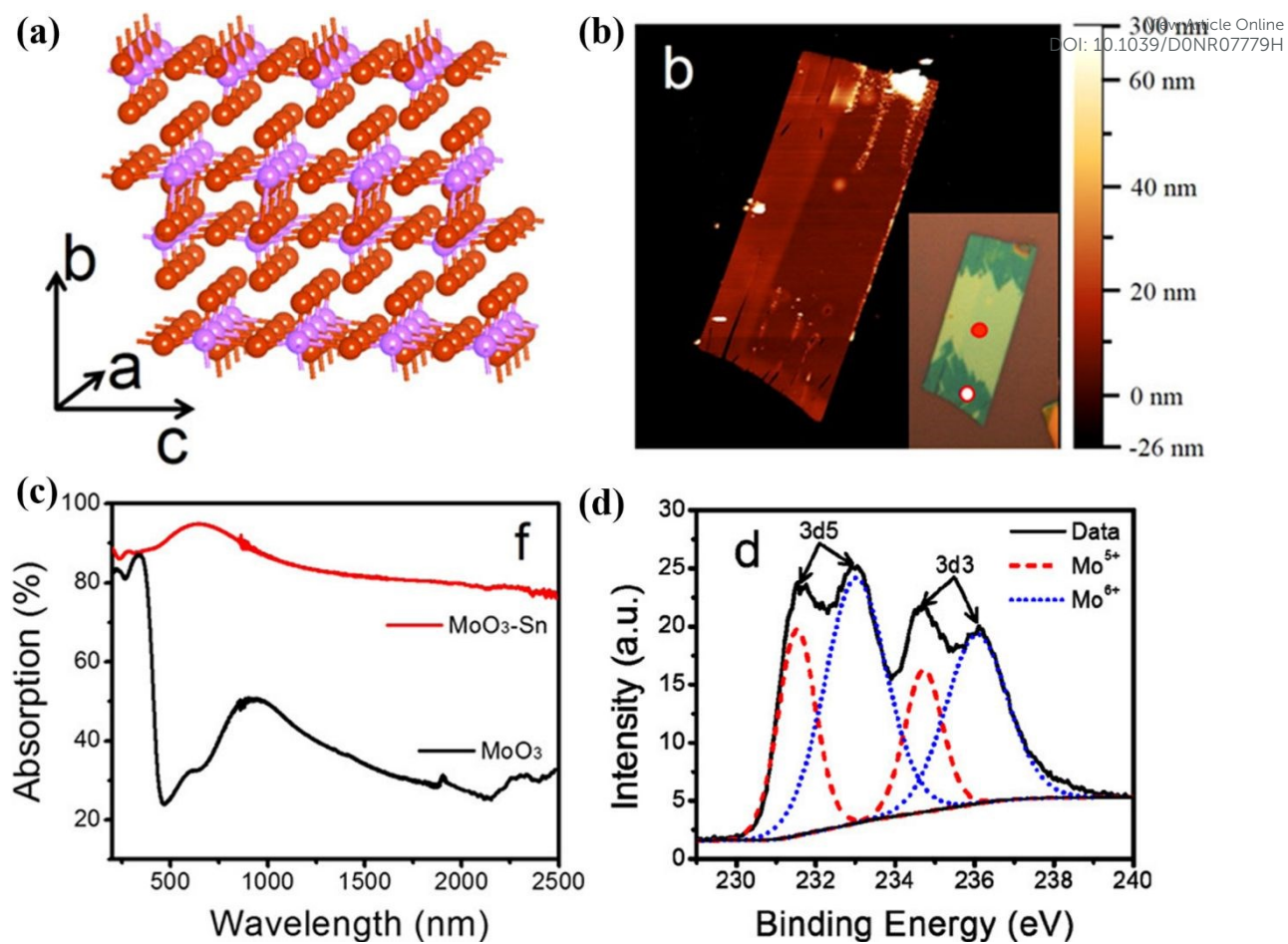


**Fig. 15.** (a) Atomic structure of the  $\alpha$ - $\text{MoO}_3$ . (b) The AFM image of the Sn-doped  $\alpha$ - $\text{MoO}_3$ . (c) The absorption spectra of for the  $\alpha$ - $\text{MoO}_3$  and Sn-doped  $\alpha$ - $\text{MoO}_3$ . (d) the Mo 3d XPS spectra obtained on Sn-doped  $\alpha$ - $\text{MoO}_3$ .<sup>[144]</sup> Reproduced with permission. Copyright 2019, The American Chemical Society.

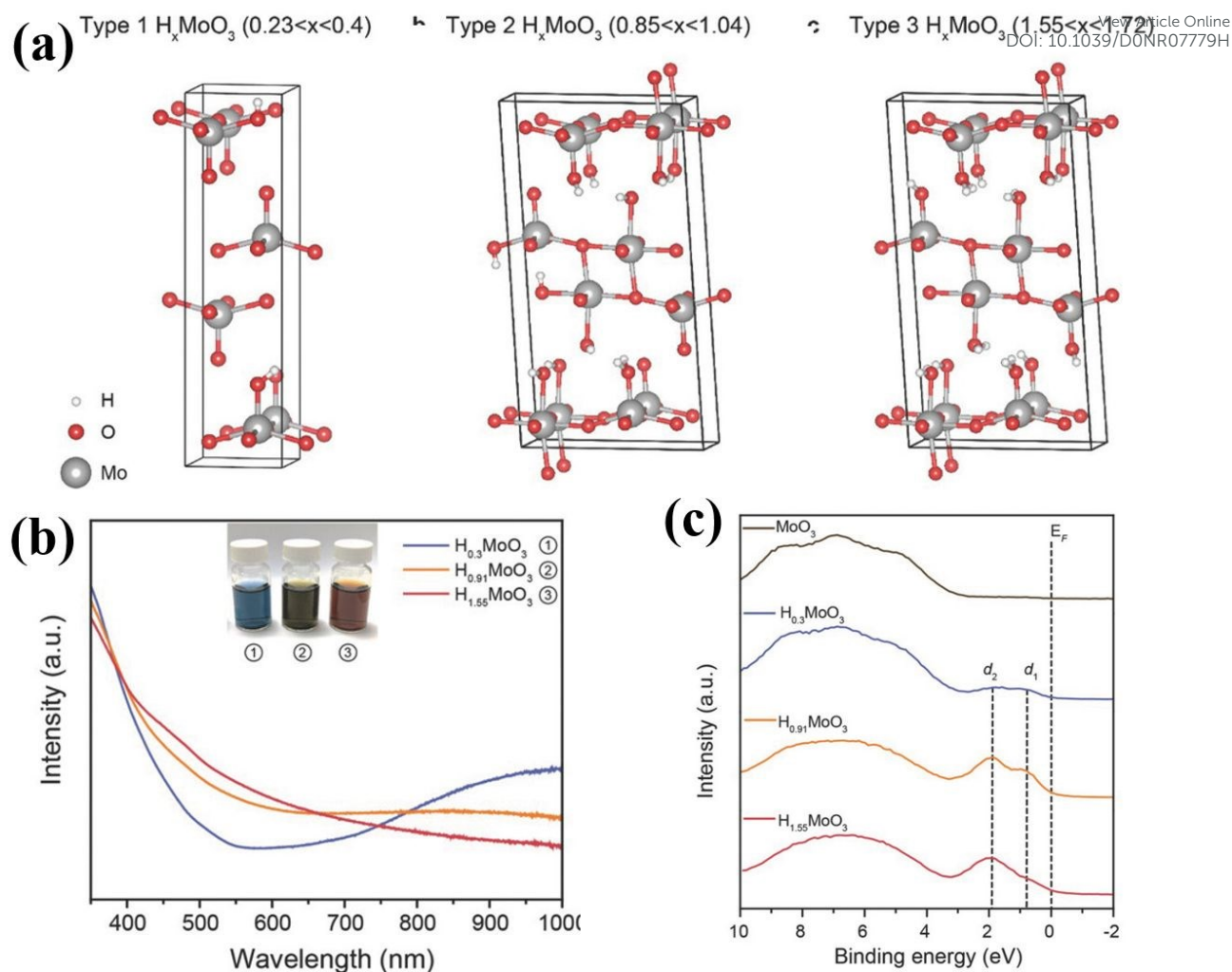


**Fig. 16.** (a) The atomic structure of the  $H_xMoO_3$  with different H concentrations. (b) The change of the absorption curve of the  $MoO_3$  aqueous solution under the light irradiation. (c) The evolution of the 2D  $MoO_{3-x}$  nano flake when exposed to the simulated solar light for different time.<sup>[140]</sup> Reproduced with permission. Copyright 2018, Wiley-VCH.

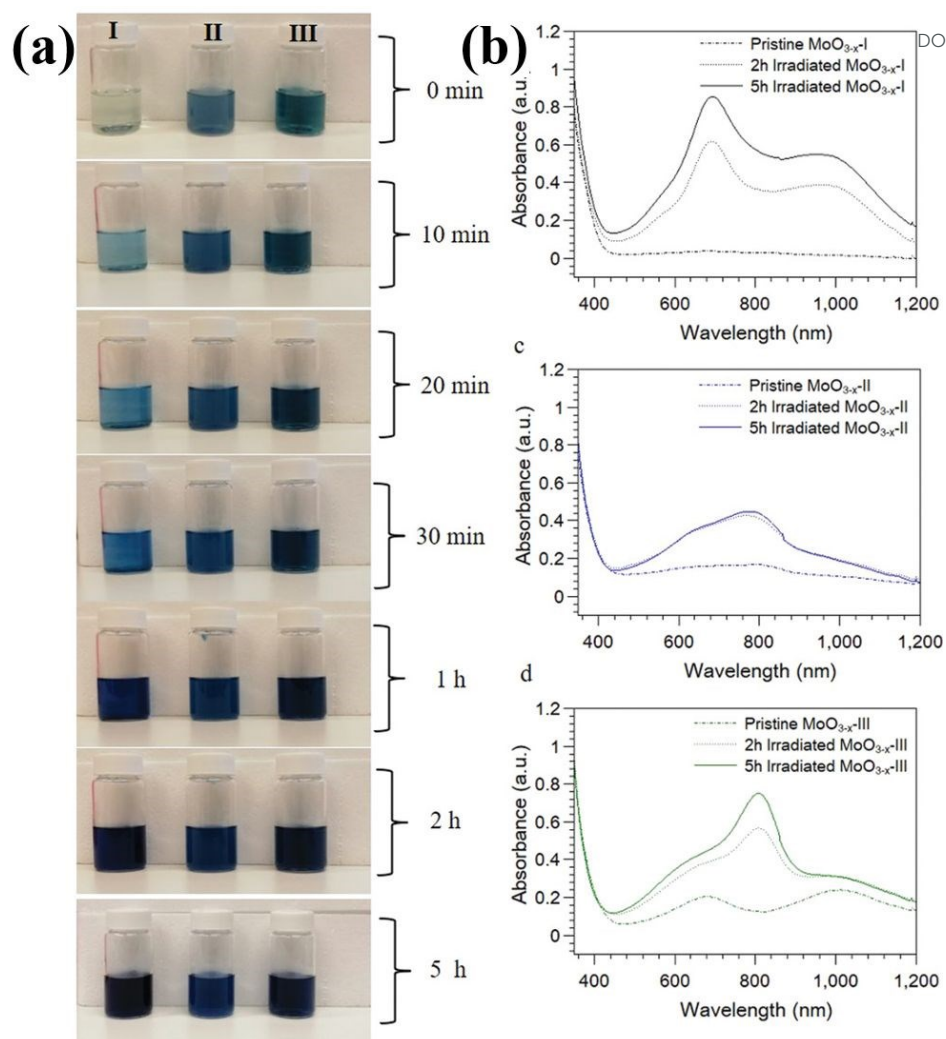


**Fig. 17.** (a) Photography of the temporal color change for the  $\text{MoO}_{3-x}\text{-I}$ ,  $\text{MoO}_{3-x}\text{-II}$  and  $\text{MoO}_{3-x}\text{-III}$  solution under the light illumination. (b) UV-vis-NIR spectra of the  $\text{MoO}_{3-x}\text{-I}$ ,  $\text{MoO}_{3-x}\text{-II}$  and  $\text{MoO}_{3-x}\text{-III}$  solution under the light illumination.<sup>[141]</sup>

Reproduced with permission. Copyright 2019, Wiley-VCH.

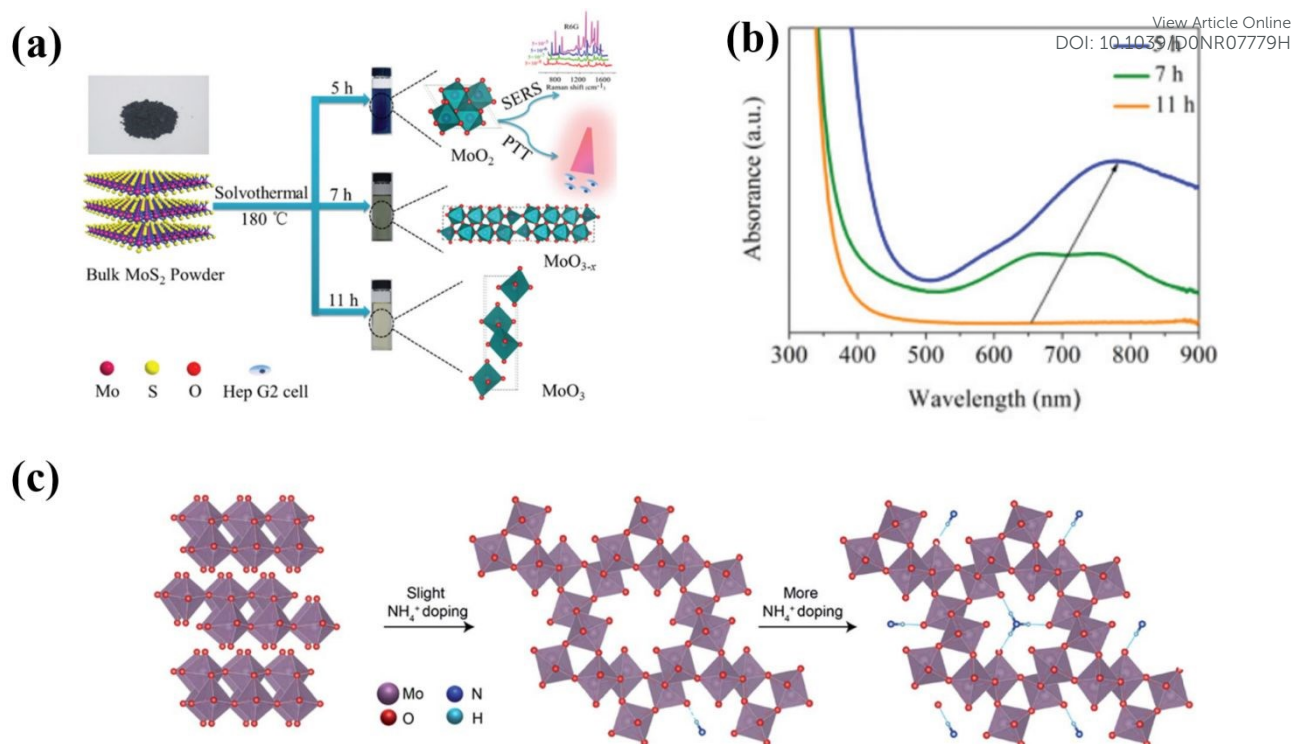


**Fig. 18.** (a) Schematic illustration of synthesizing method for the MoO<sub>x</sub> with different phases. (b) The UV-vis absorption spectra of the MoO<sub>x</sub> with different phases. (c) Schematics of the atomic structure evolution with the extending of the reaction time in the NH<sub>4</sub><sup>+</sup> solution.<sup>[162]</sup> Reproduced with permission. Copyright 2018, Royal Society of Chemistry.

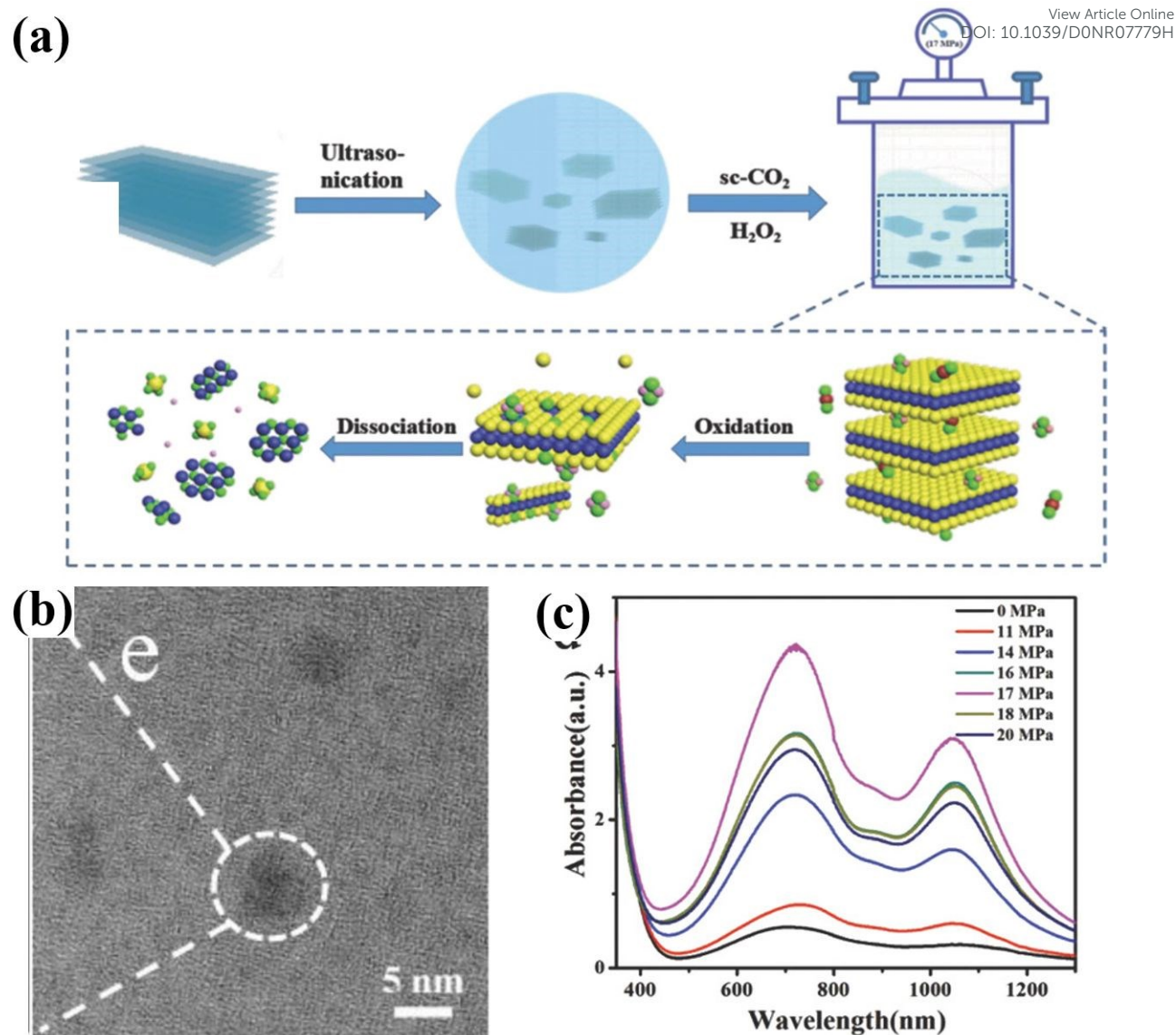


**Fig. 19.** (a) Schematic illustration of synthesizing process with the supercritical CO<sub>2</sub>. (b) The TEM image of the prepared H<sub>x</sub>MoO<sub>3</sub> quantum dot. (c) Schematics of the crystal structures evolution with the extending of the reaction time in the NH<sub>4</sub><sup>+</sup> solution.<sup>[164]</sup> Reproduced with permission. Copyright 2018, Wiley-VCH.

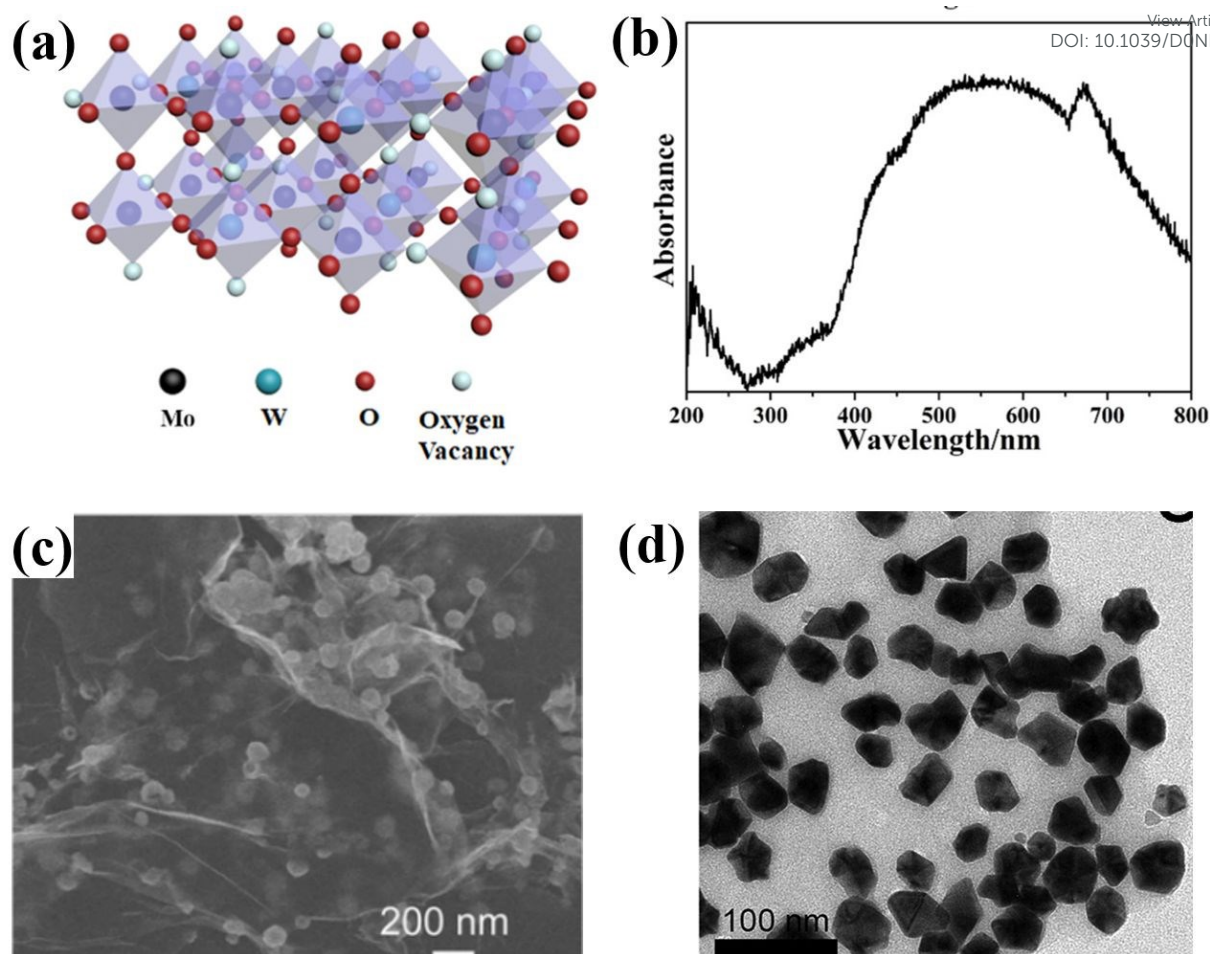


**Fig. 20.** (a) The atomic structure of the MWO hybrids. (b) The UV-vis absorption spectra of the MWO hybrids. Reproduced with permission.<sup>[165]</sup> Copyright 2020, The American Chemical Society. (c) The SEM image of the MoO<sub>2</sub>/GO hybrids.<sup>[168]</sup> Reproduced with permission. Copyright 2019, The Springer Nature Publishing Group. (d) The SEM image of the synthesized Au with HAuCl<sub>4</sub> as the precursor.<sup>[170]</sup> Reproduced with permission. Copyright 2019, Elsevier.

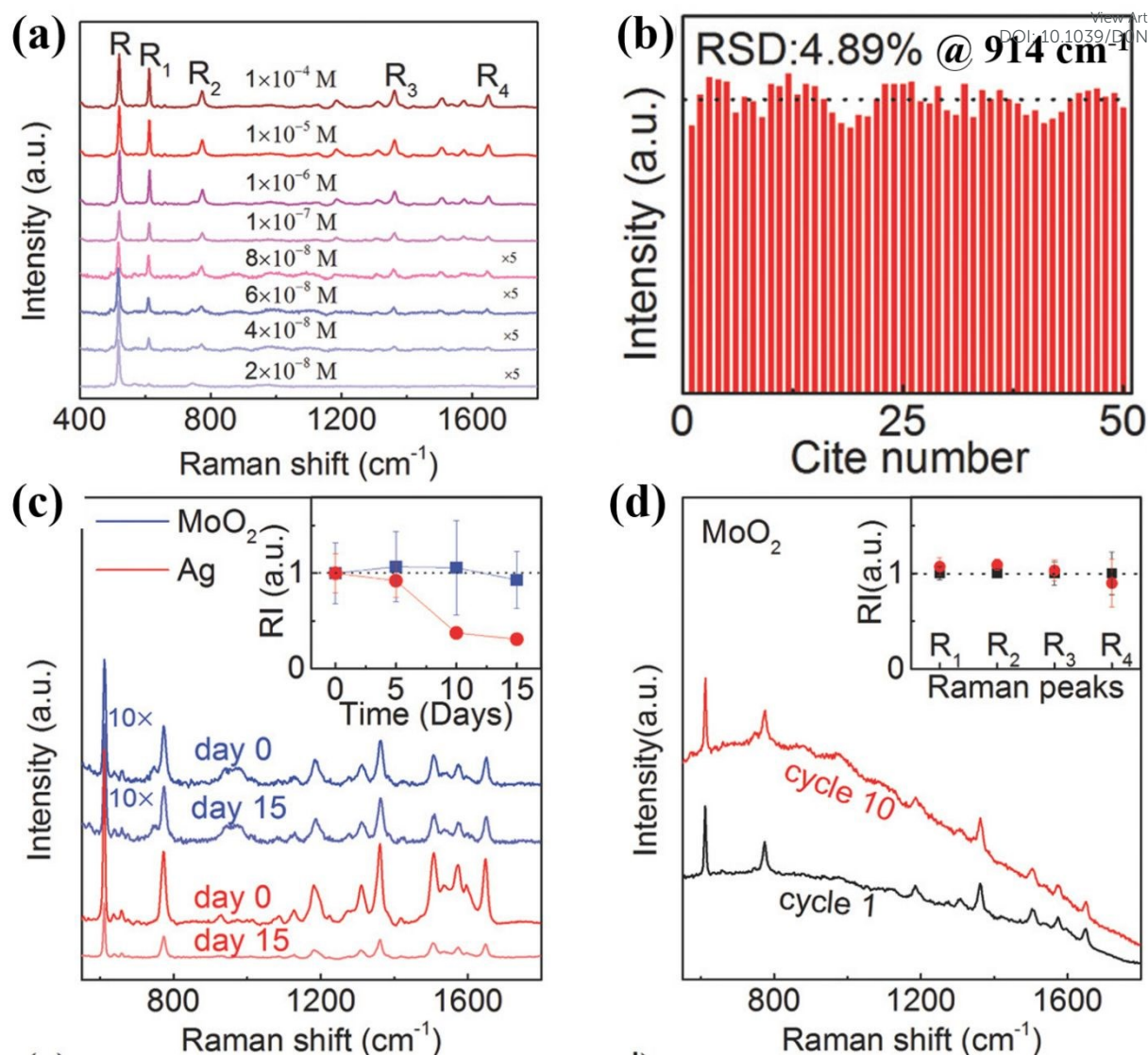


**Fig. 21.** (a) The Raman spectra measured on the prepared MoO<sub>2</sub> thin film. (b) The statistical distribution of SERS signal intensity (914 cm<sup>-1</sup>) that measured on MoO<sub>2</sub> thin film. (c) Excellent stability of the thin film compared to that of Ag. (d) The reusability of the MoO<sub>2</sub> thin film.<sup>[89]</sup> Reproduced with permission. Copyright 2018, Wiley-VCH.



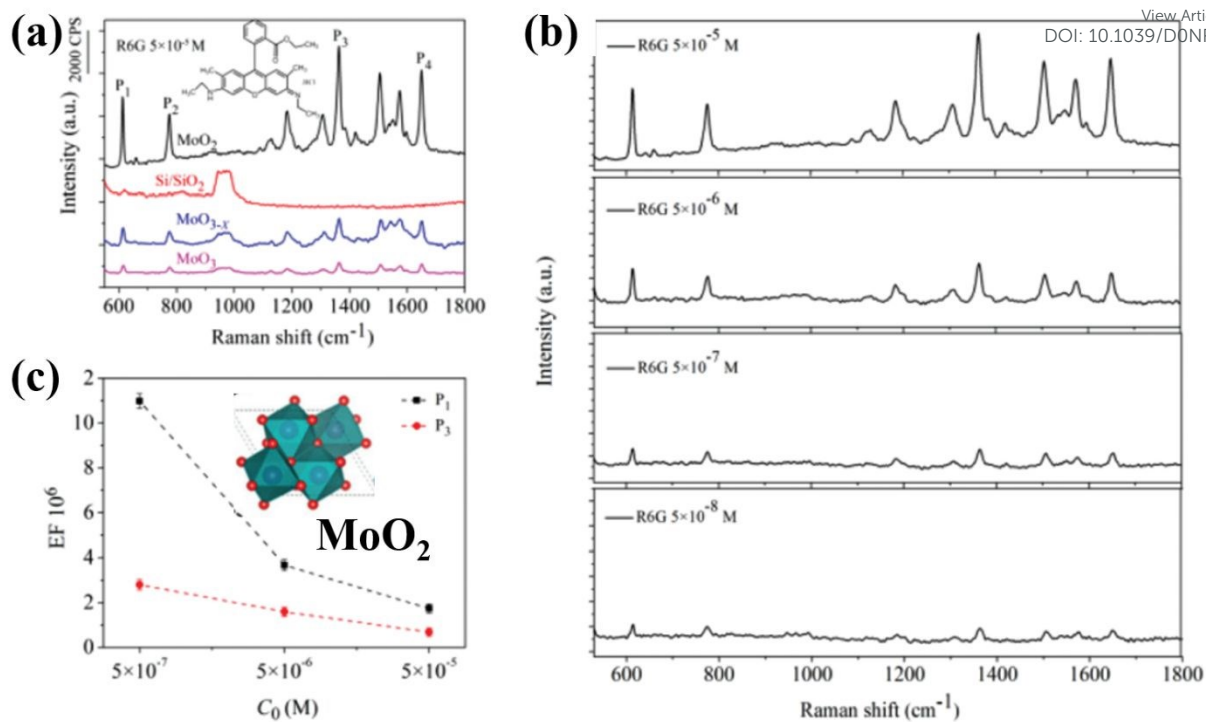


**Fig. 22.** (a) Raman Spectra of R6G solution ( $5 \times 10^{-5}$  M) mixed with  $\text{MoO}_2$ ,  $\text{MoO}_{3-x}$  and  $\text{MoO}_3$  NPS and bare silicon slice. (b) Raman spectra of R6G with different concentrations solution mixed with  $\text{MoO}_2$  NPS. (c) The EFs calculated under different R6G concentrations.<sup>[162]</sup> Reproduced with permission. Copyright 2018, Royal Society of Chemistry.

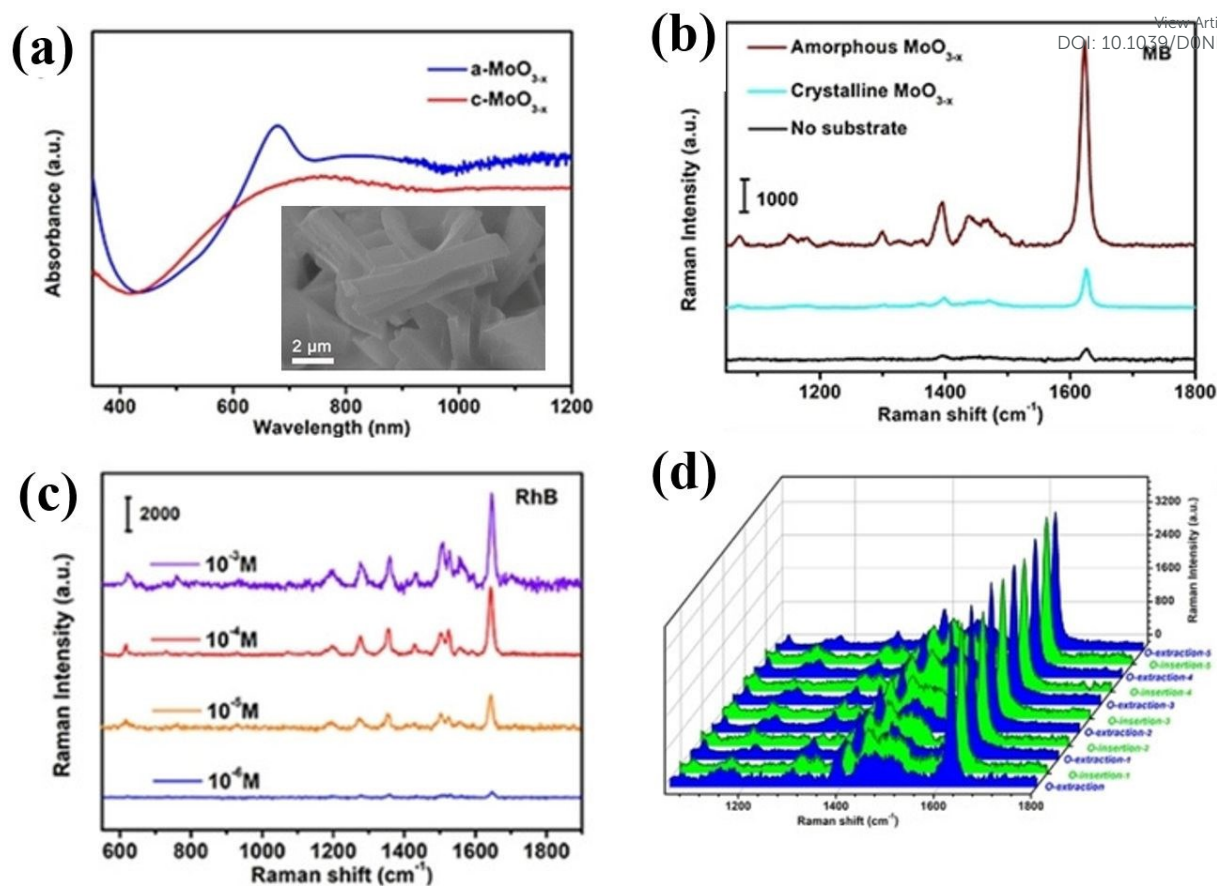


**Fig. 23.** (a) The UV-vis absorption spectra of the a-MoO<sub>3-x</sub> and c-MoO<sub>3-x</sub>. (b) The comparison of SERS spectra collected on the a-MoO<sub>3-x</sub> and c-MoO<sub>3-x</sub>. (c) SERS spectra of RhB collected on a-MoO<sub>3-x</sub> substrate. (d) The SERS activity of the a-MoO<sub>3-x</sub> after five cycles of oxygen insertion and extraction experiment.<sup>[174]</sup> Reproduced with permission. Copyright 2020, European Chemical Societies Publishing

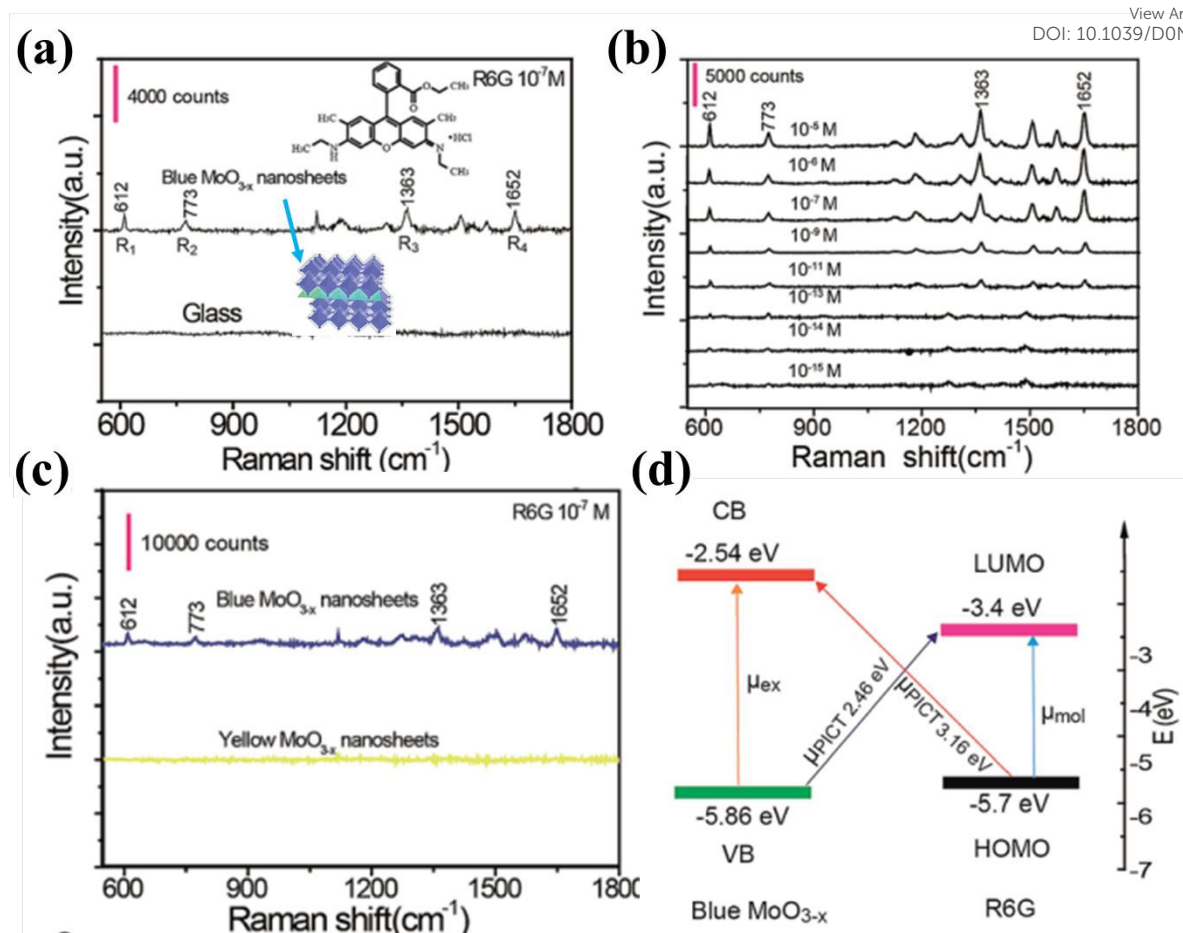


**Fig. 24.** (a) The SERS spectrum collected on the blue  $\text{MoO}_{3-x}$  nanosheets when R6G was used as the Raman reporter. (b) The SERS spectra of R6G with different concentrations collected on the blue  $\text{MoO}_{3-x}$  nanosheets. (c) Comparison of the SERS performance between the blue and yellow  $\text{MoO}_{3-x}$  nanosheets. (d) The illustration of the photo induced charge transfer path based on the defect energy level.<sup>[133]</sup> Reproduced with permission. Copyright 2019, Royal Society of Chemistry.

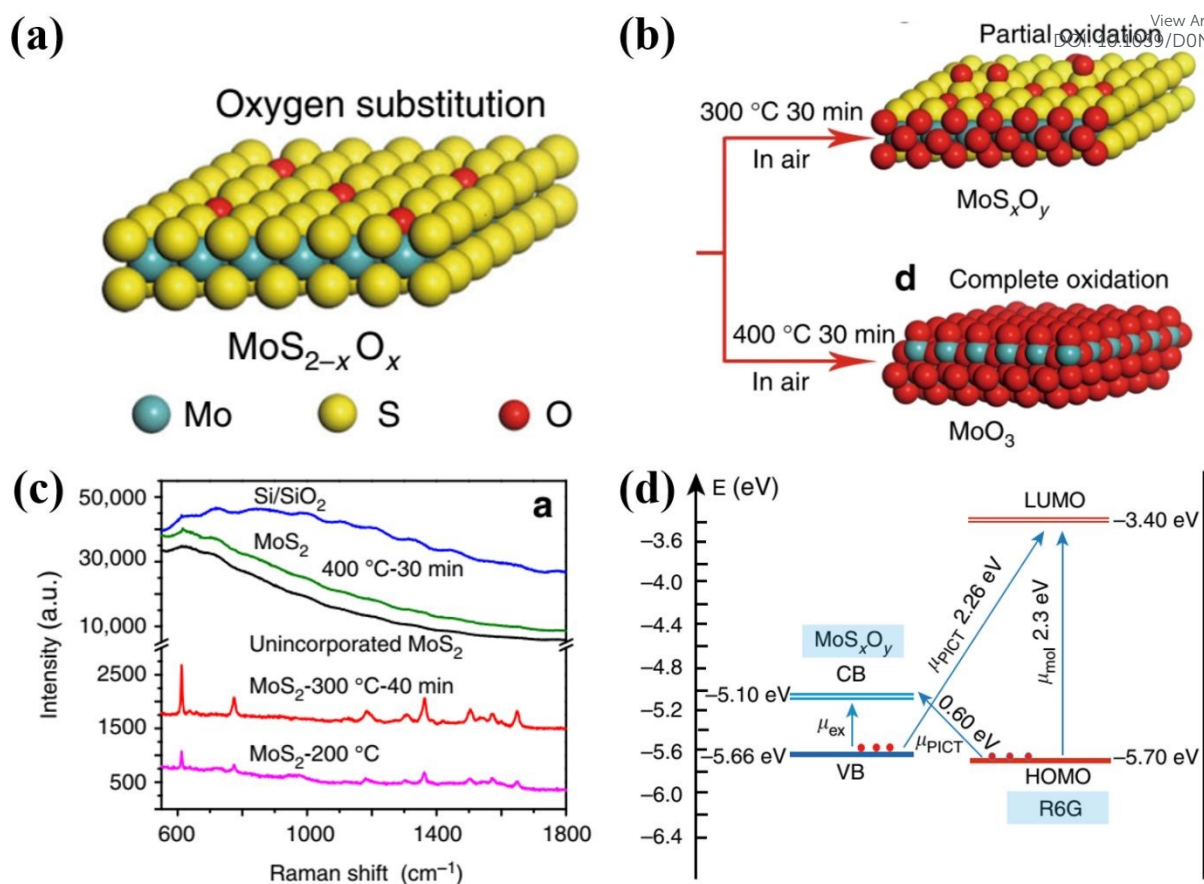


**Fig. 25.** (a) Atomic illustration of the preparing  $\text{MoS}_{2-x}\text{O}_x$  through the hydrothermal method. (b) Annealing of  $\text{MoS}_{2-x}\text{O}_x$  sample in the air through different conditions. (c) The SERS spectra measured on respective substrates when R6G is used as the Raman reporter. (d) The charge transfer path for the Raman signal enhancement during the measurement.<sup>[166]</sup> Reproduced with permission. Copyright 2017, Springer Nature Publishing Group.

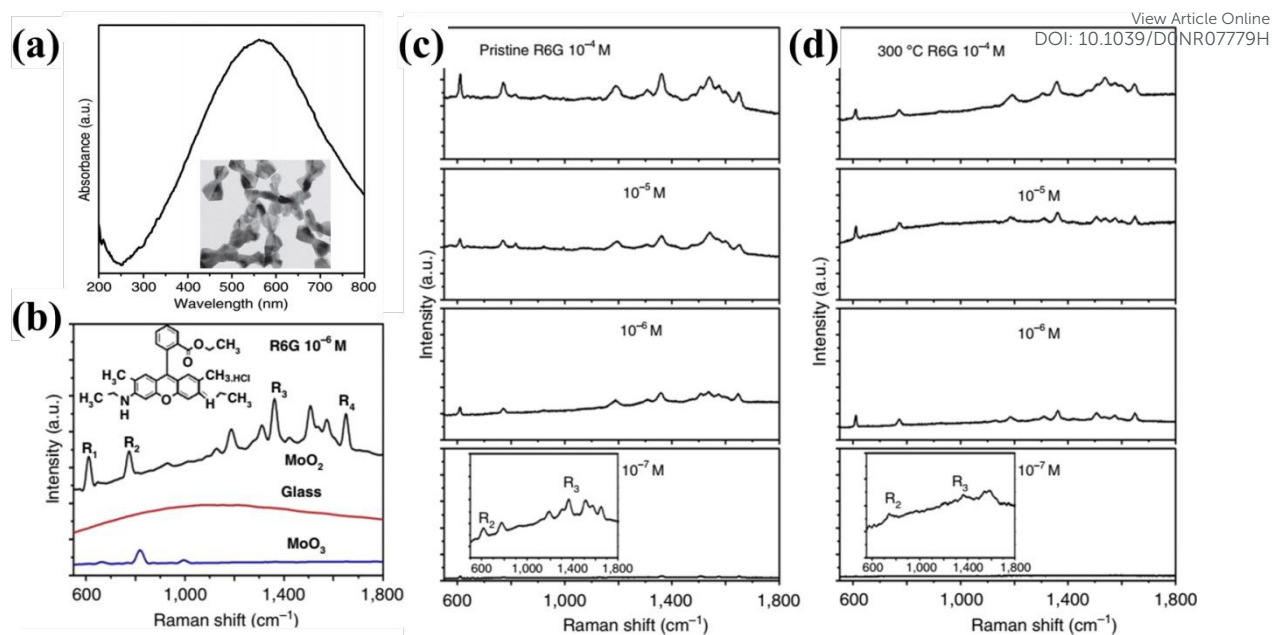


**Fig. 26.** (a) The TEM image of the hydrothermal prepared MoO<sub>2</sub> nano dumbbells. (b) The SERS spectra measured on the MoO<sub>2</sub> nano when R6G was used as the Raman reporter. (c) The SERS spectra recorded from R6G aqueous solution from 10<sup>-4</sup> to 10<sup>-7</sup> M. (d) The SERS spectra collected on the MoO<sub>2</sub> nano dumbbells after 300 °C annealing in the air. The inset in (a) shows the SEM images of the MoO<sub>x</sub> nano-dumbbell.<sup>[175]</sup> Reproduced with permission. Copyright 2017, Springer Nature Publishing Group.

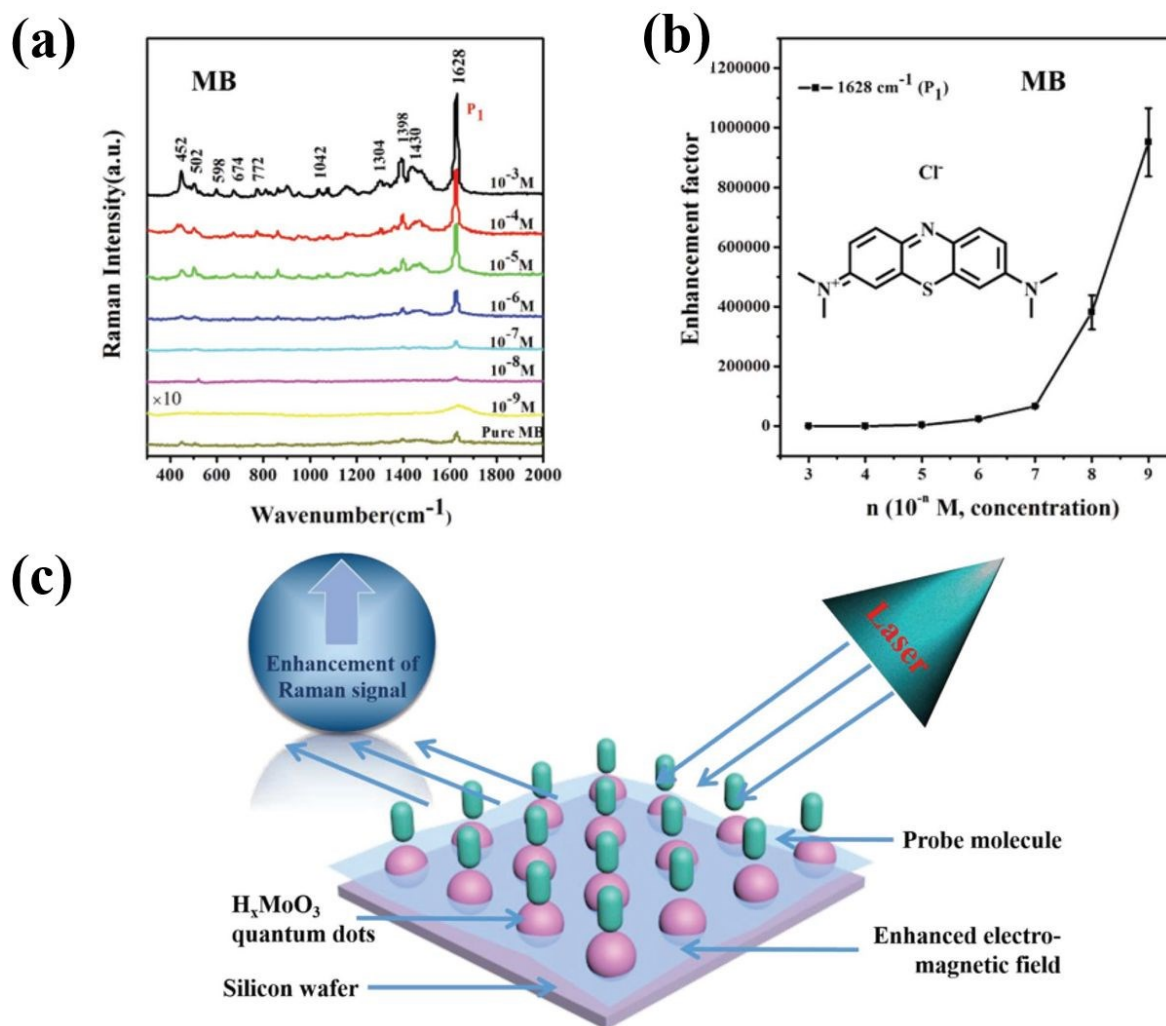


**Fig. 27.** (a) Raman spectra measured on the  $H_xMoO_3$  quantum dots as substrate, the  $H_xMoO_3$  quantum were prepared under 15%  $H_2O_2$  and 17 MPa  $SCO_2$ . (b) The Efs evolutions under different MB concentrations. (c) Schematic illustration of SERS enhancement mechanism by using the  $H_xMoO_3$  quantum dots as substrate.<sup>[164]</sup> Reproduced with permission. Copyright 2018, Wiley-VCH.

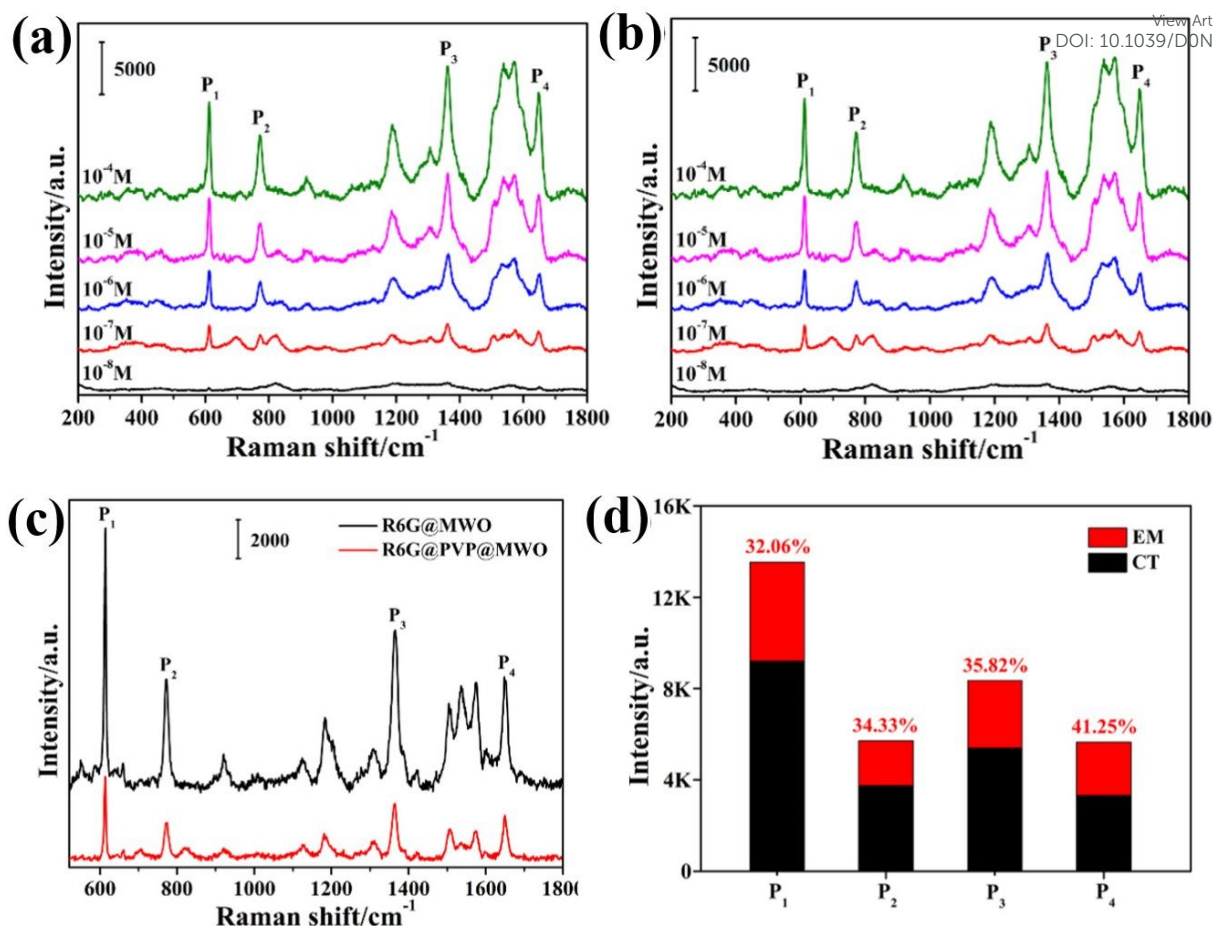


**Fig. 28.** (a) the SERS spectra of R6G measured on MWO hybrids, commercial WO<sub>3</sub> and commercial MoO<sub>3</sub>. (b) The detection limit of the MWO hybrids. (c) SERS spectra of R6G measured on pure MWO hybrids and PVP-coated MWO hybrids. (d) The calculated contributions of EM and CT to SERS.<sup>[165]</sup> Reproduced with permission. Copyright 2020, The American Chemical Society.

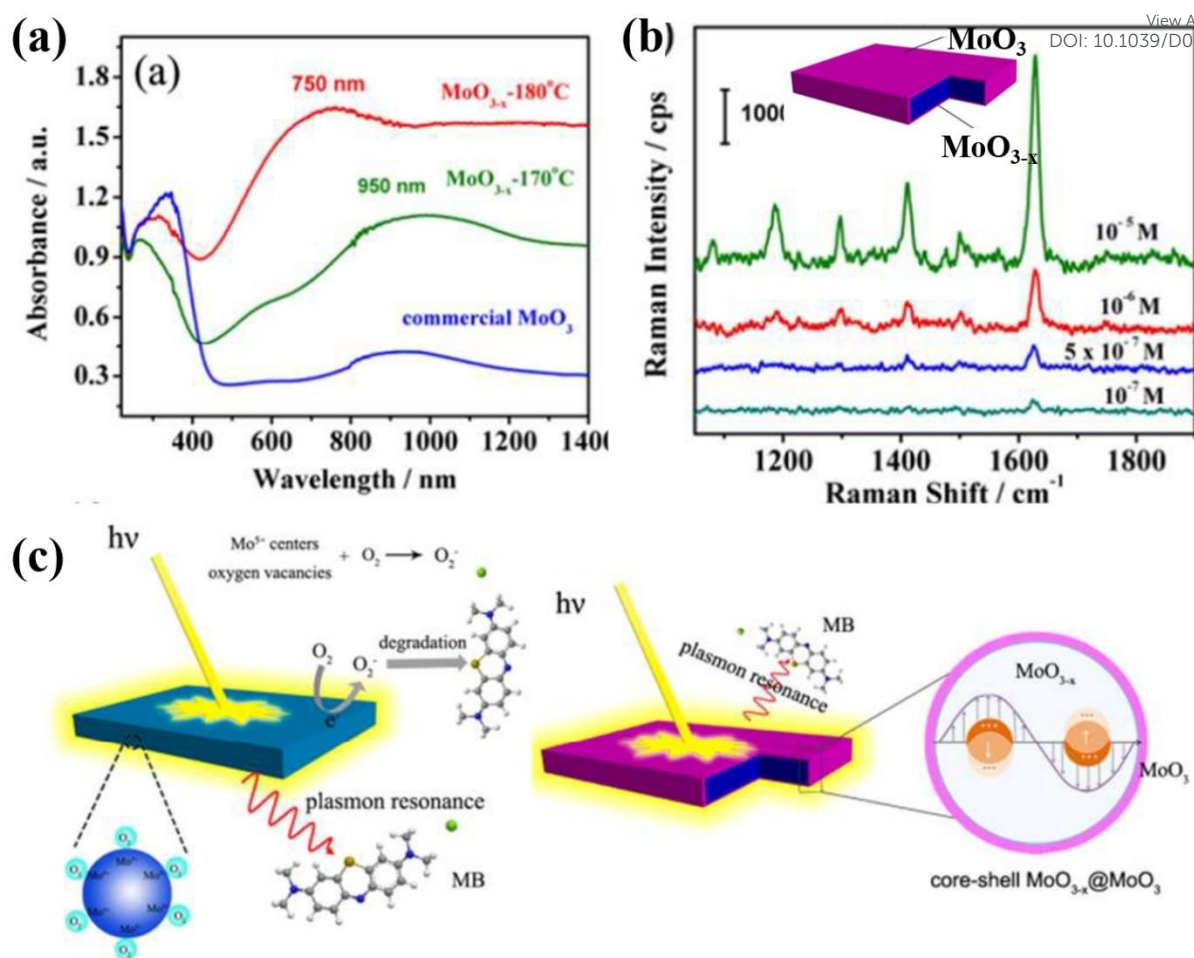


**Fig. 29.** (a) UV-vis spectra of the  $\text{MoO}_{3-x}$  nanosheets prepared under different annealing conditions. (b) The SERS spectra measured on  $\text{MoO}_{3-x}$  nanosheets after annealing at 200 °C for 6 hours. (c) The understanding of the SERS improvement mechanism for the  $\text{MoO}_{3-x}$  nanosheets after the annealing process.<sup>[176]</sup> Reproduced with permission. Copyright 2016, Royal Society of Chemistry.



## ARTICLE

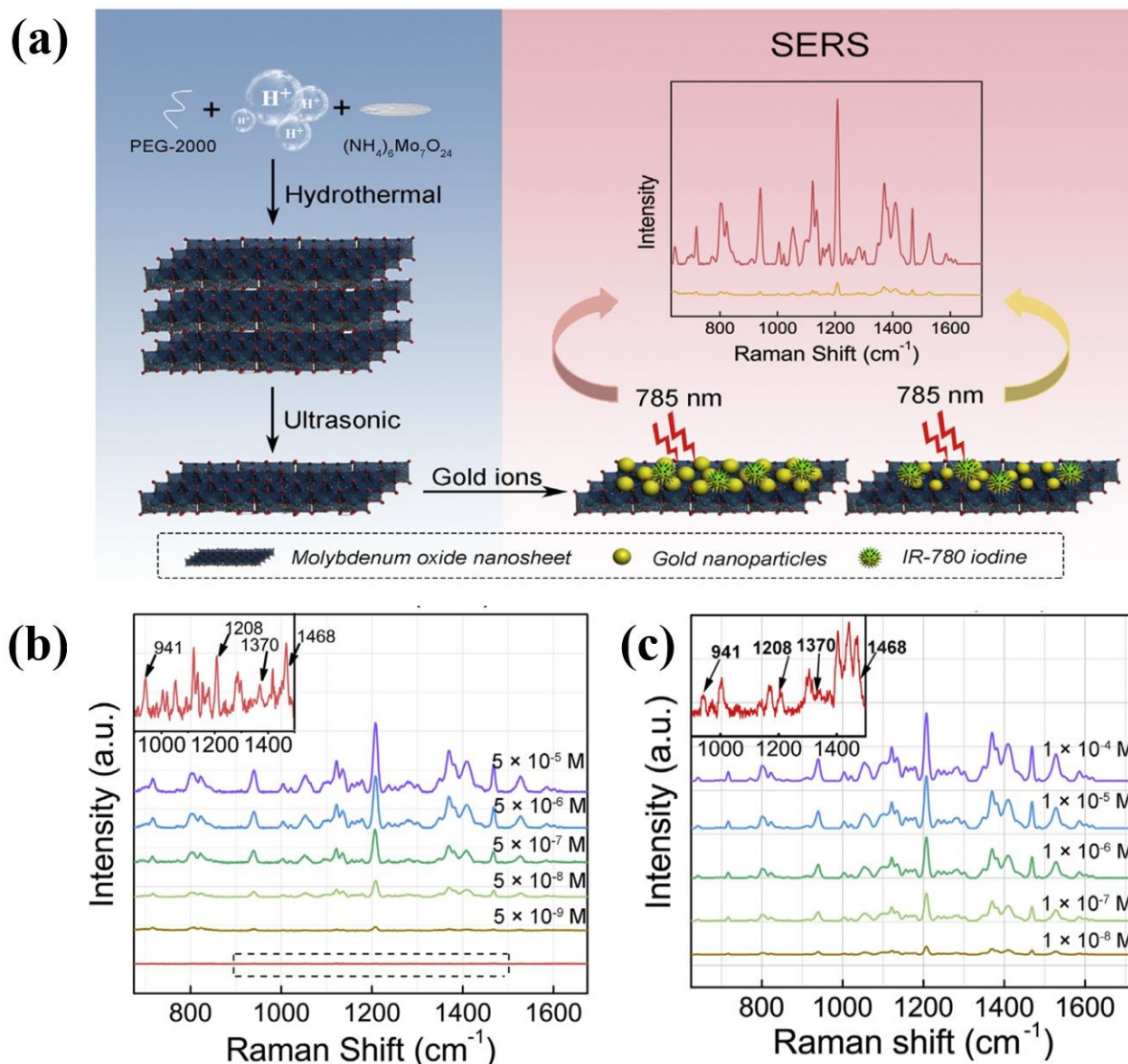


**Fig. 30.** (a) Schematic illustration of the steps for fabricating the MoO<sub>x</sub>-AuNSs complex. (b) The SERS spectra of IR-70 obtained in the aqueous solution with MoO<sub>x</sub>-AuNSs. (c) The SERS spectra of IR-70 obtained in albumin solution with MoO<sub>x</sub>-AuNSs.<sup>[170]</sup> Reproduced with permission. Copyright 2019, Elsevier.